



Max Planck Graduate Center

Johannes Gutenberg-Universität, Mainz



Parahydrogen Induced Polarization
on a Clinical MRI System:
Polarization Transfer of Two Spin Order

Dissertation zur Erlangung des Grades eines
„Doktor rerum naturalium“ der Fachbereiche:
08 - Physik, Mathematik und Informatik,
09 - Chemie, Pharmazie und Geowissenschaften,
10 - Biologie sowie
Universitätsmedizin

von Dirk Markus Graafen

Mainz, 2013

1. Gutachter:

2. Gutachter:

Tag der Promotion: 12.02.2013

Zusammenfassung

Hyperpolarisationsmethoden verstärken die Kernspinpolarisation und ermöglichen dadurch neue Anwendungen der Kernspinresonanz wie die Bildgebung von Stoffwechselprozessen. Eine dieser Methoden ist die Parawasserstoff Induzierte Polarisation (PHIP), welche einen hyperpolarisierten ^1H -Zustand erzeugt. Diese Hyperpolarisation kann durch Sequenzen von Radiofrequenzpulsen auf einen Heterokern wie ^{13}C übertragen werden. In dieser Arbeit wurde die Zeitabstimmung einer solchen Sequenz für das Molekül Hydroxyethylpropionat analysiert und optimiert. Die Pulssequenz wurde für einen klinischen Kernspintomographen angepasst, so dass sie mit einem einzigen Sendekanal verwendet werden kann. Optimierungssimulationen basierend auf der Theorie der optimalen Steuerung wurden durchgeführt, um den Polarisationstransfer zu verbessern.

Ein Nachteil der Hyperpolarisation ist, dass sie aufgrund von Relaxationsprozessen nur eine eingeschränkte Lebensdauer hat. Diese kann erhöht werden, indem die Hyperpolarisation in einem Singulett-Zustand gespeichert wird. Der zweite Teil dieser Arbeit befasst sich daher mit dem Singulett-Zustand des Cs-symmetrischen Moleküls Dimethylmaleat, welcher für Messungen in einen Triplett-Zustand überführt werden muss. Diese Konversion wurde in einem klinischen Kernspintomographen zum einen durch eine Magnetfeldvariation zum anderen durch zwei Pulssequenzen realisiert. Mehrfach aufeinanderfolgende Konversion wurden verwendet, um die Lebensdauer des Singulett-Zustands und die Konversionseffizienz der Pulssequenz zu bestimmen.

Beide Möglichkeiten, der hyperpolarisierte ^{13}C -Zustand und der konvertierte Singulett-Zustand, wurden zur Bildgebung verwendet. Die Notwendigkeit einer sorgfältigen Wahl der Echozeit wurde für beide Moleküle gezeigt.

Abstract

Hyperpolarization techniques enhance the nuclear spin polarization and thus allow for new nuclear magnetic resonance applications like *in vivo* metabolic imaging. One of these techniques is Parahydrogen Induced Polarization (PHIP). It leads to a hyperpolarized ^1H spin state which can be transferred to a heteronucleus like ^{13}C by a radiofrequency (RF) pulse sequence. In this work, timing of such a sequence was analyzed and optimized for the molecule hydroxyethyl propionate. The pulse sequence was adapted for the work on a clinical magnetic resonance imaging (MRI) system which is usually equipped only with a single RF transmit channel. Optimal control theory optimizations were performed to achieve an optimized polarization transfer.

A drawback of hyperpolarization is its limited lifetime due to relaxation processes. The lifetime can be increased by storing the hyperpolarization in a spin singlet state. The second part of this work therefore addresses the spin singlet state of the Cs-symmetric molecule dimethyl maleate which needs to be converted to the spin triplet state to be detectable. This conversion was realized on a clinical MRI system, both by field cycling and by two RF pulse sequences which were adapted and optimized for this purpose. Using multiple conversions enables the determination of the lifetime of the singlet state as well as the conversion efficiency of the RF pulse sequence.

Both, the hyperpolarized ^{13}C spin state and the converted singlet state were utilized for MR imaging. Careful choice of the echo time was shown to be crucial for both molecules.

Contents

1	Introduction	1
2	General Theory	5
2.1	Nuclear Magnetic Resonance	5
2.2	Polarization Transfer	7
2.3	Parahydrogen Induced Polarization	9
2.4	Relaxation	12
2.5	Spin Dynamics Simulations	14
2.6	Imaging	14
3	Heteronuclear Polarization Transfer	19
3.1	Theory / Previous Work	20
3.2	PH-INEPT+ Sequence	21
3.2.1	Sequence Timing Optimization	22
3.2.2	Implementation on a Clinical MRI System	30
3.2.3	Combination with MR Imaging	35
3.3	Optimal Control	40
3.3.1	Theory	40
3.3.2	Optimization of Polarization Transfer using OC Theory	42
3.3.3	Off-resonance Stabilization	47
3.4	Discussion	50
3.4.1	Hollow-Fiber Membrane Modules	50
3.4.2	Hyperpolarized ^{13}C Spin State	50
3.4.3	Polarization Transfer Sequence	51
3.4.4	Optimal Control	53
3.4.5	Imaging	53
3.4.6	^{13}C Labeling / Deuteration	54
4	Long-Lived Nuclear Spin States	55
4.1	Theory / Previous Work	56
4.2	Singlet Triplet Conversion	59

4.2.1	Field Cycling	59
4.2.2	RF Pulse Sequences	62
4.3	Multiple Conversion Experiment	68
4.3.1	Continuous Wave	71
4.3.2	Chemical Shift Scaling Sequence	74
4.4	Imaging	76
4.5	Discussion	79
4.5.1	Reference Measurement	79
4.5.2	Multiple Conversion Experiment	80
4.5.3	Singlet State Lifetime	80
4.5.4	RF Pulse Sequences	81
4.5.5	Imaging	83
4.5.6	Chemical Limitations	84
4.5.7	Comparison to Other Studies	84
5	Conclusion and Outlook	87
6	Bibliography	89
7	Appendix	97
7.1	Abbreviations	97
7.2	Chemical Composition of Samples	99
7.3	Product Operator Formalism	100
7.4	Optimal Control Input File	103
7.5	Acknowledgments	109
7.6	Declaration	111
7.7	Curriculum Vitae	113

Chapter 1

Introduction

The experimental proof of the proton spin by Gerlach and Stern [1922] paved the way for the rapid development of nuclear magnetic resonance (NMR) spectroscopy as a powerful tool in analytical chemistry. Due to the later invention of magnetic resonance imaging (MRI) by Lauterbur [1973] and Mansfield [1976], NMR found its way to the field of medicine. Nowadays, MRI in medicine is a versatile diagnostic tool. Beside anatomical imaging, important physiologic parameters can be observed including e. g. perfusion, blood flow and diffusion. Additionally, the composition of metabolites can be analyzed *in vivo* using magnetic resonance spectroscopy.

However, NMR is a rather insensitive method. Due to the low gyromagnetic ratio of nuclear spins, only a small fraction of all spins contribute to the observable NMR signal (e. g. around 10^{-6} proton spins at 1.5 T and room temperature). The applicability of NMR in medicine is therefore mainly based on the huge amount of abundant nuclear spins (water has a proton density $\approx 6.7 \times 10^{22} \text{ cm}^{-3}$). The observation of a small amount of molecules which would be beneficial for e. g. cancer diagnostic is limited especially in *in vivo* magnetic resonance spectroscopy (MRS).

Several techniques have been developed to achieve distinctive higher populations of certain spin states commonly called hyperpolarization. To generate a hyperpolarized liquid, the applicable methods are the dynamic nuclear polarization (DNP) [Abragam and Goldman, 1978] and parahydrogen induced polarization (PHIP) [Bowers and Weitekamp, 1986, Natterer and Bargon, 1997].

Ardenkjaer-Larsen et al. [2003] built a DNP polarizer which creates hyperpolarized solutions using solid-state DNP techniques. A sample consisting of the target molecule and an organic free radical is cooled down to 1 K at 3.35 T which leads to an electron polarization of $P(e^-) \approx 0.97$, whereas the Carbon-13 polarization is only $P(^{13}\text{C}) \approx 8 \times 10^{-4}$ under these conditions. This difference is based on the much higher gyromagnetic ratio of the electrons: $\gamma(e^-) \approx 2600\gamma(^{13}\text{C})$. The high polarization of the electrons can be in part transferred to the nuclear spins by microwave irradiation. Subsequent to the polar-

ization process, the sample is rapidly dissolved to maintain the high polarization of the ^{13}C solution. With this method a polarization of about 20% to 30% can be reached for $^{13}\text{C}_1$ -pyruvate. However, only a few milliliters can be polarized within a duration of one hour. DNP polarizers are commercially available (HyperSense, Oxford Instruments, UK). Recently, an alternative approach was published generating hyperpolarization using liquid state DNP directly in the bore of an MRI scanner [Krummenacker et al., 2012].

Parahydrogen (pH_2) is the antisymmetric singlet spin state isomer of the two spin system in the hydrogen molecule. Parahydrogen induced polarization (PHIP) is based on the spin order transfer of pH_2 to a target molecule. This could be performed both by a hydrogenation reaction or by reversible exchange (SABRE, signal amplification by reversible exchange). For the hydrogenation, two different methods are distinguished: PASADENA (parahydrogen and synthesis allow dramatically enhanced nuclear alignment) and ALTADENA (adiabatic longitudinal transport after dissociation engenders net alignment). In both methods, pH_2 is catalytically added to an unsaturated molecule preserving the relative spin orientation of pH_2 . Therefore, only certain spin states are populated in the target molecule leading to a non-equilibrium nuclear alignment of ^1H far above the Boltzmann polarization. To generate a hyperpolarized ^{13}C spin state using PHIP, the ^1H hyperpolarization needs to be transferred. This can be performed both by field cycling [Johannesson et al., 2004] or by radiofrequency (RF) pulse sequences. The pulse sequences can be divided into the sequences working at low magnetic field [Goldman and Johannesson, 2005, Kadlecik et al., 2010] and the high field sequences [Haake et al., 1996]. These sequences require a combination of pulses at both ^1H and ^{13}C frequencies, conventionally transmitted simultaneously. Hövener et al. [2009] built an external polarizer which performs the hydrogenation in a reaction chamber and generates the polarization transfer using the low field sequence by Goldman and Johannesson [2005]. This requires a complete low field NMR unit consisting of a B_0 field coil, RF transmission coils and RF amplifiers. With this polarizer, ^{13}C hyperpolarization of 20% could be generated. In contrast to the commercial DNP polarizer, a hyperpolarized solution of 5 ml is capable in less than one minute.

A major drawback of the liquid state hyperpolarization methods is the limited lifetime of the hyperpolarized spin state due to longitudinal relaxation processes. This is a disadvantage particularly for *in vivo* applications in which a certain delay between the hyperpolarization generation and the acquisition is needed. This is to allow for injection and subsequent distribution of the hyperpolarized molecules in the organism. Due to this restriction, *in vivo* applications are typically performed with ^{13}C hyperpolarized molecules which show longer hyperpolarization lifetimes due to the longer longitudinal relaxation times in comparison to ^1H . The use of ^{13}C hyperpolarization benefits additionally from the lack of a background signal due to the low natural abundance (only 1%) and the four times less gyromagnetic ratio in comparison to ^1H . Moreover for *in vivo* MRS, the wide chemical

shift range (10-fold of protons) delivers a better split between resonance peaks.

The promising application of DNP hyperpolarized molecules for *in vivo* investigations on animal models was shown in several studies [Yen et al., 2011], most of them used $^{13}\text{C}_1$ -pyruvate. The first *in vivo* works utilized the DNP hyperpolarized molecules for angiography [Golman et al., 2002, Svensson et al., 2003] and cerebral perfusion measurements [Johansson et al., 2004a], i. e. the supply of the brain with blood. Golman et al. [2006] showed the possibility of measuring metabolic images of ^{13}C -pyruvate and its metabolic products, ^{13}C -lactate and ^{13}C -alanine. This opened up for cancer diagnostic since an elevated lactate concentration is expected in tumor tissue [Warburg, 1956]. Using metabolic imaging with hyperpolarized ^{13}C -pyruvate, an elevated lactate concentration in prostate cancer [Chen et al., 2007, Albers et al., 2008], glioma [Park et al., 2010] and hepatocellular carcinoma [Darpolor et al., 2011] was found. Moreover, the response to chemotherapy was shown in some studies [Day et al., 2007, Park et al., 2011]. Beside cancer diagnostic, metabolic imaging with hyperpolarized ^{13}C -pyruvate was used to investigate cardiac metabolism under diabetes [Schröder et al., 2008] and in infarcted myocardium [Golman et al., 2008]. Even though, the most studies are performed with ^{13}C -pyruvate, also other DNP hyperpolarized molecules exist which are interesting for *in vivo* applications. Gallagher et al. [2008] used hyperpolarized ^{13}C -bicarbonate for *in vivo* MR imaging of pH. It was shown that hyperpolarized ^{13}C -fumarate provides a sensitive marker for cellular necrosis [Gallagher et al., 2009].

In comparison to DNP, only a few studies exist showing the *in vivo* applicability of PHIP hyperpolarized molecules. Using the field cycling method, hyperpolarized hydroxyethyl- ^{13}C -propionate (^{13}C -HEP) was used for angiography [Golman et al., 2001] and perfusion measurements [Johansson et al., 2004b]. Bhattacharya et al. [2005] first performed angiography with hyperpolarized hydroxyethyl- ^{13}C -propionate (HEP) generated by an external polarizer realizing the polarization transfer with the low field RF sequence of Goldman and Johannesson [2005]. The possibility to use PHIP hyperpolarized ^{13}C -succinate for cancer diagnostic was predicted by Bhattacharya et al. [2007] who showed the enhancement of metabolic products of succinate in a brain tumor by *ex vivo* ^{13}C NMR spectroscopy. PHIP hyperpolarized tetrafluoropropyl- ^{13}C -propionate (TFPP) can be used for atheroma diagnostics since it shows a stronger binding to the lipid bilayer on the intimal surface in atheroma regions [Bhattacharya et al., 2011]. The main reason for the fewer *in vivo* applications of PHIP hyperpolarized molecules might be the lack of a commercial available polarizer. Even though there is a higher restriction on the molecules to be polarized by the PHIP method, the higher production rate of hyperpolarization might be an advantage for future *in vivo* applications especially in humans.

Even though the lifetime of the hyperpolarized ^{13}C spin state is longer than for ^1H , it is still limited to around one minute. A newer approach to increase the lifetime is to store

the hyperpolarization in a nuclear spin singlet state being built by two nuclear spins. The singlet spin state has a prolonged lifetime since for symmetry reasons the singlet spin state cannot relax by the intramolecular dipole-dipole interaction which is often the strongest relaxation mechanism. However, the singlet spin state itself is not observable and therefore needs to be converted into the measurable triplet spin state. The increase of the lifetime using the storage in the singlet state has been shown for DNP hyperpolarized double ^{13}C labeled molecules by a few studies [Laustsen et al., 2012, Feng et al., 2012, Pileio et al., 2012]. For this purpose, the singlet state needs to be created by an RF pulse sequence and retransferred into detectable magnetization after a delay. Recently, Franzoni et al. [2012] showed that the storage of the PHIP hyperpolarization in the ^1H singlet spin state of a Cs-symmetric molecule is very effective for increasing the lifetime of the hyperpolarization in the order of several minutes. Using the PHIP hyperpolarization method has the advantage that the singlet state is directly created without the necessity of an RF pulse sequence. Buljubasich et al. [2012] showed the transfer into detectable magnetization for the Cs-symmetric molecule dimethyl maleate can be achieved by moving the sample to a low resonance magnetic field. However, for *in vivo* applications it is impractical to move the object (an animal or a patient) to the resonance field during the measurement.

The aim of the present work is to realize both the $^1\text{H}/^{13}\text{C}$ polarization transfer and the singlet triplet conversion in the magnetic field of a clinical MRI system. The challenge of $^1\text{H}/^{13}\text{C}$ polarization transfer is that a conventional clinical NMR scanner is equipped with a single RF transmit channel which does not allow the simultaneous transmission on both frequencies. Chapter 3 treats this problem including the optimization of the sequence timing, the implementation on a clinical MRI system and the combination of the polarization transfer with an imaging sequence. Additionally, optimizations of the polarization transfer are performed using the optimal control theory. Chapter 4 deals with the singlet triplet conversion. RF pulse sequences are adapted to perform the singlet triplet conversion in the Cs-symmetric molecule inside the magnet, i. e. avoiding the movement of the sample. These sequences are analyzed and combined with an imaging sequence. Finally, the conclusions and the outlook are presented in chapter 5.

Chapter 2

General Theory

Contents

2.1 Nuclear Magnetic Resonance	5
2.2 Polarization Transfer	7
2.3 Parahydrogen Induced Polarization	9
2.4 Relaxation	12
2.5 Spin Dynamics Simulations	14
2.6 Imaging	14

2.1 Nuclear Magnetic Resonance

Nuclear magnetic resonance (NMR) is based on the nuclear spins. The magnetic moment μ of a nucleus is proportional to its spin angular momentum I :

$$\mu = \gamma I, \tag{2.1}$$

where the factor of proportionality γ is called the gyromagnetic ratio¹. It is 42.576 MHz T⁻¹ for ¹H and 10.705 MHz T⁻¹ for ¹³C. For spin-1/2 nuclei, the common eigenstates of the angular momentum operators I^2 and I_z are called Zeeman eigenstates and are represented by the following symbols:

$$\begin{aligned} |\alpha\rangle &= \left| \frac{1}{2}, +\frac{1}{2} \right\rangle \\ |\beta\rangle &= \left| \frac{1}{2}, -\frac{1}{2} \right\rangle \end{aligned} \tag{2.2}$$

¹More precisely, γ is called magnetogyric ratio. However, this term is less common.

The density operator ρ of a spin ensemble is given by:

$$\rho = N^{-1} \sum_{i=1}^N |\Psi_i\rangle\langle\Psi_i| = \overline{|\Psi\rangle\langle\Psi|}, \quad (2.3)$$

where the overbar indicates the ensemble average. The matrix representation of the density operator for a non-interacting spin-1/2 ensemble is given by

$$\rho = \begin{pmatrix} \rho_{\alpha\alpha} & \rho_{\alpha\beta} \\ \rho_{\beta\alpha} & \rho_{\beta\beta} \end{pmatrix} = \begin{pmatrix} \overline{c_\alpha c_\alpha^*} & \overline{c_\alpha c_\beta^*} \\ \overline{c_\beta c_\alpha^*} & \overline{c_\beta c_\beta^*} \end{pmatrix} \quad (2.4)$$

The diagonal elements are called the populations of states $|\alpha\rangle$ and $|\beta\rangle$, the off-diagonal elements are called coherences. In an external magnetic field along the z-axis with magnitude B_0 , the spin Hamiltonian (in units of \hbar) is given by:

$$\mathcal{H} = -\omega_0 I_z, \quad (2.5)$$

where the Larmor frequency is given by $\omega_0 = \gamma B_0$. The energy E of the eigenstates is therefore given by:

$$E_{\alpha,\beta} = \pm \frac{1}{2} \hbar \omega_0. \quad (2.6)$$

In the thermal equilibrium, the populations of the energy states obey the Boltzmann distribution:

$$\frac{\rho_{\alpha\alpha}}{\rho_{\beta\beta}} = \frac{\exp\left(-\frac{E_\alpha}{k_B T}\right)}{\exp\left(-\frac{E_\beta}{k_B T}\right)}, \quad (2.7)$$

where k_B is the Boltzmann constant. In the high-temperature approximation the density matrix in thermal equilibrium is therefore given by

$$\rho = \begin{pmatrix} \frac{1}{2} + \frac{1}{4}\mathbb{B} & 0 \\ 0 & \frac{1}{2} - \frac{1}{4}\mathbb{B} \end{pmatrix}, \quad (2.8)$$

in which the Boltzmann factor \mathbb{B} is defined by

$$\mathbb{B} = \frac{\hbar\gamma B_0}{k_B T}. \quad (2.9)$$

In terms of spin operators, the density operator for a non-interacting spin-1/2 ensemble at thermal equilibrium is given by

$$\rho = \frac{1}{2}\mathbb{1} + \frac{1}{2}\mathbb{B}I_z \quad (2.10)$$

The macroscopic magnetization and therefore the NMR signal are only given by the difference in the populations which is called polarization P :

$$P_{\text{thermal}} = \rho_{\alpha\alpha} - \rho_{\beta\beta} \approx \frac{1}{2}\mathbb{B}. \quad (2.11)$$

For example, the Boltzmann polarization in a magnetic field of 1.5 T at room temperature is 5.23×10^{-6} for protons and 1.31×10^{-6} for carbon-13.

The Hamiltonian in an isotropic liquid may be written as

$$\mathcal{H} = \mathcal{H}_{CS} + \mathcal{H}_J + \mathcal{H}_{\text{RF}}, \quad (2.12)$$

including the chemical shift term \mathcal{H}_{CS} , the J-coupling term \mathcal{H}_J and the term caused by radiofrequency (RF) pulses \mathcal{H}_{RF} :

$$\begin{aligned} \mathcal{H}_{CS} &= - \sum_j \omega_j^0 I_{jz} \\ \mathcal{H}_J &= 2\pi \sum_{j < k} J_{jk} \hat{I}_j \hat{I}_k \\ \mathcal{H}_{\text{RF}} &= \sum_i (\omega_{\text{rf}}^{I_{ix}} I_{ix} + \omega_{\text{rf}}^{I_{iy}} I_{iy}), \end{aligned} \quad (2.13)$$

where the indices i, j and k label the nuclear spins in one molecule of the liquid. The equation of motion for the density operator, which is based on the Schrödinger equation, is given by

$$\frac{d}{dt}\rho(t) = -i[\mathcal{H}, \rho(t)]. \quad (2.14)$$

It is called the Liouville-von Neumann equation. The effect of an on-resonant RF pulse on the density matrix is

$$\rho_R = R_\phi(\alpha)\rho_0 R_\phi^\dagger(\alpha) \quad (2.15)$$

with $\phi = \tan^{-1}(\frac{\omega_{\text{rf}}^y}{\omega_{\text{rf}}^x})$ being the phase of the pulse and α the flip angle.

For further reading about nuclear magnetic resonance the following literature is recommended: Abragam [1983], Ernst et al. [1990] and Levitt [2008].

2.2 Polarization Transfer

One of the first approaches to overcome the lower polarization of heteronuclei like carbon-13 was to transfer the ^1H polarization to the heteronucleus by RF pulse sequences. One of these pulse sequences is the refocused INEPT sequence (Insensitive Nuclei Enhanced by Polarization Transfer) (Fig. 3.1 on page 22) which is an expansion of the INEPT sequence by Morris and Freeman [1979]. It is based on the scalar coupling J_{IS} between the protons

and the heteronucleus. For the theoretical derivation of the polarization transfer, the position of the simultaneous π pulses is not important. Therefore, they can be ignored in the calculations since they can be collapsed around the $(\frac{\pi}{2})$ pulse couple.

The thermal density operator of the AX spin system is given as:

$$\rho_0 = \frac{1}{4}\mathbb{1} + \frac{1}{4}\mathbb{B}_I I_z + \frac{1}{4}\mathbb{B}_S S_z. \quad (2.16)$$

Since the unity operator is invariant, it will be neglected in the following equations. After the first $(\frac{\pi}{2})_x^I$ pulse, the density operator is transformed to:

$$\rho_1 = -\frac{1}{4}\mathbb{B}_I I_y + \frac{1}{4}\mathbb{B}_S S_z. \quad (2.17)$$

During the delay τ_1 , the spin systems evolves under the J coupling. Choosing $\tau_1 = \frac{1}{2J_{IS}}$, the density operator transforms to:

$$\rho_2 = \frac{1}{4}\mathbb{B}_I I_x S_z + \frac{1}{4}\mathbb{B}_S S_z. \quad (2.18)$$

After the $((\frac{\pi}{2})_y^I, (\frac{\pi}{2})_x^S)$ pulse pair, one achieves:

$$\rho_3 = \frac{1}{4}\mathbb{B}_I I_z S_y - \frac{1}{4}\mathbb{B}_S S_y. \quad (2.19)$$

This evolves during the second delay $\tau_2 = \frac{1}{2J_{IS}}$ to:

$$\rho_4 = -\frac{1}{4}\mathbb{B}_I S_x + \frac{1}{4}\mathbb{B}_S I_z S_x. \quad (2.20)$$

The second term which originates from the initial carbon-13 polarization is canceled by the $\{^1H\}$ decoupling. The first term is proportional to S_x but weighted with the Boltzmann term \mathbb{B}_I of the protons. Therefore, for the Zeeman polarization the maximum enhancement η_{max} is given by the ratio of the gyromagnetic ratios of the protons and the heteronucleus:

$$\eta_{max} = \frac{\mathbb{B}_I}{\mathbb{B}_S} = \frac{\gamma^{1H}}{\gamma^X}, \quad (2.21)$$

which is approximately four for carbon-13. For a two spin system, the optimal delay times are given by:

$$\tau_1 = \tau_2 = \frac{1}{2J_{IS}}. \quad (2.22)$$

The refocusing realized by the last π -pulse couple, converts the generated mixed operator e.g. $I_z S_y$ into a pure heteronucleus operator S_x , enabling for $\{^1H\}$ decoupling during acquisition.

If the polarization transfer is regarded in a multi-spin system, the calculations are more

complicated and therefore are easier performed using numerical evaluations commonly called spin dynamics simulations.

2.3 Parahydrogen Induced Polarization

As mentioned in the introduction, several techniques exist which overcome the low Boltzmann polarization by achieving an enhanced nuclear alignment commonly called hyperpolarization. One of these techniques which is used in the present work is parahydrogen induced polarization (PHIP).

The effect of signal enhancement through hydrogenation with parahydrogen of a target molecule was theoretically predicted by Bowers and Weitekamp [1986]. One year later, this was experimentally proved independently by Bowers and Weitekamp [1987] and Eisenschmid et al. [1987].

Parahydrogen

Hydrogen H_2 as a two spin-1/2 system has two isomers named para- and orthohydrogen. Parahydrogen is the antisymmetric nuclear spin singlet state with total nuclear spin $I = 0$:

$$|S\rangle = \frac{1}{\sqrt{2}}(|\alpha\beta\rangle - |\beta\alpha\rangle). \quad (2.23)$$

Orthohydrogen is the symmetric nuclear spin triplet state with total nuclear spin $I = 1$:

$$\begin{aligned} |T_{+1}\rangle &= |\alpha\alpha\rangle \\ |T_0\rangle &= \frac{1}{\sqrt{2}}(|\alpha\beta\rangle + |\beta\alpha\rangle) \\ |T_{-1}\rangle &= |\beta\beta\rangle \end{aligned} \quad (2.24)$$

Since protons are Fermions, the wavefunction of the hydrogen molecule has to be antisymmetric in exchange of the nuclei. This condition can only be fulfilled by the product of the molecular rotational angular momentum Ψ_{rot} and the nuclear spin angular momentum $\Psi_{\text{nuclear spin}}$. Since Ψ_{rot} is symmetric for rotational states with $j = \text{even}$ (and vice versa), parahydrogen exists only in the even rotational states whereas orthohydrogen only in the odd rotational states. In the high temperature limit, the ratio of the number of ortho- and parahydrogen molecules is $N_{\text{ortho}}/N_{\text{para}} \rightarrow 3$, the low temperature limit is $N_{\text{ortho}}/N_{\text{para}} \rightarrow 0$. By cooling hydrogen in the presence of active charcoal, parahydrogen can be enriched (e. g. to 93% at 35 K). Herein, active charcoal allows the system to reach the thermodynamical equilibrium within minutes. Since the conversion of para- to orthohydrogen in the absence of active charcoal is very slow, the enriched parahydrogen can be stored at room temperature.

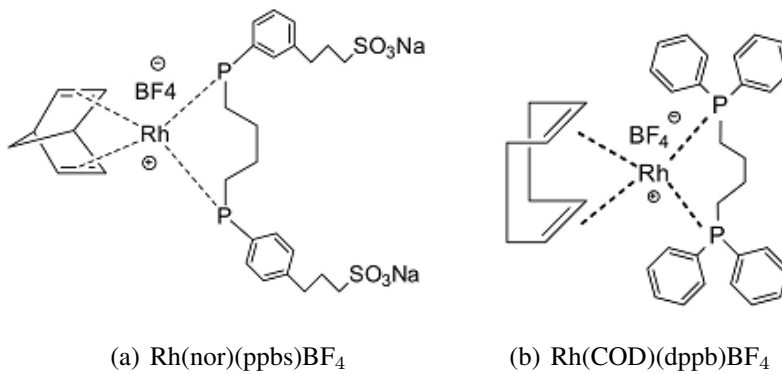


Figure 2.1: Homogeneous Catalyst Systems.

Density Operator

The density operator of parahydrogen is given by:

$$\rho_{\text{para}} = \frac{1}{2} (|\alpha\beta\rangle - |\beta\alpha\rangle) (\langle\alpha\beta| - \langle\beta\alpha|). \quad (2.25)$$

Using the product operator formalism, this can be expressed as:

$$\rho_{\text{para}} = \frac{1}{4} \mathbb{1} - (I_{1x}I_{2x} + I_{1y}I_{2y} + I_{1z}I_{2z}), \quad (2.26)$$

where the term which is proportional to the unity operator can be neglected. A brief summary of the product operator formalism can be found in the appendix (Section 7.3 on page 100).

Hydrogenation

Hyperpolarization can be achieved by the hydrogenation of an unsaturated molecule with parahydrogen. For this purpose, a catalyst is required which pairwise and simultaneously transfers the two protons keeping the relative spin orientation. In this work, two homogeneous catalyst complexes with Rhodium as metal center were used (Fig. 2.1). The water-soluble catalyst Rh(nor)(ppbs)BF₄ was used to hydrogenate hydroxyethyl acrylate to hydroxyethyl propionate. Rh(COD)(dppb)BF₄ was used to hydrogenate the dimethyl acetylenedicarboxylate to dimethyl maleate soluted in acetone. A further description of the catalyst can be found in the literature (e. g. Roth [2009]).

After the simultaneous transfer of the two parahydrogen protons, the molecule is in the spin state given by equation 2.26 (neglecting Boltzmann contributions of the other spins in the molecule). Since the reaction is performed over a certain duration, the density operator of the entire ensemble has to be averaged over this duration [Natterer and Bargon, 1997].

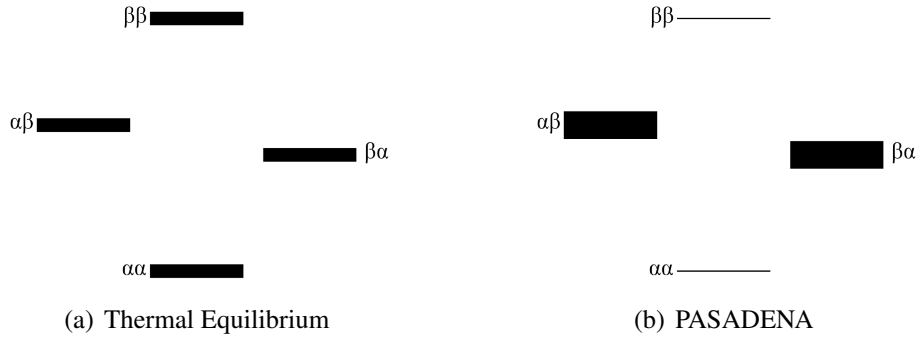


Figure 2.2: Populations of the energy levels in the AX spin system in (a) thermal equilibrium and (b) PASADENA. The populations are depicted by the thickness of the energy levels. In the thermal equilibrium the population difference is only in the order of 10^{-6} and therefore not visible in the diagram.

For a two spin system, this leads to:

$$\rho = \frac{1}{4}\mathbb{1} - \left(I_{1z}I_{2z} + \frac{1}{\xi^2 + 1}(I_{1x}I_{2x} + I_{1y}I_{2y}) + \frac{\xi}{2(\xi^2 + 1)}(I_{1z} - I_{2z}) \right), \quad (2.27)$$

with $\xi = \frac{\nu_1 - \nu_2}{J_{12}}$, where ν_1 and ν_2 are the resonance frequencies of the two former parahydrogen protons in the molecule and J_{12} is the scalar coupling between them.

PASADENA

If the hydrogenation is performed in a high magnetic field, the two former pH₂ spins are weakly coupled (AX spin system). The hydrogenation with pH₂ under high field conditions is commonly called PASADENA (Parahydrogen and Synthesis Allow Dramatic Enhancement of Nuclear Alignment). The density operator of equation 2.27 can be simplified to:

$$\rho_{AX} = \frac{1}{4}\mathbb{1} - I_{1z}I_{2z}. \quad (2.28)$$

More pictorial, this can be described in the energy level diagram (cf. Fig. 2.2). Under PASADENA conditions, only energy levels of the spin states $|\alpha\beta\rangle$ and $|\beta\alpha\rangle$ are populated by the hydrogenation with pH₂ which yields a huge population difference of the energy levels. The density matrix is therefore given by

$$\rho_{AX} = \frac{1}{2}(|\alpha\beta\rangle\langle\alpha\beta| + |\beta\alpha\rangle\langle\beta\alpha|), \quad (2.29)$$

which formulated in the product operator formalism of course leads to the result of equation 2.28.

ALTADENA

A different spin state is achieved if the reaction is performed at low field followed by an adiabatic transport of the sample into the high field of the NMR system. This experiment is commonly called ALTADENA (Adiabatic Longitudinal Transport After Dissociation Engenders Nuclear Alignment).

At low magnetic field, the protons are strongly coupled (AB spin system). Hence, the system stays in the singlet spin state which is an eigenfunction of the strongly coupled spin system. By the adiabatic transfer, the system remains in a state corresponding to an eigenfunction of the Hamiltonian. Thus, only the energetically favored spin states of $|\alpha\beta\rangle$ and $|\beta\alpha\rangle$ become populated in the AX spin system at high field (e. g. in the diagram shown in figure 2.2 only $|\beta\alpha\rangle$).

The density operator achieved by the ALTADENA experiment is therefore:

$$\rho_{\text{alta}} = |\alpha\beta\rangle\langle\alpha\beta| \text{ or } \rho_{\text{alta}} = |\beta\alpha\rangle\langle\beta\alpha|. \quad (2.30)$$

In terms of spin operators, this can be expressed as:

$$\rho_{\text{alta}} = \frac{1}{4}\mathbb{1} - \left(I_{1z}I_{2z} \pm \frac{1}{2}(I_{1z} - I_{2z}) \right), \quad (2.31)$$

in which the upper sign correspond to the case $J_{12}(\nu_1 - \nu_2) < 0$.

Signal Enhancement

Calculating the maximal signals for the thermal equilibrium and for the PASADENA experiment, Natterer and Bargon [1997] found a maximum theoretical signal enhancement of

$$\eta = \left| \frac{k_B T (1 - 4a)}{6\hbar\gamma B_0} \right| = \left| \frac{1 - 4a}{6\mathbb{B}} \right|, \quad (2.32)$$

with a being the fraction of parahydrogen in the hydrogen gas. For example, a maximum signal enhancement by a factor of 43 000 is predicted for the ^1H signal at 1.5 T using 93% enriched parahydrogen. By polarization transfer to the heteronucleus ^{13}C , an even four times higher signal enhancement is expected due to the lower gyromagnetic ratio.

2.4 Relaxation

If a spin ensemble is allowed to be undisturbed for a long time, it is arranged in the state of thermal equilibrium which for the non-interaction spin-1/2 ensemble was given in equation 2.8. After an RF pulse, often coherences are generated and populations are changed. Relaxation pushes the system to return to the thermal equilibrium, i. e. to the population values

described by the Boltzmann distribution and to zero coherences. Relaxation processes are divided into two types:

Spin-Lattice Relaxation

This spin-lattice relaxation, also called longitudinal relaxation, causes the re-establishment of the population values in thermal equilibrium. It is based on an energy transfer of the excited spin system with the lattice, i. e. the remaining degrees of freedom of the entire quantum mechanical system. In the non-interacting spin-1/2 ensemble, the longitudinal relaxation is characterized by the spin-lattice relaxation time constant T_1 . The motion of the longitudinal component of the net magnetization vector is given by

$$M_z(t) = \left(M_z(t=0) - M_z^{\text{thermal}} \right) \exp\left(-\frac{t}{T_1} \right) + M_z^{\text{thermal}}. \quad (2.33)$$

Spin-Spin Relaxation

The spin-spin relaxation, also called transverse relaxation, is concerned with the decay of coherences. The coherence loss is caused by random fluctuations of the local magnetic field which lead to random variations in the instantaneous NMR precession frequency. In the non-interacting spin-1/2 ensemble, the transverse relaxation is characterized by the transverse relaxation time constant T_2 . The temporal evolution of the transverse components of the net magnetization vector in the rotating frame follows

$$M_{x,y}(t) = M_{x,y}(t=0) \exp\left(-\frac{t}{T_2} \right) \quad (2.34)$$

Relaxation Mechanisms

The physical mechanism of relaxation is based on the fluctuating magnetic fields at the sites of the nuclear spins, caused by thermal motion of the molecules. The most important mechanisms for spins-1/2 generating local magnetic fields are

- Dipole-Dipole Coupling
- Chemical Shift Anisotropy

The dipole-dipole coupling is based on the magnetic field of one spin on another. Due to the molecular tumbling, the magnitude and direction of this magnetic field changes. The relaxation rates caused by dipole-dipole couplings are proportional to the square of the dipole-dipole coupling constant b^2 and hence depend on the inverse sixth power of the internuclear distance r^{-6} .

The chemical shift of nuclei is caused by the induced local magnetic fields generated by the electrons in an external magnetic field. This induced magnetic field has components

not only parallel to the external magnetic field B_0 which is described by the chemical shift tensor. The chemical shift anisotropy (CSA) is defined by the largest deviation in the chemical shift from the isotropic value. This anisotropy causes fluctuating magnetic fields as the molecule tumbles. The chemical shift anisotropy relaxation rate is proportional to the square of the magnetic field B_0^2 .

2.5 Spin Dynamics Simulations

Spin dynamics simulations are based on a numerical evaluation of the Liouville-von Neumann equation (Eq. 2.14). The formal solution of the Liouville-von Neumann equation may be written as

$$\rho(t) = U(t, 0)\rho(0)U^\dagger(t, 0), \quad (2.35)$$

where $\rho(0)$ is the density operator describing the initial spin state and $U(t, 0)$ is the unitary propagator defined by the Hamiltonian according to

$$U(t, 0) = \hat{T} \exp \left[-i \int_0^t \mathcal{H}(t') dt' \right], \quad (2.36)$$

with \hat{T} being the Dyson time-ordering operator relevant for Hamiltonians containing non-commuting components. This integral can numerically be approximated by a simple time-ordered product

$$U(t, 0) = \prod_{j=0}^{n-1} \exp \left[-i\mathcal{H}(j\Delta t) \right]. \quad (2.37)$$

Herein, the duration from 0 to t is divided in n small isochronous time intervals Δt over each of which the Hamiltonian may be considered time-independent. The exponentiation of the single time intervals is accomplished by diagonalization of the matrix representation for the Hamiltonian.

The spin dynamic simulations in the present work were performed with the SIMPSON software package by Bak et al. [2000].

2.6 Imaging

In the following, the main features of magnetic resonance imaging are illustrated. A more detailed description can be found in the literature, e. g. Mansfield and Morris [1982], Haacke et al. [1999], Liang et al. [2000] and Bernstein et al. [2004].

Magnetic resonance imaging is based on the spatial variation of the z component of the magnetic field B_0 by a magnetic field gradients G . This causes a spatial variation of the resonance frequency. Generally, the spatial encoding can be divided into these steps:

the slice selection, the phase encoding and the frequency encoding. The corresponding gradients need to be linearly independent. For simplification in the following, the slice selection gradient points towards the z axis, the phase encoding gradient towards the y axis and the frequency encoding gradient towards the x axis.

Slice Selection

The slice selection leads to an excitation of spins perpendicular to the slice selection gradient. The resonance frequency is modulated due to the slice selection gradient:

$$\omega(z) = \gamma(B_0 + G_z z) \quad (2.38)$$

The transmission of an RF pulse with frequency ω_{rf} and frequency bandwidth $\Delta\omega$ yields an excitation of the spins in the slice positioned at

$$z = \frac{\omega_{\text{rf}} - \gamma B_0}{\gamma G_z} \quad (2.39)$$

with thickness Δz

$$\Delta z = \frac{\Delta\omega}{\gamma G_z}. \quad (2.40)$$

A temporal modulation of the RF pulse amplitude by a sinc-function leads to a rectangular slice profile.

Phase Encoding

The spatial encoding in the excited slice is achieved by two additional magnetic field gradients. The phase encoding gradient G_y is switched on for a duration T_y between excitation and acquisition. During the phase encoding gradient the spins accumulate a phase depending on their position in y direction:

$$\phi(y) = \gamma \int_0^{T_y} G_y(t) y dt \quad (2.41)$$

The spatial encoding in the phase encoding direction is yielded by repeating the measurement N_y times with a linear incrementation e. g. of the gradient amplitude from $-G_{y,max}$ to $+G_{y,max}$ at a constant duration T_y .

Frequency Encoding

The frequency encoding gradient is switched on during the acquisition. This yields a temporal phase variation during the acquisition which depends on the position in x direction:

$$\phi(x, t_x) = \gamma \int_0^{t_x} G_x(t)x dt \quad (2.42)$$

Image Reconstruction

The dependency of the signal intensity S caused by the phase and frequency encoding is given by

$$S(t_x, T_y) \propto \int \int \left[\rho(x, y) \exp \left(-i \left(\gamma \int_0^{t_x} G_x(t)x dt + \gamma \int_0^{T_y} G_y(t)y dt \right) \right) \right] dx dy, \quad (2.43)$$

with $\rho(x, y)$ the spatial depending spin density. Using the substitutions

$$\begin{aligned} k_x &= \gamma \int_0^{t_x} G_x(t) dt \\ k_y &= \gamma \int_0^{T_y} G_y(t) dt \end{aligned} \quad (2.44)$$

yields the representation of the signal intensity in the so-called k-space:

$$S(k_x, k_y) \propto \int \int \left[\rho(x, y) \exp \left(-i(k_x x + k_y y) \right) \right] dx dy. \quad (2.45)$$

The image reconstruction is therefore performed by an inverse two-dimensional fourier transformation of the acquired signal:

$$\rho(x, y) \propto \mathcal{F}^{-1}[S(k_x, k_y)] = \int \int \left[S(k_x, k_y) \exp \left(i(k_x x + k_y y) \right) \right] dk_x dk_y. \quad (2.46)$$

Pulse Sequences

The pulse sequences used for magnetic resonance imaging are in principle dividable into spin echo (SE) sequences and gradient echo (GRE) sequences (Fig. 2.3). In a spin echo sequence, the echo is generated by a 180° pulse [Hahn, 1950]. In a gradient echo sequence, the echo is generated by a dephasing gradient in frequency encoding direction with half gradient moment. The subsequent frequency encoding gradient rephases the spins by what a phase coherence is achieved during the acquisition at the echo time TE.

The signal equation for a repeated spin-echo sequence as a function of the repetition time TR, and the echo time TE for a non-interacting spin ensemble at thermal equilibrium

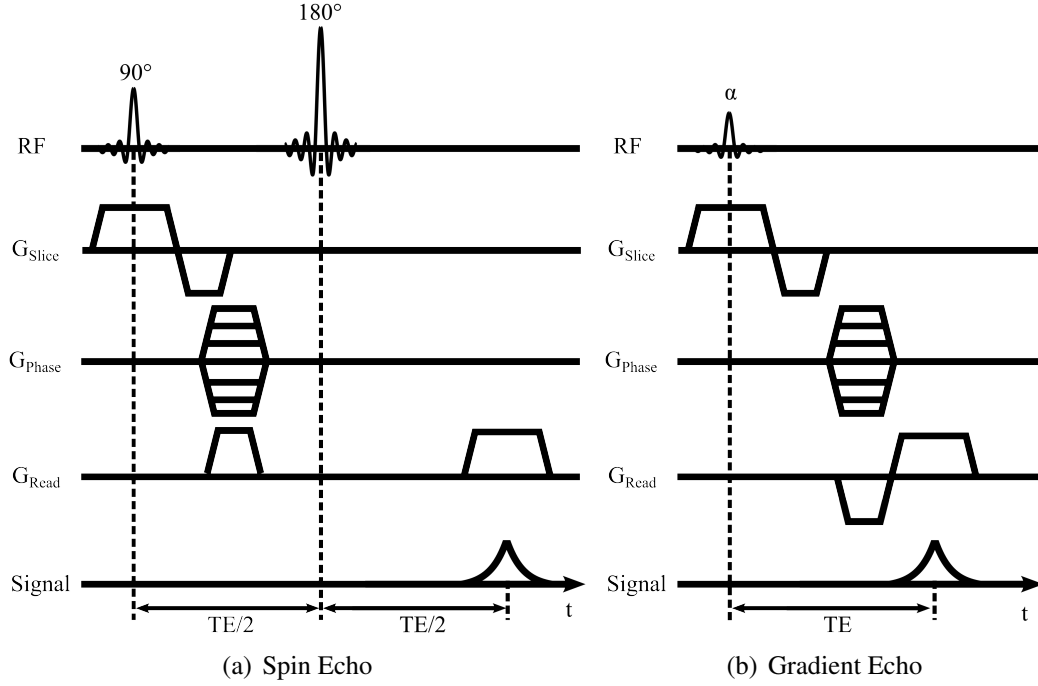


Figure 2.3: Basic Sequences.

is

$$S_{SE} \propto \left[1 - \exp\left(-\frac{TR}{T_1}\right) \right] \exp\left(-\frac{TE}{T_2}\right), \quad (2.47)$$

with T_1 being the longitudinal relaxation time and T_2 the transverse relaxation time. In contrast, the signal equation for a repeated gradient echo sequence using an excitation pulse with flip angle α is

$$S_{GRE} \propto \sin(\alpha) \frac{1 - \exp\left(-\frac{TR}{T_1}\right)}{1 - \cos(\alpha) \exp\left(-\frac{TR}{T_1}\right)} \exp\left(-\frac{TE}{T_2^*}\right), \quad (2.48)$$

with T_2^* being the time constant of the loss of phase coherence caused by a combination of magnetic field inhomogeneities and transverse relaxation. A detailed analysis of these signal equations and the optimization e. g. of the flip angle α in the GRE sequence can be found in the literature recommended above.

In the following the differences in the signal behavior of PHIP hyperpolarized molecules are pointed out. Using a spin system at thermal equilibrium, the signal increases with increasing repetition time TR since more longitudinal magnetization is recovered between two excitation pulses. In contrast, the hyperpolarization decays with the longitudinal relaxation. Therefore, a minimum possible repetition time TR should be used for imaging of hyperpolarized molecules.

Hyperpolarized molecules are normally more complex spin systems with different chemical shifts and J-couplings. Hence, the echo time dependence is not just an exponential

function like it is for a non-interaction spin ensemble like water which has the main contribution at *in vivo* imaging [Dechent et al., 2012]. The echo time behavior was therefore analyzed for both molecules used in the present work which can be found in section 3.2.3 and section 4.4.

Chapter 3

Heteronuclear Polarization Transfer

Contents

3.1	Theory / Previous Work	20
3.2	PH-INEPT+ Sequence	21
3.2.1	Sequence Timing Optimization	22
3.2.2	Implementation on a Clinical MRI System	30
3.2.3	Combination with MR Imaging	35
3.3	Optimal Control	40
3.3.1	Theory	40
3.3.2	Optimization of Polarization Transfer using OC Theory	42
3.3.3	Off-resonance Stabilization	47
3.4	Discussion	50
3.4.1	Hollow-Fiber Membrane Modules	50
3.4.2	Hyperpolarized ^{13}C Spin State	50
3.4.3	Polarization Transfer Sequence	51
3.4.4	Optimal Control	53
3.4.5	Imaging	53
3.4.6	^{13}C Labeling / Deuteration	54

This part of the PhD thesis deals with the transfer of the PHIP hyperpolarized ^1H spin state to the heteronucleus ^{13}C . The heteronucleus ^{13}C has a four times lower gyromagnetic ratio ($\gamma^{13\text{C}} \approx 0.25 \times \gamma^{1\text{H}}$) and a natural abundance of only 1%. This results in a relative sensitivity in comparison to protons of only 0.0159. To overcome the low natural abundance, for *in vivo* MRI and NMR spectroscopy often ^{13}C labeled compounds are used. Alternatively or in combination with isotope labeling, hyperpolarization of ^{13}C provides a huge improvement in sensitivity, especially for *in vivo* applications. In section 3.1 the previous

work in the field of $^1\text{H}/^{13}\text{C}$ polarization transfer of PHIP hyperpolarized proton spin states is briefly summarized. Section 3.2 treats the analysis and optimization of the PH-INEPT+ sequence, its implementation on a clinical MRI system, and the combination with an imaging sequence. In section 3.3 the polarization transfer is optimized using optimal control theory. Finally, the results of this chapter are discussed in section 3.4.

3.1 Theory / Previous Work

To analyze the polarization transfer from the PHIP hyperpolarized protons to ^{13}C , at least a 3-spin system needs to be considered with the two pH_2 proton spins and the ^{13}C nuclear spin. For liquid samples, the spin Hamiltonian (in units of \hbar) is given by:

$$\mathcal{H} = -\omega_{\text{H},1}I_{1,z} - \omega_{\text{H},2}I_{2,z} - \omega_{\text{C}}I_{3,z} + 2\pi \sum_{i<j} J_{ij} \hat{I}_i \cdot \hat{I}_j. \quad (3.1)$$

The first three terms correspond to the Zeeman interaction for each nucleus and the fourth represents the scalar coupling between each pair of nuclei. The product is given by:

$$\hat{I}_i \cdot \hat{I}_j = I_{i,x}I_{j,x} + I_{i,y}I_{j,y} + I_{i,z}I_{j,z}. \quad (3.2)$$

In a good approximation, for weak coupling, i.e. if $2\pi|J_{ij}| \ll |\omega_i - \omega_j|$, one can retain only the secular components of the scalar coupling Hamiltonian ($\propto I_{iz}I_{jz}$). Three magnetic field regimes can be distinguished, for which the Hamiltonian can be simplified:

- 'Zero' field
- Low field
- High field

In the 'Zero' field regime which is practically very close to 0 T, such that $\omega_i \ll J_{jk} \forall i, j, k$, the spin system can be classified an AA'A' system. In this magnetic field range, the Zeeman terms can be neglected and the Hamiltonian (Eq. 3.1) can be simplified to:

$$\mathcal{H}_{\text{Zero}} = 2\pi \sum_{i<j} J_{ij} \hat{I}_i \cdot \hat{I}_j \quad (3.3)$$

The low field regime is the magnetic field range where the protons are still strongly coupled but the proton carbon coupling is already weak ($|\omega_{\text{H},1} - \omega_{\text{H},2}| \ll 2\pi|J_{ij}| \ll |\omega_{\text{H},i} - \omega_{\text{C}}|$, $\forall i, j, k$). This is termed an AA'X spin system and the Hamiltonian can be simplified to:

$$\mathcal{H}_{\text{Low}} = -\omega_{\text{H},1}I_{1,z} - \omega_{\text{H},2}I_{2,z} - \omega_{\text{C}}I_{3,z} + 2\pi(J_{12}\hat{I}_1 \cdot \hat{I}_2 + J_{13}I_{1,z}I_{3,z} + J_{23}I_{2,z}I_{3,z}) \quad (3.4)$$

In the high field regime all nuclei are weakly coupled. In this range, the system is an ABX spin system and the Hamiltonian is given by:

$$\mathcal{H}_{\text{High}} = -\omega_{\text{H},1}I_{1,z} - \omega_{\text{H},2}I_{2,z} - \omega_{\text{C}}I_{3,z} + 2\pi \sum_{i<j} J_{ij}I_{i,z}I_{j,z} \quad (3.5)$$

The polarization transfer from the PHIP hyperpolarized proton spin state to a heteronucleus can be categorized in two methods:

- Static Field Cycling
- Polarization Transfer Pulse Sequences

The static field cycling method [Aime et al., 2003, Johannesson et al., 2004, Goldman et al., 2005, Korchak et al., 2009] involves two consecutive steps. First, the field is suddenly changed to zero. This reduces the density matrix to the projection of its initial form on the zero-field Hamiltonian eigenstates. Second, the field is adiabatically increased, during which the populations follow the time-dependent eigenstates.

The pulse sequence methods are related mainly to the INEPT sequence (Insensitive Nuclei Enhanced by Polarization Transfer) [Morris and Freeman, 1979]. They are based on a combination of pulses on both nuclei (^1H and ^{13}C) and free evolution periods utilizing the mixing of the spin operators due to the J-coupling network. Sequences were developed for the polarization transfer from PHIP hyperpolarized protons to ^{13}C applied at the low field regime [Goldman and Johannesson, 2005, Kadlecik et al., 2010] and at the high field regime [Haake, Natterer, and Bargon, 1996]. The sequences in the low field regime were created for use in an external polarizer, e.g. built by Hövener et al. [2009]. Such a polarizer consists among other things of a reaction chamber for the hydrogenation embedded inside a low field NMR unit. Although this system works quite well, a lot of additional hardware is needed in comparison to a normal NMR experiment. Therefore, we decided to realize the polarization transfer in the high field regime of the NMR spectrometer or MRI scanner utilizing no more than a double resonant $^1\text{H}/^{13}\text{C}$ coil which is anyway needed for the measurements.

3.2 PH-INEPT+ Sequence

There are several pulse sequences for polarization transfer from protons to carbon-13. One of these is the refocused INEPT sequence (Fig. 3.1 on the following page), which was described in section 2.2 on page 7. Due to the different initial density operator after the PHIP reaction, Haake et al. [1996] modified this sequence by replacing the first proton $(\frac{\pi}{2})_x$ pulse by a $(\frac{\pi}{4})_y$ pulse and named it PH-INEPT+ sequence. However, a detailed analysis of the sequence timing is still missing. Therefore, the aim of this study is to analyze and

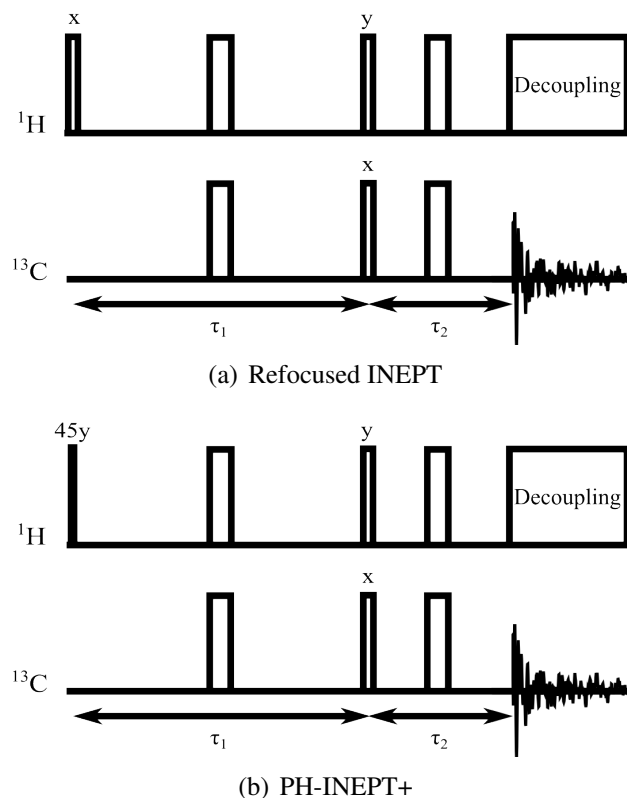


Figure 3.1: Polarization transfer sequences.

optimize the PH-INEPT+ sequence timing for hydroxyethyl propionate (HEP). HEP is a common used molecule for *in vivo* applications of PHIP since it is water soluble and can be generated from hydroxyethyl acrylate (HEA) by a water-soluble catalyst.

3.2.1 Sequence Timing Optimization

Spin Dynamics Simulations

The numerical simulations (as described in section 2.5 on page 14) were performed for the HEP molecules with carbon-13 at the first or second position ($^{13}\text{C}_1$ -HEP and $^{13}\text{C}_2$ -HEP) (see Fig. 3.2 on the next page). In the calculations, the three protons in the methyl group, the two protons in the methylene group and the Carbon-13 nucleus were taken into account, resulting in a 6-spin system. The ^1H pulses were applied on the frequency between resonance of the methyl and the methylene group. In the carbon channel, the carrier frequency was set on-resonant with the $^{13}\text{C}_1$ frequency. The J-coupling networks of the two spin systems are listed in table 3.1 on the facing page.

The magnetic field was set to 7 T and the RF strengths of the pulses to 2.17 kHz and 5 kHz, respectively, being the same values as used in the experimental measurements. The

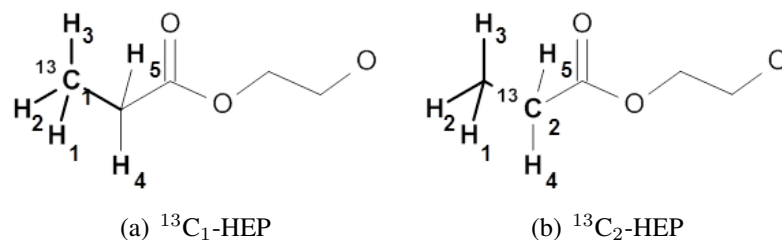


Figure 3.2: Hydroxyethyl-propionate with ^{13}C at (a) the first and (b) the second position. For the spin dynamics simulations the ^{13}C spin and the spins of the numbered protons were considered.

Table 3.1: Simulated spin systems. On the left, the differences δ between the carrier frequencies of the pulses and the resonance frequencies are shown in ppm. On the right the J-coupling values are listed.

$^{13}\text{C}_1$ -HEP	$I_{1,2,3}$	$I_{4,5}$	S
$I_{1,2,3} \delta = 0.66p$		7.6 Hz	128 Hz
$I_{4,5} \delta = -0.66p$			4.65 Hz
$S \delta = 0$			
$^{13}\text{C}_2$ -HEP	$I_{1,2,3}$	$I_{4,5}$	S
$I_{1,2,3} \delta = 0.66p$		7.6 Hz	4.65 Hz
$I_{4,5} \delta = -0.66p$			129.1 Hz
$S \delta = 18.94p$			

initial density operator for the two spin systems is given by:

$$\rho_0 = I_{1z}I_{4z}, \quad (3.6)$$

with the indices 1 and 4 specifying the pH_2 protons added to the molecule by the hydrogenation of hydroxyethyl acrylate (HEA). The polarization transfer efficiency is given by the projection of the final density operator $\rho(T)$ on to the carbon spin ladder operator S_+ :

$$s = \text{Tr}(S_+\rho(T)) \quad (3.7)$$

The PH-INEPT+ sequence was simulated with spin dynamics simulations using a 2D loop of the τ delays with τ_1 varying from 0.25 to 70 ms and τ_2 from 0.2 to 25 ms using a step size of 0.25 ms and 0.1 ms, respectively. To compare the results with the polarization transfer achieved for thermally polarized protons, simulations were additionally performed using the refocused INEPT sequence starting with the thermal density operator.

The results of the spin dynamics simulations are shown in figure 3.3 on the next page. Clearly, these plots show that there is an important difference between the polarization transfer of thermally polarized protons and that of the PHIP spin state. In the thermal case the global polarization transfer optimum is reached at the first local τ_1 optimum, in the PHIP case the fourth local τ_1 optimum at 27.4 ms is the global optimum. This fact is apparent in both simulated spin systems. However, due to the different symmetry of the spin systems, they show different τ_2 dependencies. Whereas the $^{13}\text{C}_1$ -HEP spin system produces an alternation of two positive and two negative optima, the $^{13}\text{C}_2$ -HEP spin system shows a change of sign between every optimum. The overlaying small oscillations in the results for the $^{13}\text{C}_2$ -HEP spin system are an off-resonance phenomenon since the ^{13}C were applied on-resonant with the $^{13}\text{C}_1$ frequency. The difference in the maximal amplitude of the optima in the thermal (Max: 1) and PHIP simulations (Max: 0.05) is due the different norms of the initial density operator:

$$\left\| \sum_{i=1}^5 I_{iz} \right\| = 20 \|I_{1z}I_{2z}\| \quad (3.8)$$

Experimental Validation

The aim of this section is to validate the spin dynamic results found for the PH-INEPT+ sequence timing. The hydrogenation with pH_2 is usually carried out by vigorous shaking of the NMR tube pressurized with parahydrogen and subsequent fast transfer of the tube into the spectrometer or by bubbling parahydrogen into the NMR tube being placed inside the spectrometer. Both methods only show a limited suitability for the validation of

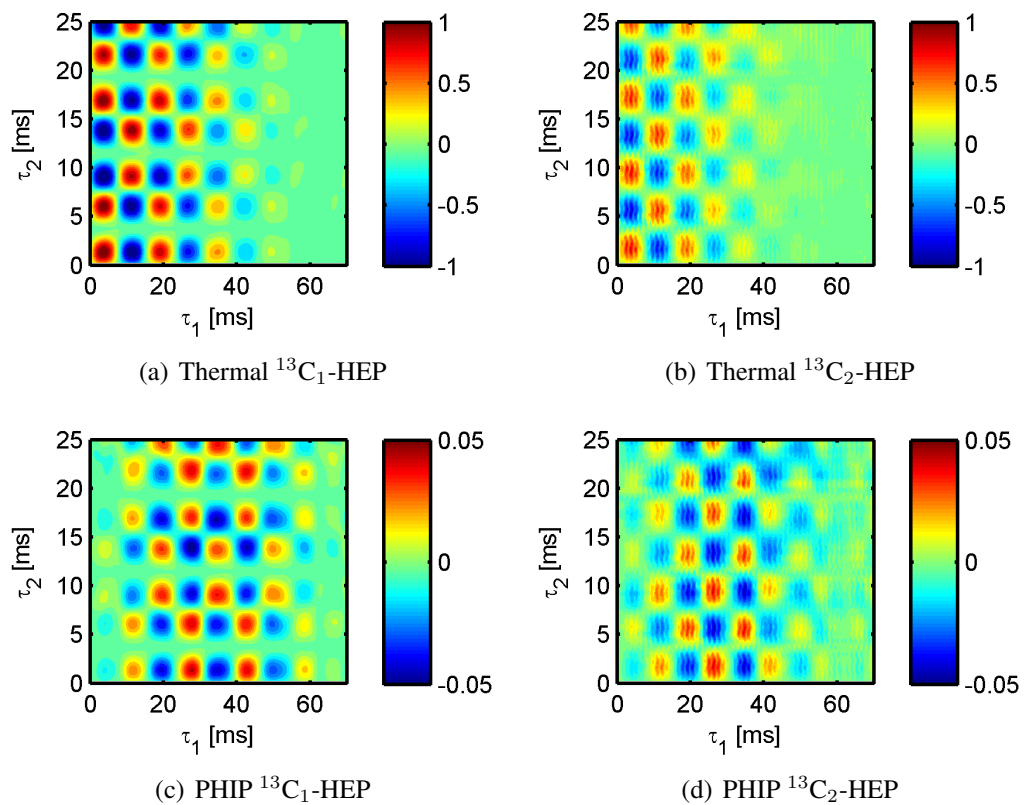


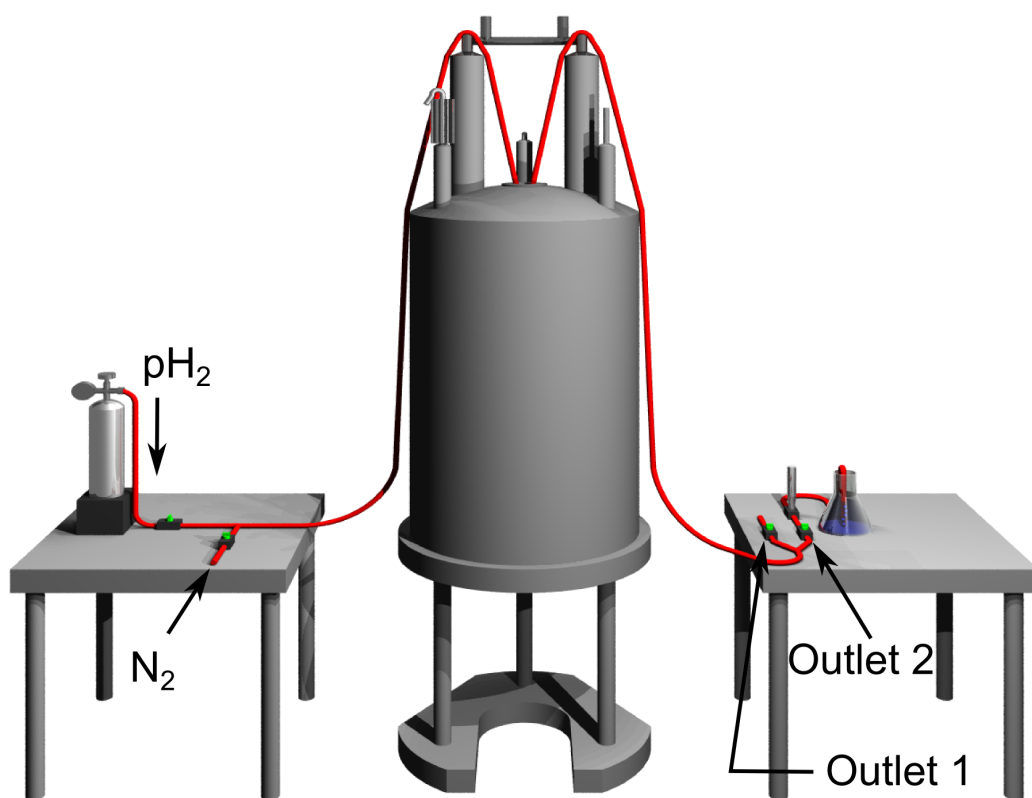
Figure 3.3: Numerical simulations of polarization transfer from ^1H to ^{13}C with different τ delays. At the top the polarization transfer efficiencies are shown for thermally polarized protons using the refocused INEPT sequence, at the bottom for the PHIP protons using the PH-INEPT+ sequence. (a) and (c) for the $^{13}\text{C}_1$ -HEP spin system, (b) and (d) for the $^{13}\text{C}_2$ -HEP spin system.

the sequence timing optimization. The shaking method has the limitation that the reaction is carried out at a lower magnetic field outside the spectrometer. Consequently, the spin system is in a mixture of the ALTADENA and the PASADENA spin states, which therefore leads to a initial density operator that is different from that assumed in the simulations. The bubbling method can realize a continuous hyperpolarization at high magnetic field, but the bubbling needs to be stopped before each acquisition since the bubbles cause strong susceptibility artifacts. To overcome these limitations, a relatively new method was used, which utilizes hollow-fiber membrane modules enabling a continuous dissolution of parahydrogen in the reaction mixture during the measurement [Roth et al., 2010a].

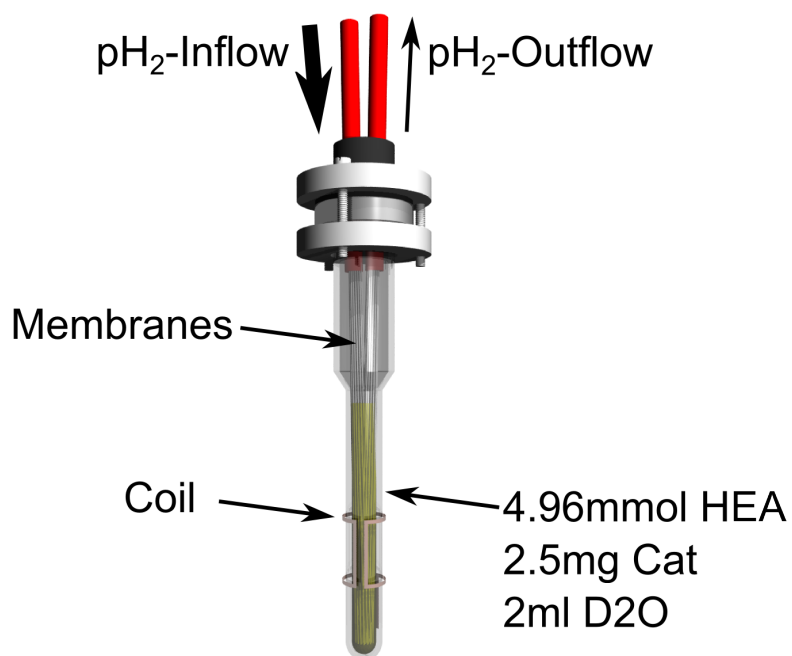
For this purpose, hydrophobic membranes were used, which are composed of polypropylene for use in aqueous systems (Celgard X50, Membrana GmbH, Wuppertal, Germany). They were bended in the middle and glued into two pipes fixed in a cap of an NMR pressure tube. Therefore, in contrast to Roth et al. [2010a] the membrane setup was equipped with an inlet and an outlet (cf. Fig. 3.4). The outlet was mainly used for an initial filling of the membranes with parahydrogen at the beginning of the experiments. The inlet of the module was equipped with a parahydrogen and a nitrogen inflow. The nitrogen was used to test the module for leakage and to clean the pipes from parahydrogen before connecting the next sample. The outlet was split into two pipes. One was used as an 'open end' to enable fast filling of the inflow pipe and the membrane module with parahydrogen at the beginning of the experiment. The second outlet was equipped with a bellows-sealed metering valve (Swagelok, Ohio, USA) to allow for a tiny flow during the whole experiment which was visualized by bubbling in a water-filled flask. All other valves, pipes and connectors used are from Festo (Festo AG & Co.KG, Esslingen Germany). The hydrogenation with pH_2 was performed at room temperature.

The experimental validation was done for two τ_1 variations with $\tau_2 = 1.5$ ms and $\tau_2 = 14$ ms, and two τ_2 variations with $\tau_1 = 27.4$ ms and $\tau_1 = 34.6$ ms. For every experiment, four transportable one-liter aluminum cylinders were filled with 93% enriched parahydrogen at 4 bar. The NMR pressure tube was filled with 2.5 mg of the water-soluble catalyst, 4.96 mmol of 2-hydroxyethyl acrylate, and 2 ml of D_2O .

The experiments were performed on a Bruker AVANCE spectrometer equipped with a 7 T magnet. The carrier frequencies of the pulses were adjusted as used in the simulations (1H : between the methyl and the methylene group, ^{13}C : onresonant on the first carbon of the HEP molecule). The RF strength was 2.17 kHz and 5 kHz for the 1H and the ^{13}C channel, respectively. During acquisition on ^{13}C , a 1H WALTZ decoupling scheme was applied. Since the amount of hyperpolarized molecules depends on the reaction rate, which is not constant over the complete reaction period, two reference measurements were repeated several times during the measurement. The first reference (1H -Ref) is a 1H -FID (free induction decay) using a 45° excitation pulse, the second reference (^{13}C -Ref) the PH-INEPT+



(a) In- and outflow pipes



(b) Membrane module inside an NMR pressure tube

Figure 3.4: Experimental setup. In (a) the parahydrogen and the nitrogen inlets are shown as well as the the two outlets. In (b) the NMR pressure tube with inserted hollow-fiber membrane module is shown.

sequence using the delay of the corresponding τ variation for which the simulations predict the maximum signal. For the τ_1 variations the τ_1 delay was varied between 1 ms and 20 ms in 2.5 ms steps. For the τ_2 variations the τ_2 delay was varied between 1 ms and 20 ms in 1 ms steps. For every experiment the following measurement cycle was used: First, four ^1H -Ref and ^{13}C -Ref were measured alternately. After the first reference pair, the inflow pipe and the membrane module was filled with parahydrogen by opening the valve of the 'open end' for 5 s. Afterwards, the cycle ' ^1H -Ref – PH-INEPT+ – ^{13}C -Ref – PH-INEPT+' was repeated until every τ value of the delay variation was measured four times (48 cycles for the τ_1 variations and 40 cycles for the τ_2 variations). Finally, the ^1H -Ref and the ^{13}C -Ref measurements were alternately acquired until the HEA was completely hydrogenated. A delay of 15 s was used between subsequent measurements.

The peaks of the ^{13}C spectra using the PH-INEPT+ sequence arise not only from polarization transfer of the hyperpolarized protons but also - due to some hardware imperfections - from the thermally polarized protons. The latter contribution is proportional to the amount of HEP which was calculated indirectly by the integral I_{DB} over the double bond protons in the ethylene group of the HEA molecule. The peak amplitudes $A(t, \tau_1, \tau_2)$ were corrected with this thermal offset and, additionally, normalized with the offset corrected amplitude of the ^{13}C -Ref spectra $A_{\text{C}}(t, \tau_{1,\text{ref}}, \tau_{2,\text{ref}})$:

$$A_{\text{C}}(t, \tau_1, \tau_2) = \frac{A(t, \tau_1, \tau_2) - A_{\text{Th}}(t, \tau_1, \tau_2)}{A_{\text{C}}(t, \tau_{1,\text{ref}}, \tau_{2,\text{ref}})}. \quad (3.9)$$

The thermal contribution A_{Th} was calculated as follows:

$$A_{\text{Th}}(t, \tau_1, \tau_2) = A_{\text{Th}}(t_{\infty}, \tau_{1,\text{ref}}, \tau_{2,\text{ref}}) \left(1 - \frac{I_{\text{DB}}(t)}{I_{\text{DB},0}}\right) \frac{\tilde{A}_{\text{Th}}(\tau_1, \tau_2)}{\tilde{A}_{\text{Th}}(\tau_{1,\text{ref}}, \tau_{2,\text{ref}})}, \quad (3.10)$$

where the first factor on the right side is the peak amplitude in the ^{13}C -reference spectrum after HEA is completely converted to HEP, the second factor is the relative amount of HEP at the time t and the last factor is the ratio of the thermal offsets for the actual delay values and the delay values of the ^{13}C -Ref sequence. For the last correction, additional measurements were performed for all the delay values after complete conversion to HEP with the same acquisition parameters but 32 averages.

The temporal evolution of the reference measurements is shown in figure 3.5 on the facing page. Here, the protons of the double bond in the HEA molecule (ethylene group) occur around 6 ppm, while the protons of the methyl group of HEP are at 1.12 ppm and of the methylene group at 2.45 ppm. The reduction of the amount of HEA molecules in the solution is clearly visible and graphically shown by displaying the integral over the ethylene group protons in figure 3.5b. The antiphase signals of the hyperpolarized HEP at 1.12 ppm and 2.45 ppm are visible. However, the amplitudes of these peaks are only in the order of

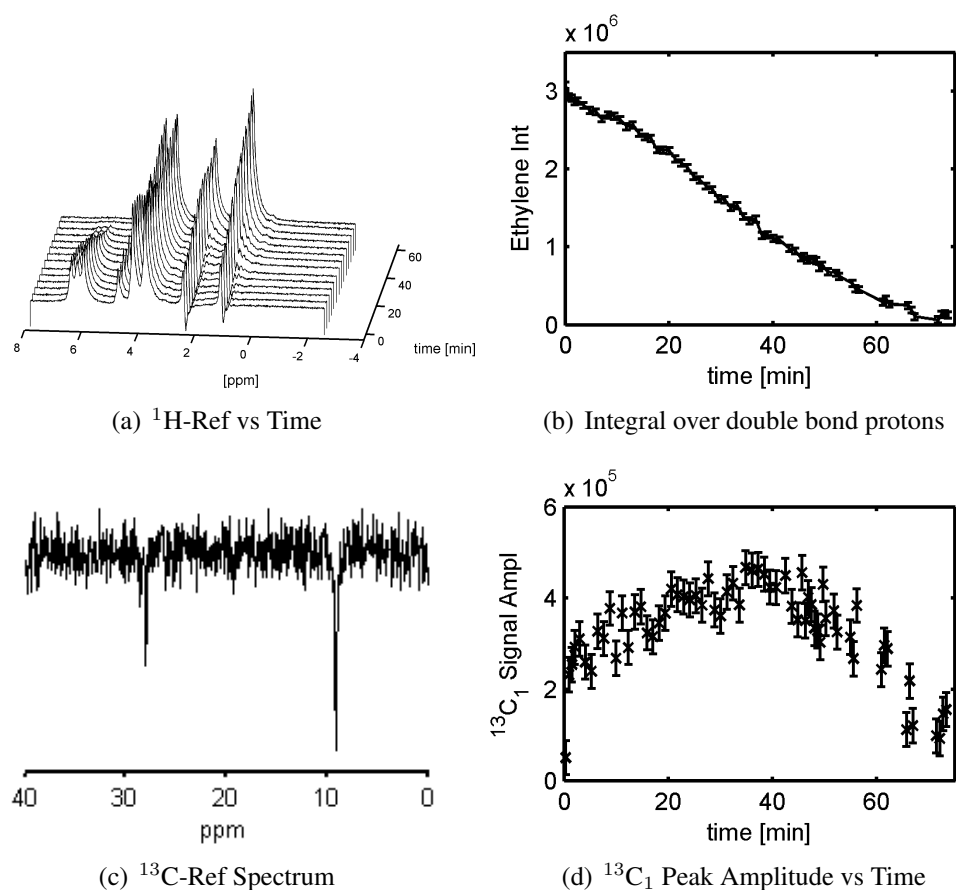


Figure 3.5: Temporal evolution of the reference measurements. In the ^1H -Ref spectra (a) the reaction of HEA to HEP is visible. The integral over the protons at the double bond in HEA (ethylene group) is shown. (c) shows a zoom of one ^{13}C -Ref spectrum with the $^{13}\text{C}_1$ peak at 9.2 ppm and the $^{13}\text{C}_2$ peak at 28.1 ppm. The temporal evolution of the $^{13}\text{C}_1$ peak amplitude is shown in (d).

the peaks originating from the thermally polarized protons. This is because a compromise had to be established between the signal enhancement and the possible duration of the experiment, being proportional to the number of τ delay values which can be measured during one experiment. It should be pointed out that the signal of the hyperpolarized protons only originates from the molecules which reacted during the repetition time period of 15 s. In comparison to the thermal signal of these amount of molecules, the signal enhancement was estimated to be around 300. The temporal evolution of the $^{13}\text{C}_1$ peak in the ^{13}C -Ref measurements is shown in 3.5d. In the beginning the signal increases rapidly after start of the parahydrogen inflow between the first two measurements. Then, it further slightly increases until around 40 min and finally decreases until HEA has completely reacted at 70 min. The remaining offset with a relative amplitude around 25% after the complete conversion stems from the thermally polarized molecule. This offset was corrected using equation 3.9 on the preceding page.

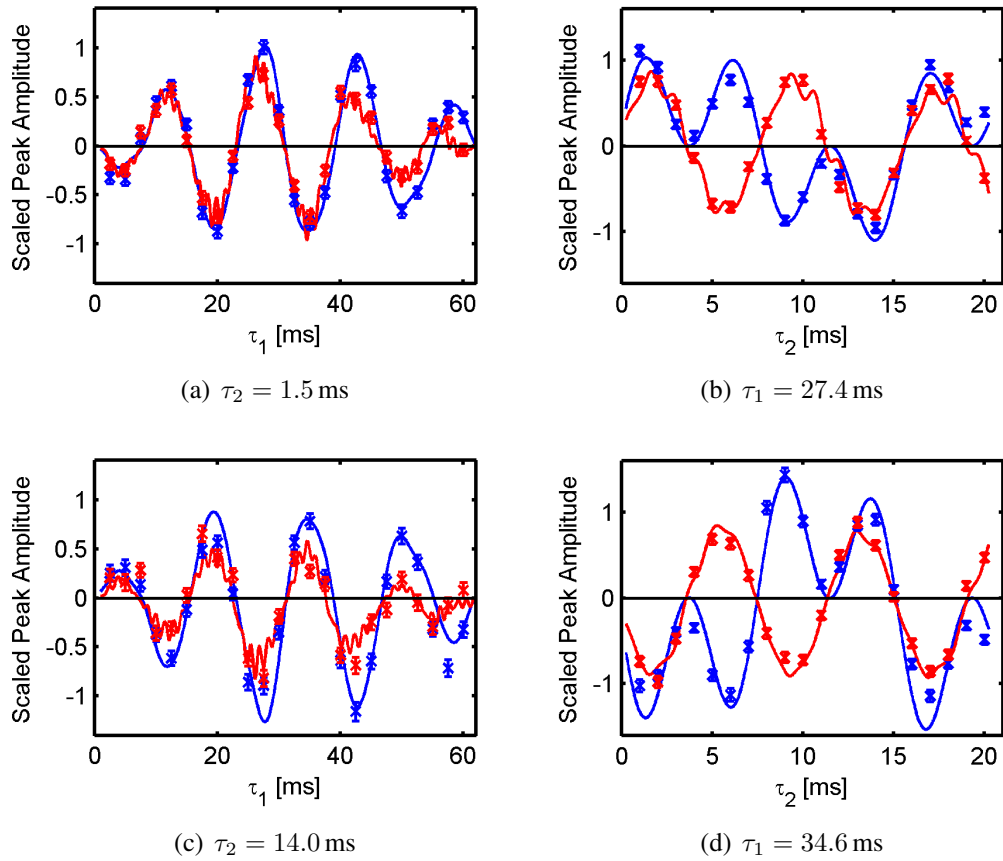


Figure 3.6: Comparison of experimental data with numerical simulations for the polarization transfer utilizing the PH-INEPT+ sequence. The variation of the τ_1 delay has been performed for (a) $\tau_2 = 1.5$ ms and (c) $\tau_2 = 14.0$ ms, the variation of the τ_2 delay for (b) $\tau_1 = 27.4$ ms and (d) $\tau_1 = 34.6$ ms. The data of $^{13}\text{C}_1$ -HEP is shown in blue, the data of $^{13}\text{C}_2$ -HEP in red. The error bars depict the measurement data and the lines correspond to the simulated curves.

The results of the τ variation experiments (Fig. 3.6) are in good agreement with the spin dynamics simulations. Even though there are certain deviations in the polarization transfer amplitude, the qualitative characteristics particularly the position of the optima are very well reproduced. Concretely, both main simulation results, the necessity of the longer τ_1 delay and the different τ_2 behavior of the two spin systems were validated.

3.2.2 Implementation on a Clinical MRI System

The PH-INEPT+ sequence requires the simultaneous RF transmission at both ^1H and ^{13}C frequencies. However, a conventional clinical MRI scanner is only equipped with a single RF transmit channel. Therefore, a sequential version of the PH-INEPT+ sequence was implemented (Fig. 3.7), in analogy to the sequential refocused INEPT sequence introduced by Klomp et al. [2008b]. In the sequential version, the original sequence was modified

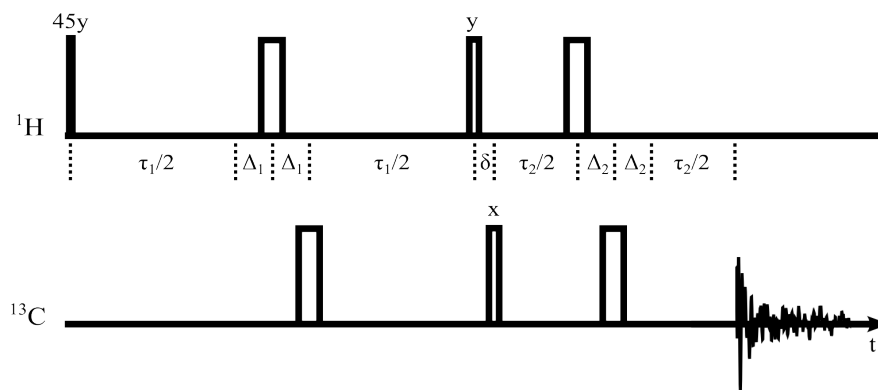


Figure 3.7: Sequential PH-INEPT+ sequence. Three delays Δ_1 , Δ_2 and δ were inserted to achieve a delay between the pulses. This time is needed to allow for RF frequency switching of the single transmit channel on a clinical MRI system.

by three delays Δ_1 , Δ_2 and δ to allow the single RF channel to switch the frequency. The delays Δ_1 and Δ_2 were added symmetrically around the first ^1H and the last ^{13}C 180° pulse. Additionally, the 90° pulses were shifted by δ . All delays were set to the minimum possible value, i. e. a delay of $100 \mu\text{s}$ between the pulses was needed by the hardware to switch the frequency.

The measurements were performed on a clinical 1.5 T MRI scanner (Magnetom, Sonata, Siemens) combined with an in-house manufactured double resonant $^1\text{H}/^{13}\text{C}$ coil optimized for NMR tubes with a diameter of 10 mm. 500 mg of the precursor molecule HEA without isotope labeling, 10 mg catalyst and 2.6 g D_2O were filled into an NMR pressure tube. The samples were heated to 70°C , pressurized with 4 bar of 93% enriched parahydrogen and vigorously shaken for 5 s inside the bore of the MRI scanner. In contrast to an NMR spectrometer, the shaking method can be performed under PASADENA conditions since the bigger magnet bore enables shaking at high magnetic field. After positioning the NMR tube inside the coil, a ^1H FID was acquired with a flip angle of 3° . This spectrum was used as a reference for the hyperpolarization. After a delay of 2 s the sequential PH-INEPT+ sequence was applied.

The τ_1 delay of the sequence was set to the optimum of 27.74 ms found in the simulations. Four different τ_2 delays were used (1.7 ms, 6.1 ms, 9.6 ms and 14 ms) at which for the first and the last delay the $^{13}\text{C}_1$ and the $^{13}\text{C}_2$ peaks are expected to be in phase (cf. Fig. 3.6b). The pulse duration was set to $200 \mu\text{s}$ for every pulse in the sequence. Eight measurements were performed for every τ_2 delay. Prior to the polarization transfer, initially hyperpolarized ^{13}C spin states were disturbed using a 90° pulse followed by a spoiling gradient.

For reasons of comparison, a ^{13}C FID was acquired 0.5 s after the ^1H FID instead of the polarization transfer sequence. This was performed both after shaking inside the magnetic

bore at 1.5 T and after shaking at earth field. A thermal spectrum of the sample was measured after it was completely hydrogenated to HEP. For this purpose 1024 scans were used (TR: 30 s, FA: 80°)

In figure 3.8 the ^{13}C NMR spectra acquired after the polarization transfer are shown. Due to the varying amount of initial ^1H hyperpolarization, the spectra were normalized each with their maximum signal intensity. They are of limited resolution as can be expected in a clinical MRI system. However, the position of the peaks in the multiplets from the dominant $J^1(^1\text{H}, ^{13}\text{C})$ couplings (cf. Fig. 3.8a) are reproducible. A special attention should be given to the two subpeaks of the $^{13}\text{C}_1\text{-HEP}$ and $^{13}\text{C}_2\text{-HEP}$ at around 20 ppm, since these peaks are very close. This might lead to a partial cancelation if they are in antiphase mode which is the case for $\tau_2 = 6.1$ ms and 9.6 ms. For 9.6 ms the peaks at 20 ppm are smaller than most of the peaks in the spectrum. However, this is not observed in the spectrum using $\tau_2 = 6.1$ ms.

In figure 3.9 on page 34 the spectra acquired without using the polarization transfer sequence are shown. Surprisingly, a hyperpolarized ^{13}C spin state was found also after shaking at 1.5 T. Moreover, the signal intensity of this spectrum was around a factor of 1.5 higher than the spectra after the polarization transfer. A discussion of this result can be found in section 3.4 on page 50. The thermal spectrum has a much lower signal to noise ratio even after 1024 scans. Here, the peaks and their multiplet structures are rarely visible. The background signal observed as a broad underlying peak ranging from 25 ppm to 50 ppm might stem e.g from glue used for the coil. The signal enhancement after polarization transfer in comparison to the thermal spectrum is approximately 120.

The signal available for imaging can be estimated by the integral of the absolute spectrum. These were calculated and normalized with respect to the signal of the ^1H reference. Mean values and standard deviations of the eight measurements per τ_2 value are shown in figure 3.10 on page 34. The integral over the spectrum directly acquired without polarization transfer is around 1.5 times higher as was found for the peak amplitudes. Within the margin of errors no difference was found for the polarization transfer using different τ_2 optima.

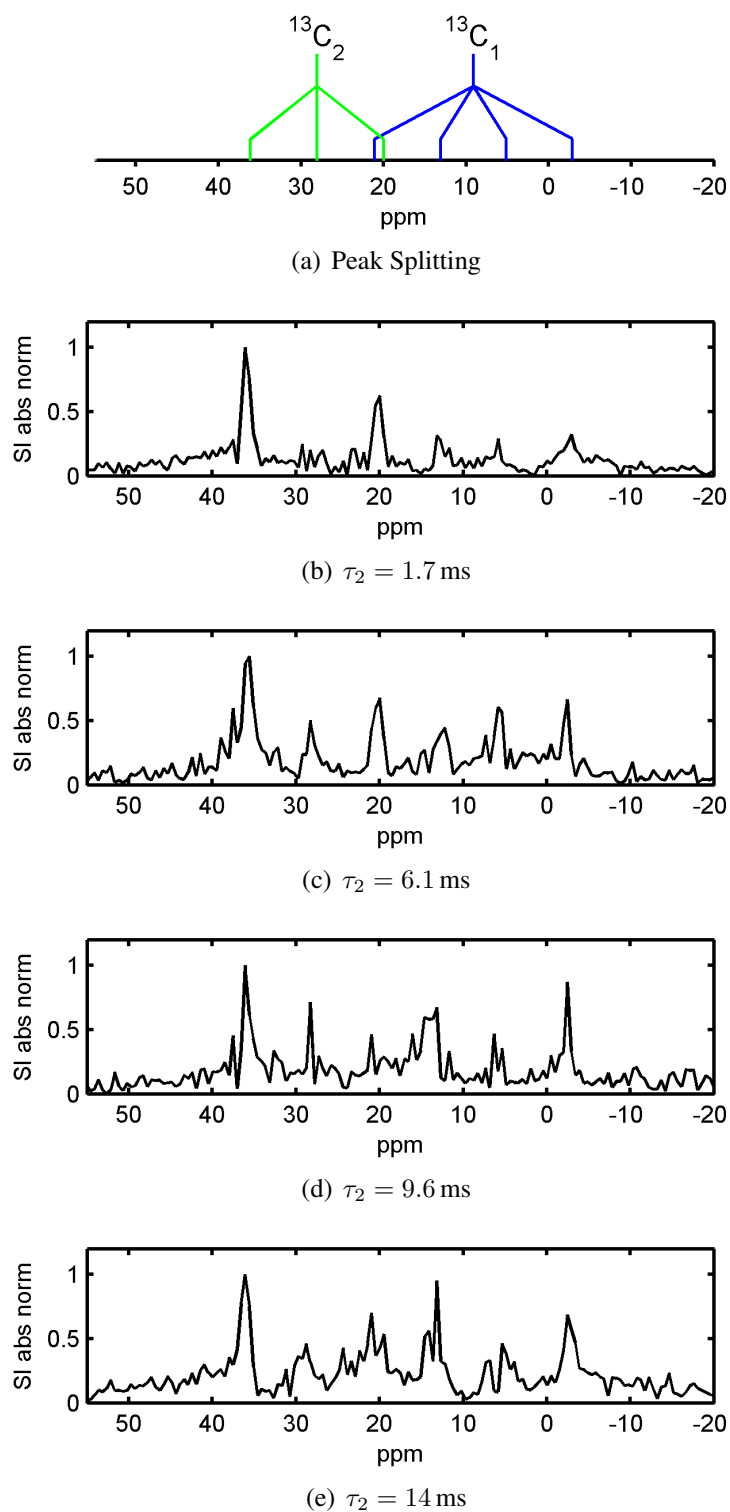


Figure 3.8: ^{13}C NMR spectra of HEP acquired after the sequential PH-INEPT+ sequence on a clinical MRI system using different τ_2 values. Absolute values are shown normalized each with the maximum signal intensity in the spectrum. τ_1 was set to 27.74 ms. At the top the splitting of the $^{13}\text{C}_1$ and the $^{13}\text{C}_2$ peaks caused by the $J^1(^1\text{H}, ^{13}\text{C})$ coupling is shown.

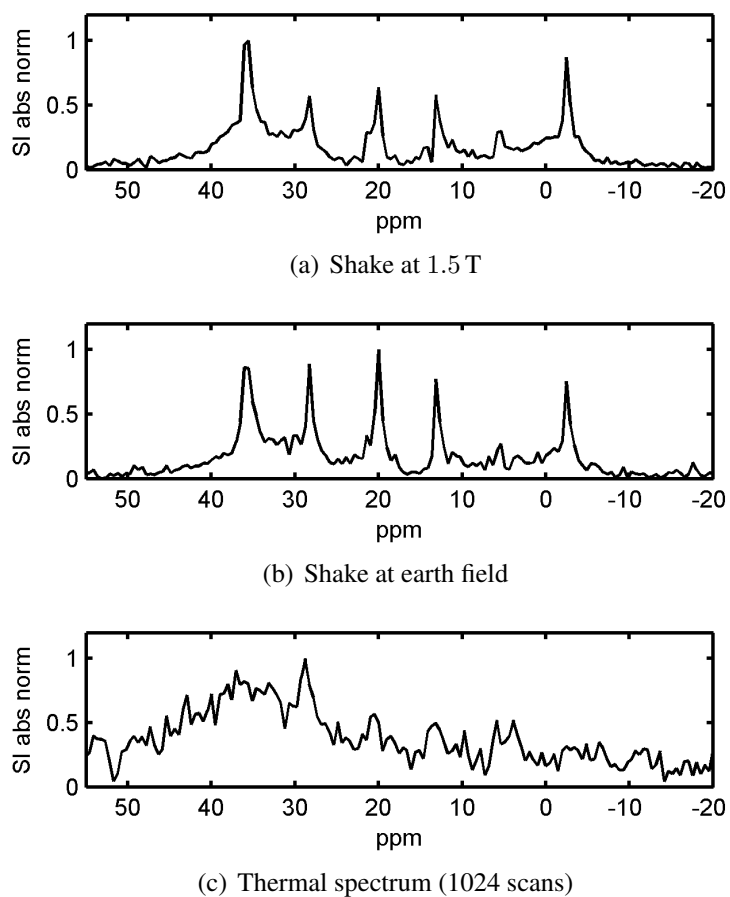


Figure 3.9: ^{13}C NMR spectra of HEP acquired with an FID measurement after the hydrogenation with pH_2 at (a) 1.5 T and (b) at earth field. For comparison a thermal spectrum is shown using 1024 scans. Absolute values are shown normalized each with the maximum signal intensity in the spectrum.

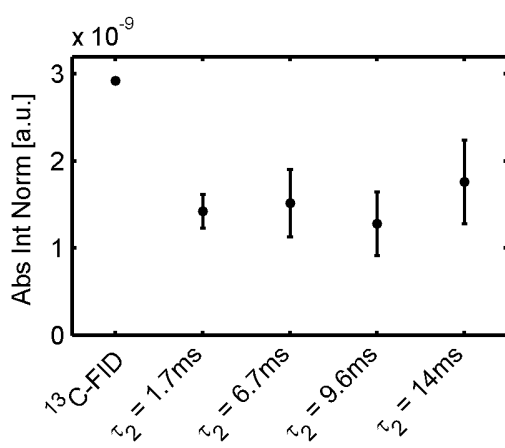


Figure 3.10: Integrals of the absolute spectrum for the ^{13}C FID and for the spectra acquired with the sequential PH-INEPT+ sequence using $\tau_1 = 27.74\text{ ms}$, normalized to the ^1H reference signal.

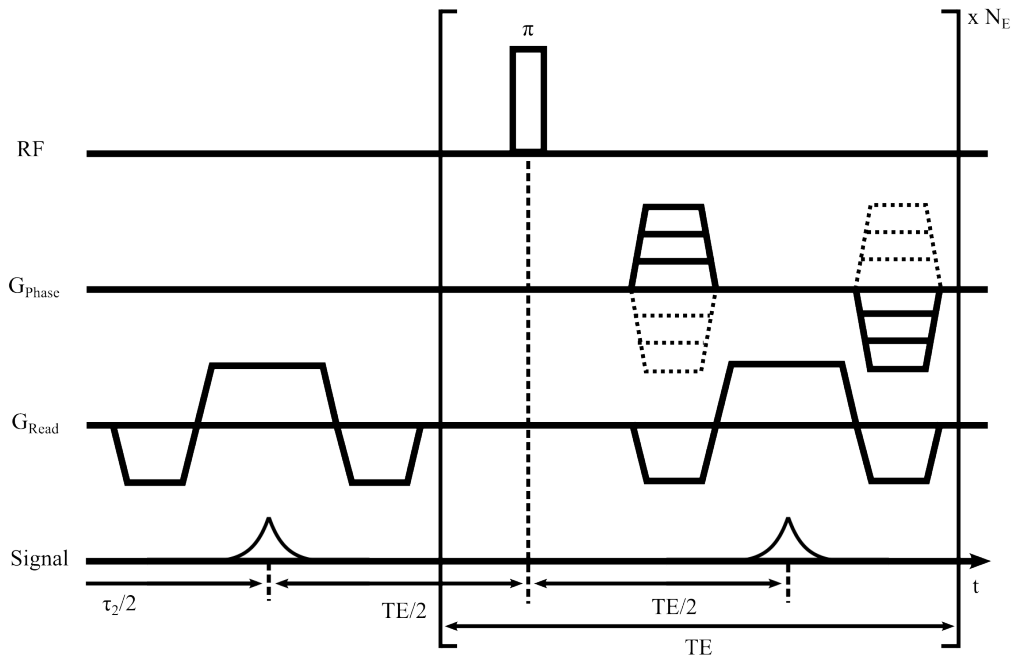


Figure 3.11: RARE sequence. The first echo evolving after the sequential PH-INEPT+ sequence was used for the first phase encoding step.

3.2.3 Combination with MR Imaging

Here, the hyperpolarized ^{13}C spin state was used for magnetic resonance imaging. For this purpose, the sequential PH-INEPT+ sequence (τ_1 : 27.74 ms, τ_2 : 14.0 ms) was combined with a fast spin echo sequence, which is also called RARE (rapid acquisition with refocused echoes). This spin-echo sequence consists of a train of 180° refocusing pulses and multiple echoes (cf. Fig. 3.11). The phase encoding gradient is changed for each echo and, as the readout gradient, refocused before the next pulse. The first echo refocusing after the sequential PH-INEPT+ sequence was used for the center k-space line of the first image.

The field of view (FOV) was set to 25x25 mm sampled by 8x8 pixels. The echo train was repeated 512 times to acquire 64 sequential images. A bandwidth of 800 Hz/pixel was used.

Signal Evolution in the Echo Train

Spin dynamics simulations have been performed to analyze the signal evolution during the echo train as a function of the echo time TE. The initial density operator was set to the ^{13}C spin operator S_x starting with the first echo after the PH-INEPT+ sequence. A projection of the density operator onto the raising operator S_+ was calculated at the center of every echo. The echo time TE was varied from 1.0 ms to 31.0 ms in steps of 0.05 ms at which 32 echoes were simulated for every TE value. The signal evolution was calculated for both the

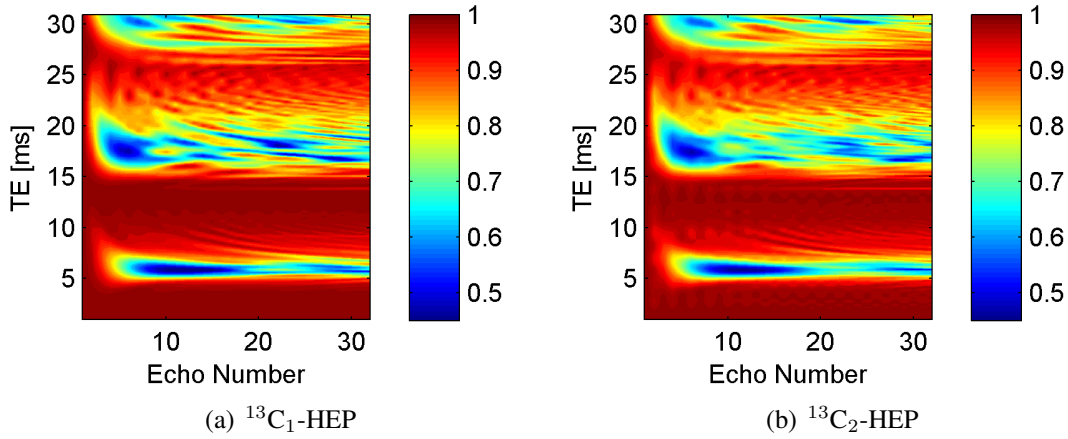


Figure 3.12: Simulation of the spin system evolution in the echo train for (a) $^{13}\text{C}_1$ -HEP and (b) $^{13}\text{C}_2$ -HEP using different echo times TE. The colormap depicts for the absolute value of the projection of the density operator on the ladder operator S_+ .

$^{13}\text{C}_1$ -HEP and the $^{13}\text{C}_2$ -HEP spin system (cf. Tab. 3.1).

The results of the simulations are shown in figure 3.12. No substantial differences are visible comparing the two spin systems. Nevertheless, the results show that there are TE regions where the signal is stable during the whole echo train (e.g. for $\text{TE} < 3.5$ ms or around $\text{TE} = 14$ ms). In between the signal decays rapidly within the first five echoes. In the TE range used for the simulations, this effect is most pronounced at TE around 5.9 ms and 18 ms. In figure 3.13 the mean echo amplitude of the two spin systems is shown for four echo times (7 ms, 14 ms, 18 ms and 26 ms), which were used later for the measurements. After the initial decay, the signal oscillates around 80% for $\text{TE} = 7$ ms and around 65% for $\text{TE} = 18$ ms.

To experimentally validate these simulation results, the RARE echo sequence was performed with the parameters described above but without any spatial encoding gradients. The mean absolute value of every echo was calculated. Due to the varying amount of hyperpolarization, each measurement was normalized with the value of the first echo, which is independent of the subsequent echo time TE.

The average of 5 measurements per echo time is shown in figure 3.14. The initial signal decay over the first echoes for $\text{TE} = 7$ ms and 18 ms is observed. In figure 3.14b the first 32 echoes are redrawn with the standard deviations of the five measurements. The experimental results are in good agreement with the simulation reproducing the signal loss as well as the oscillations of the signal. The global decay of the signal amplitudes is caused by the T_2 relaxation which was not taken into account in the simulations. As expected, this decay is more pronounced for longer TE values. Comparing the signal evolution for $\text{TE} = 7$ ms and 14 ms, the initial fast decay for $\text{TE} = 7$ ms is compensated by the smaller T_2 relaxation from around the hundredth echo.

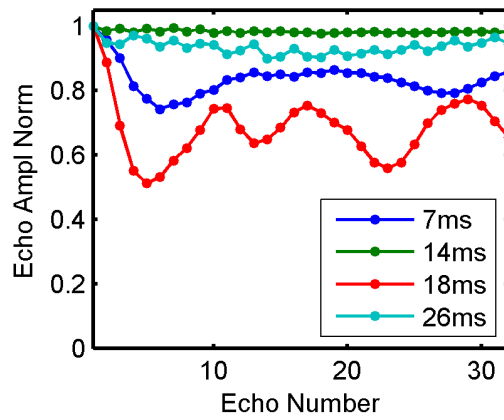


Figure 3.13: Simulation of the spin system evolution in the echo train for four different echo times TE. The echo amplitude was calculated by the mean value of the contributions from the $^{13}\text{C}_1$ and the $^{13}\text{C}_2$ spin system.

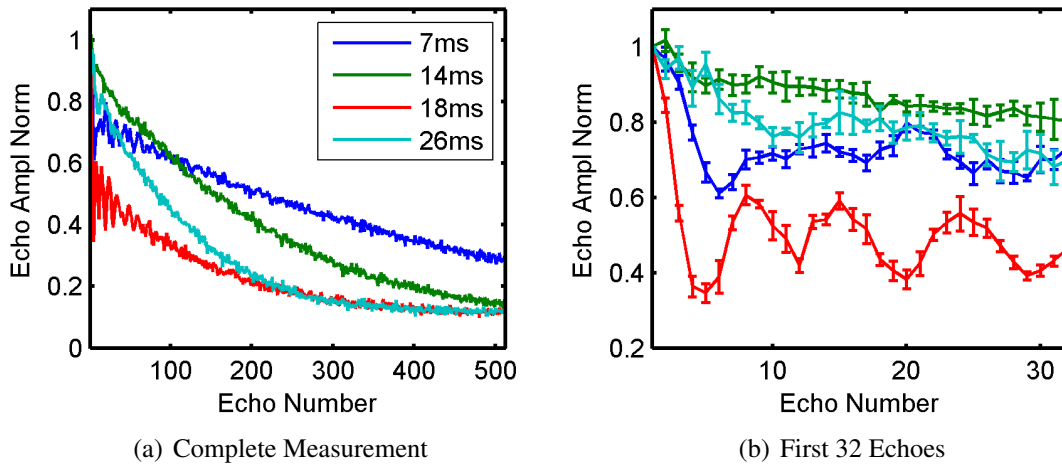


Figure 3.14: Measurement of the signal evolution in the echo train. The echo amplitude was calculated by the mean absolute value of the echo. The data was normalized with the first echo. In (b) the mean and the standard deviation of five acquisitions for the first 32 echoes are shown.

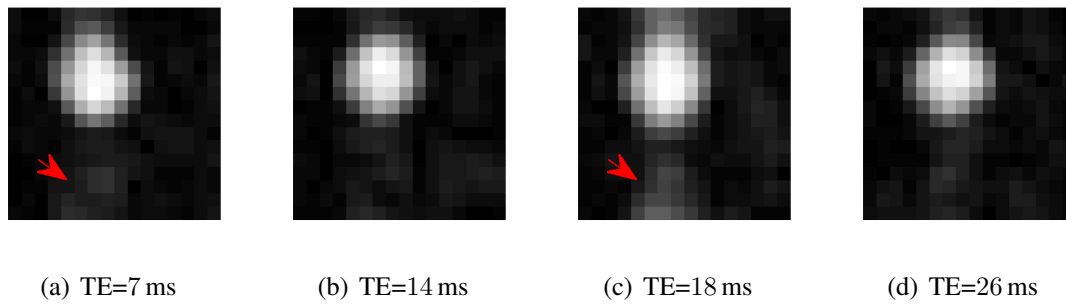


Figure 3.15: First ^{13}C projection images of the 10 mm NMR tube acquired in the echo train for (a) TE=7 ms, (b) 14 ms, (c) 18 ms and (d) 26 ms. The artifacts caused by the oscillations of the echo amplitude for 7 ms and 18 ms are marked by a red arrow.

Imaging

The imaging experiments were also performed for the four echo times used before (7 ms, 14 ms, 18 ms and 26 ms). To improve the representation of the images a factor 2 zero filling was used yielding 16x16 pixels.

In figure 3.15 the first images acquired with the used TE times are shown. For ^{13}C images, a good image quality was achieved with the hyperpolarized ^{13}C spin states. However, the fast signal decay and the oscillations causes image artifacts especially pronounced in the first image. For TE=18 ms strong artifacts are visible, one of which is indicated by a red arrow. This artifact is also visible but much less pronounced for TE=7 ms.

In figure 3.16 a complete image series is shown using TE=14 ms. The exponential decay caused by T_2 relaxation is clearly visible. However, even in the last image the object is slightly observable. The signal to noise ratio (SNR) in the first image is 13 (the noise was determined by the mean signal in the noise region at the right bottom of the image). By cumulative averaging in the echo train, the SNR could be increased up to 98.

To achieve the signal evolution with the images the mean signal inside the NMR tube was calculated. As before, the data were normalized with the mean signal of the first echo. Figure 3.17 on page 40 shows the average values of four measurements. The initial signal decay over the echoes is recovered in the images. For example, the mean signal of the second image for TE=7 ms, 18 ms and 26 ms is 83%, 57% and 85% relative to the mean signal for TE=14 ms. Comparing again the data of TE=7 ms and 14 ms, the initial signal decay is compensated by the lower T_2 relaxation from the 12. image on, which is in good agreement to the hundredth echo found before.

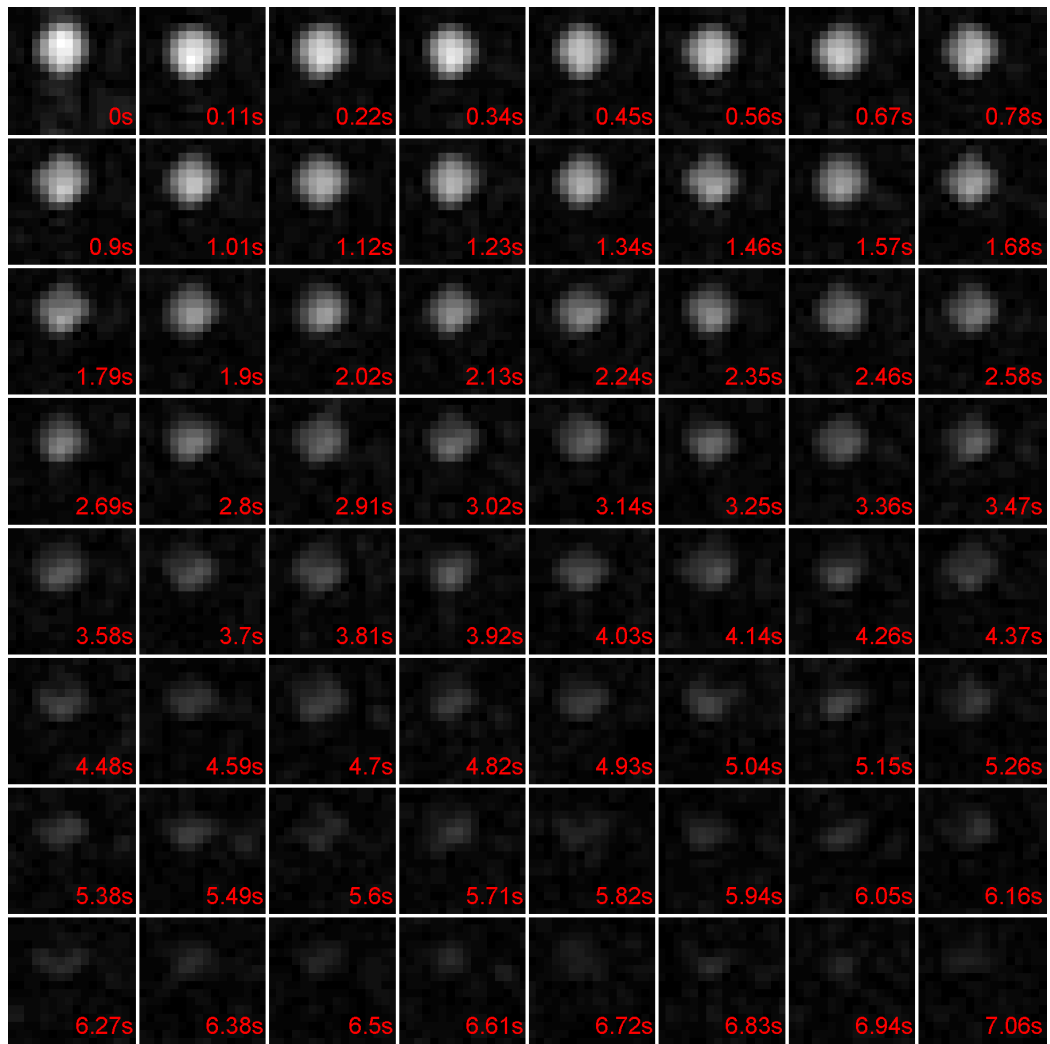


Figure 3.16: ^{13}C image series acquired in the echo train using $\text{TE}=14$ ms. The signal decay is caused by the transverse relaxation time T_2 . The acquisition time difference to the first image is shown on the bottom right of every image.

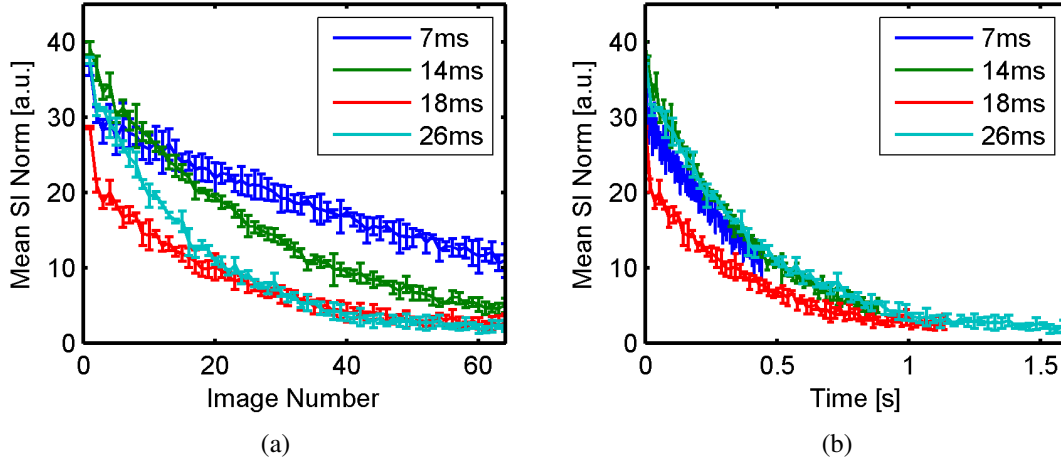


Figure 3.17: Signal evolution of the mean signal inside the NMR tube for four different echo times depending on (a) the image number and (b) the acquisition time.

3.3 Optimal Control

3.3.1 Theory

Optimal control (OC) theory is a mathematical optimization method mainly developed by Lev Pontryagin and Richard Bellman (e. g. [Pontryagin, 1962, Bellman, 1971]). Independent of the field of application, its task is to find an optimized path described by a set of differential equations which minimizes a certain cost function. This is a function of state and control variables.

The implementation of optimal control theory in NMR is a powerful tool to optimize a state-to-state transfer, i. e. a given initial density operator ρ_0 is transferred to a certain target operator C at time T . For this purpose, a sequence consisting of a train of N RF pulses is iteratively optimized. The spin density operator at the end of this pulse sequence is given by

$$\rho(T) = U_N(t_N, t_{N-1}) \dots U_2(t_2, t_1) U_1(t_1, 0) \rho(0) U_1^\dagger(t_1, 0) U_2^\dagger(t_2, t_1) \dots U_N^\dagger(t_N, t_{N-1}) \quad (3.11)$$

with the propagators defined as

$$U(t_{k+1}, t_k) = \hat{T} \exp \left(-i \int_{t_k}^{t_{k+1}} \mathcal{H}(t) dt \right), \quad (3.12)$$

with the Dyson time-ordering operator \hat{T} and the Hamiltonian \mathcal{H}

$$\mathcal{H}(t) = \mathcal{H}_{\text{int}} + \mathcal{H}_{\text{rf}}(t), \quad (3.13)$$

$$\mathcal{H}_{\text{rf}}(t) = \sum_i \omega_{\text{rf}}^{I_{ix}}(t) I_{ix} + \omega_{\text{rf}}^{I_{iy}}(t) I_{iy}, \quad (3.14)$$

$$\mathcal{H}_{\text{int}} = \mathcal{H}_{CS} + \mathcal{H}_J. \quad (3.15)$$

In the spin density operator at time T , written as $\rho(T) = c_{\text{max}}C + B$, the coefficient c_{max} is optimized and B contains all residual operator terms. The efficiency of the transfer, called the final cost Φ_{fin} , is calculated by the inner product of the target operator C and the transformed operator $\rho(T) = U\rho_0U^\dagger$:

$$\Phi_{\text{fin}} = \langle C | \rho(T) \rangle = \text{Tr}\{C^\dagger U\rho_0U^\dagger\}. \quad (3.16)$$

The correction gradients on the pulses between two iteration steps are calculated based on the inner products of the forward calculated state $\rho(t_i)$ starting from the initial state ρ_0 and the back-propagated state $\chi(t_j)$ starting from the target state C :

$$\frac{\partial \Phi_{\text{fin}}}{\partial \omega_{\text{rf}}^{I_{iq}}(t_j)} = \langle \chi(t_j) | -i\Delta t_j [I_{iq}, \rho(t_j)] \rangle. \quad (3.17)$$

This corresponds to an iterative update of the RF field by

$$\omega_{\text{rf}}^{I_{iq}}(t_j) \rightarrow \omega_{\text{rf}}^{I_{iq}}(t_j) + \epsilon \text{Tr}\{\chi^\dagger(t_j) i\Delta t_j [I_{iq}, \rho(t_j)]\}, \quad (3.18)$$

whereas ϵ is a small real number.

The iterative optimization process is schematically shown in figure 3.18. Additionally to the transfer efficiency, running costs can be accounted which are weighted with a small number λ . For example, the running cost of the overall consumption of radiofrequency (RF) energy is given by:

$$\Phi_{\text{rf}} = \lambda E_{\text{rf}}, \quad (3.19)$$

with the RF energy (in units of \hbar) defined as:

$$E_{\text{rf}} = \sum_i \sum_{q=x,y} \sum_{k=0}^{N-1} (\omega_{\text{rf}}^{I_{iq}}(t_k))^2 \Delta t_k. \quad (3.20)$$

The RF energy is an important parameter especially for *in vivo* applications since it is proportional to the specific absorption rate (SAR) [Bernstein et al., 2004]. The SAR is a measure of the absorption of RF electromagnetic fields in biological tissue. This absorption can cause unwanted heating of the patient and therefore should be kept under certain critical values.

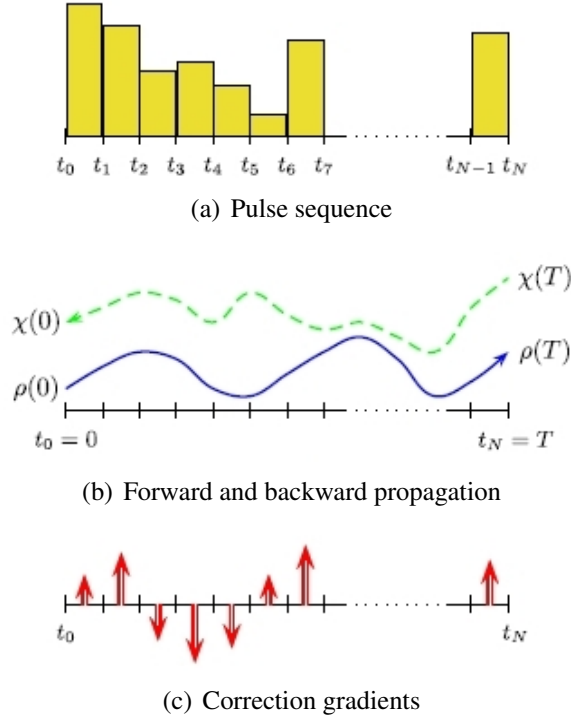


Figure 3.18: Schematic illustration of optimal control design of multiple-pulse experiments [Tosner et al., 2009].

The gradient for the iterative optimization of the RF energy is given by:

$$\frac{\partial \Phi_{\text{rf}}}{\partial \omega_{\text{rf}}^{I_{iq}}(t_j)} = 2\lambda \omega_{\text{rf}}^{I_{iq}}(t_j) \Delta t_j. \quad (3.21)$$

The total cost to be optimized is given by the subtraction of the running from the final cost:

$$\Phi_{\text{tot}} = \Phi_{\text{fin}} - \Phi_{\text{rf}}. \quad (3.22)$$

The higher the λ value the higher the contribution of the running cost to the total cost. If chosen too high this can constrain the optimization of the state-to-state transfer efficiency.

3.3.2 Optimization of Polarization Transfer using OC Theory

The implementation of optimal control in the software package SIMPSON [Tosner et al., 2009] was used to optimize the transfer from the initial PASADENA spin operator $I_{1z}I_{4z}$ of hydroxyethyl propionate (HEP) to the carbon-13 spin state S_z . The optimizations were performed for the $^{13}\text{C}_1$ -HEP spin system. Since a clinical MRI scanner is usually not equipped with a second radio frequency transmit channel, the optimizations were performed for a pulse sequence consisting of N isochronous pulses alternating between the proton and carbon-13 channel (Fig. 3.19). Every pulse consists of a train of n subpulses, whose ampli-

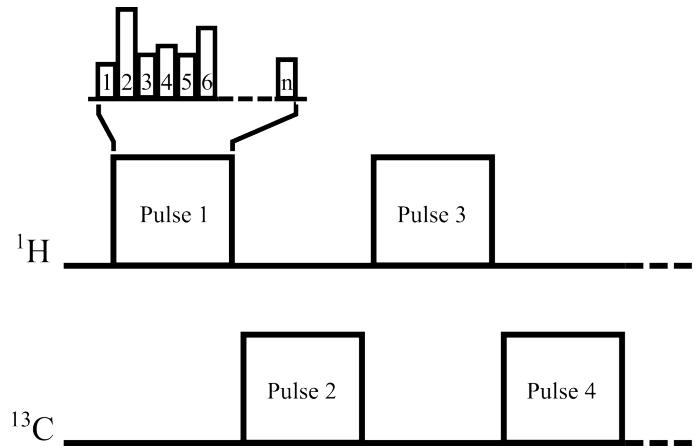


Figure 3.19: A combination of N isochronous pulses alternating between the proton and carbon-13 channel were used for the optimal control optimization. Each pulse consists of a train of n $10 \mu\text{s}$ subpulses varying in amplitude and phase.

tudes and phases are optimized. A sampling interval of $10 \mu\text{s}$ was used. Between the pulses, a delay of $100 \mu\text{s}$ was inserted, required by the hardware of the MRI scanner to switch the frequency of the transmit channel. The optimizations were performed for $N = 6$ and 8 pulses with a total duration of 14.9, 20.3, 25.7, 30.5 ms and 15.1, 19.9, 25.5, 30.3 ms, respectively. The optimization was done for a magnetic field of 7 T, since it was planned to validate the results on a 7 T spectrometer. For every combination of the parameters N , pulse duration and λ a minimum of 3 optimization procedures was performed starting the iterations in each case with randomly generated initial pulse sequences. The carrier frequency of the RF pulses on the proton channel was set between the methyl and the methylene group resonances, and for the carbon-13 channel on-resonant with the $^{13}\text{C}_1$ frequency.

Figure 3.20 shows the resulting OC pulse sequences which generate the maximum polarization transfer with a duration of 30.5 ms and $\lambda = 10^{-6}$ and $\lambda = 10^{-5}$, respectively. It is not possible to define a common pattern between these pulses because the solution is ambiguous, i. e. many different pulse sequences exist leading to same final transformation of the spin system.

The optimized pulses using the optimal control theory reach a transfer efficiency up to 11%. The results show no big differences whether a combination of 6 or 8 pulse sequences is used (Fig. 3.21). The results show that the transfer efficiency increases rapidly until a total sequence duration of approximately 25 ms. The increase is much smaller for the elongation from 25 ms to 30 ms. Therefore, no significant improvement is expected for pulse sequence durations longer than 30 ms, which have not been used due to the associated increase in computing time. The variation of λ from 10^{-7} to 10^{-5} yields only a small reduction of the transfer efficiency but a reduction of the RF energy by a factor of 35. In contrast, the increase of λ to 10^{-4} leads also to a reduction of the transfer efficiency

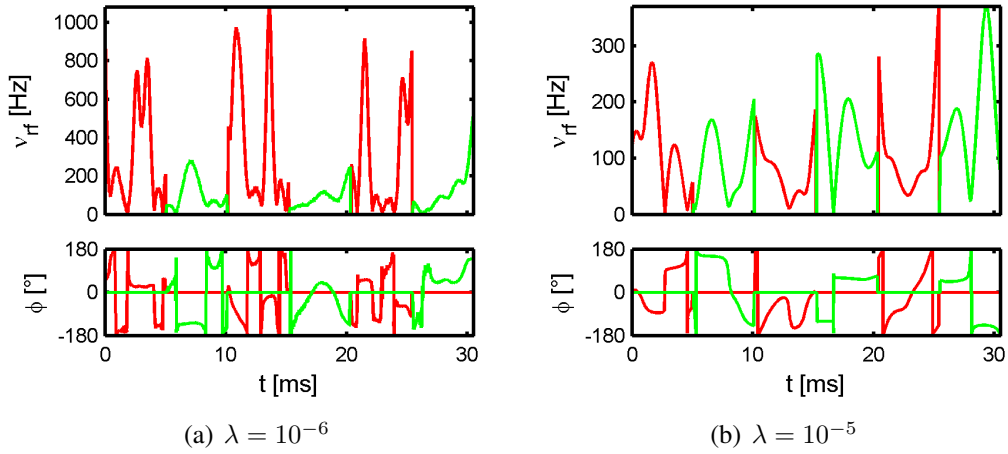


Figure 3.20: Optimized pulse sequences with a duration of 30.5 ms using 6 pulses and a weighting of the pulse energy of (a) $\lambda = 10^{-6}$ and (b) $\lambda = 10^{-5}$.

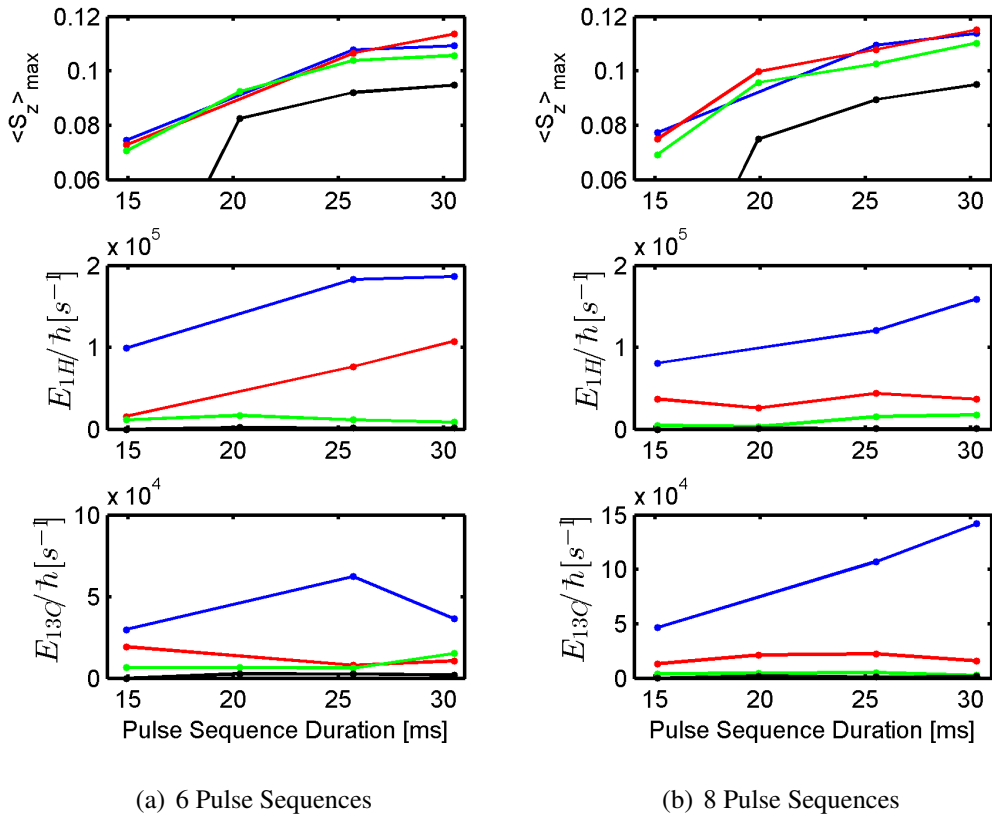


Figure 3.21: Transfer efficiencies and RF energies of the optimized pulse sequences using the optimal control theory with a combination of (a) 6 and (b) 8 pulse sequences. The colors depict for the λ value (blue: 10^{-7} , red: 10^{-6} , green: 10^{-5} , black: 10^{-4})

Table 3.2: Summary of transfer efficiencies and RF energies of the optimal control sequences and the sequential PH-INEPT+ sequence with an additional $(\frac{\pi}{2})_y$ pulse using a pulse duration of 200 μs .

		$\langle S_z \rangle_{\max}$	$E_{\text{rf},^1\text{H}}/\hbar [\text{s}^{-1}]$	$E_{\text{rf},^{13}\text{C}}/\hbar [\text{s}^{-1}]$
seq l-PH-INEPT+		0.05	114000	123000
Optimal control (6 pulses)	$\lambda = 10^{-7}$	0.11	311000	530000
	$\lambda = 10^{-6}$	0.11	108000	11000
	$\lambda = 10^{-5}$	0.11	8700	15000
	$\lambda = 10^{-4}$	0.09	1600	2100

by 9%. The results are summarized in table 3.2. They are compared to the sequential PH-INEPT+ sequence with an additional $(\frac{\pi}{2})_y$ pulse (seq l-PH-INEPT+). This sequence also generates longitudinal ^{13}C spin states. In comparison to the sequential l-PH-INEPT+ sequence, more than twice transfer efficiency can be achieved. Using an energy weighting factor of $\lambda = 10^{-6}$, the RF energy of the OC pulse sequence is already lower than the RF energy of the sequential l-PH-INEPT+ sequence with a constant pulse duration of 200 μs .

However, the results for the transfer efficiency have to be interpreted carefully. The calculated transfer efficiencies are only valid if the frequencies on both channels are exactly adjusted. Furthermore, the RF strength of the B_1 field needs to be exactly adjusted. In a realistic experiment, these conditions can only be fulfilled on average due to B_0 and B_1 field inhomogeneities. Therefore, simulations were performed to analyze the B_0 and B_1 field stability of the OC sequences. The B_0 field and frequency adjustment stability was analyzed by varying the RF pulse frequency by a delta frequency in the range from -1 to 1 ppm for the proton channel and -4 to 4 ppm for the carbon-13 channel. Additionally, the B_0 field was varied from 1 to 14 T keeping the RF pulse frequency onresonant. These variations were performed to test whether the OC pulse sequences could directly be transferred to other NMR systems with different B_0 field strengths, e. g. a 1.5 T MRI scanner. The B_1 field stability was tested by scaling the RF strength ν_{rf} by a factor between 0.5 and 1.5 . For comparison, these simulations were also performed for the sequential l-PH-INEPT+ sequence using a pulse duration of 200 μs .

The off-resonance stability tests (Fig. 3.22) show that the OC pulse sequence has only a very poor robustness. The transfer efficiency rapidly decreases with the carrier offset frequency showing a full width of half maximum (FWHM) of the center peak of only 0.19 ppm on the proton channel and 0.44 ppm on the carbon-13 channel for $\lambda = 10^{-6}$ ($\lambda = 10^{-5}$: ^1H 0.03 ppm, ^{13}C 1.31 ppm; $\lambda = 10^{-7}$: ^1H 0.13 ppm, ^{13}C 0.5 ppm). Moreover, there are regions with negative transfer which would lead to an additional reduction of the overall transfer efficiency since they cancel each other out with the main onresonance region. In comparison, in the simulated ppm region the seq l-PH-INEPT+ sequence shows only a small dependency on the off-resonance value. The variation of the magnetic field

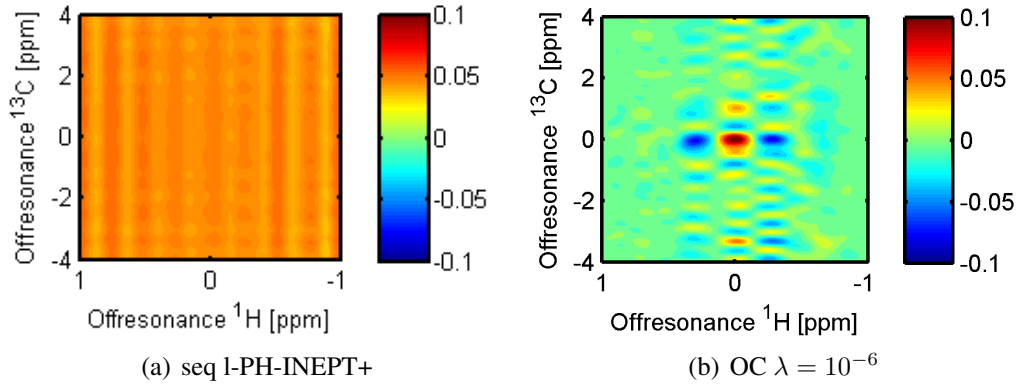


Figure 3.22: Off-resonance stability of the transfer efficiency using (a) the sequential l-PH-INEPT+ sequence and (b) the OC pulse sequence with 6 pulses and $\lambda = 10^{-6}$.

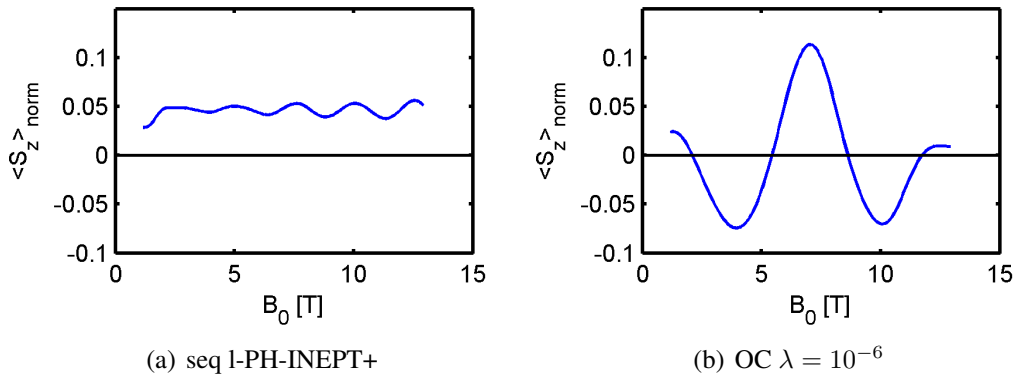


Figure 3.23: B_0 field stability of the transfer efficiency using (a) the sequential l-PH-INEPT+ sequence and (b) the OC pulse sequence with 6 pulses and $\lambda = 10^{-6}$.

strength B_0 also leads to a reduction of the polarization transfer of the OC sequence (Fig. 3.23). However, these results only show that the OC sequence should be optimized for the magnetic field of interest (in this case 7 T was used and corresponds to the maximum value). The magnetic field variation of a 7 T spectrometer does not significantly influence the polarization transfer. To achieve an optimized sequence e.g. at a magnetic field of 1.5 T new optimizations are necessary.

The B_1 stability tests (Fig. 3.24) show that the OC sequence has a reduced stability towards variation on the ^1H channel. The FWHM of the polarization transfer is only 18% for $\lambda = 10^{-6}$ whereas the seq l-PH-INEPT+ sequence has a FWHM of 56% ($\lambda = 10^{-5}$: 43%; $\lambda = 10^{-7}$: 26%). The B_1 stability on the carbon-13 channel is better. In the range of $\pm 50\%$ B_1 variation, the OC sequence has a higher polarization transfer than the seq l-PH-INEPT+ sequence ($\lambda = 10^{-5}$: 70%; $\lambda = 10^{-6}$: 75%; $\lambda = 10^{-5}$: 79%; seq l-PH-INEPT+: 71%).

The results obtained for the stability tests lead to the conclusion that stability optimiza-

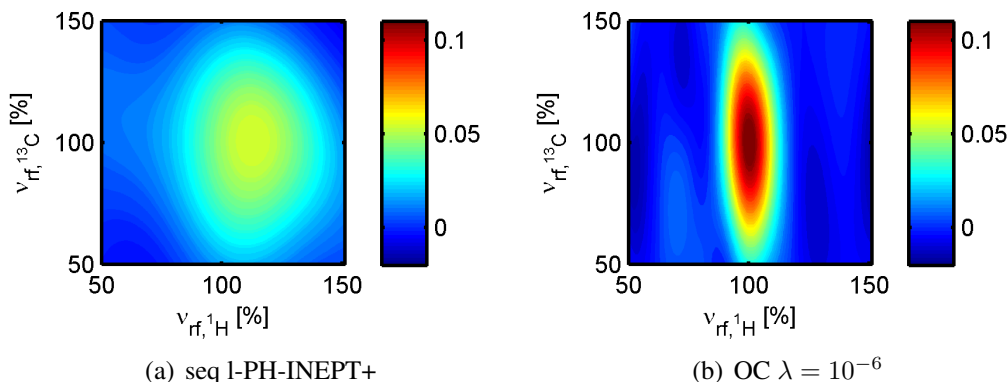


Figure 3.24: B_1 field stability of the transfer efficiency using (a) the sequential 1-PH-INEPT+ sequence and (b) the OC pulse sequence with 6 pulses and $\lambda = 10^{-6}$.

tion are necessary to achieve experimental practicability for the OC pulse sequences.

3.3.3 Off-resonance Stabilization

To optimize the RF offset stability of the OC pulses, the total cost and gradients in the optimization should be calculated based on several supporting points in a desired RF offset range [Tosner et al., 2009]. The RF offset stabilization was performed consecutively for the proton and the carbon-13 channel for the 6 pulse sequences with the maximum transfer efficiencies for $\lambda = 10^{-6}$. First, the ^1H RF pulses were optimized for a range of ± 0.5 ppm using 17 supporting points. The optimization was initiated with the pulse sequence for which the maximum transfer efficiency was achieved with the on-resonance optimizations. Subsequently, the ^{13}C RF pulses were optimized for a range of ± 2 ppm using 17 supporting points. The number of supporting points is limited by the increase in the computing time. The optimization of the pulses in the sequence took around two months on a single core of a 3.0 GHz processor.

The stability improvement of the OC pulse sequence is shown in figure 3.25. The FWHM could be increased to 1.1 ppm for the proton channel and 3.5 ppm for the carbon-13 channel. The maximum transfer efficiency at the center is slightly reduced from 0.11 to 0.10. The B_0 stability is also improved by the optimizations. At 3 T, the transfer efficiency is 86% of the maximum at 7 T. However, for 1.5 T still adapted optimizations are necessary (only 61% of the maximum transfer efficiency are achieved at 1.5 T). For $\lambda = 10^{-6}$, the B_1 stability is rather affected by the RF offset optimization. Moreover, a small increase of the B_1 stability was obtained (FWHM: ^1H : 28%, ^{13}C : 86%). The RF energy of the offset optimized pulse (in units of \hbar) is $113\,000\text{ s}^{-1}$ and $32\,100\text{ s}^{-1}$ for the ^1H and the ^{13}C channel, respectively (cf. Tab. 3.2 on page 45).

To simulate the net effect of the stability optimization the mean transfer efficiency was

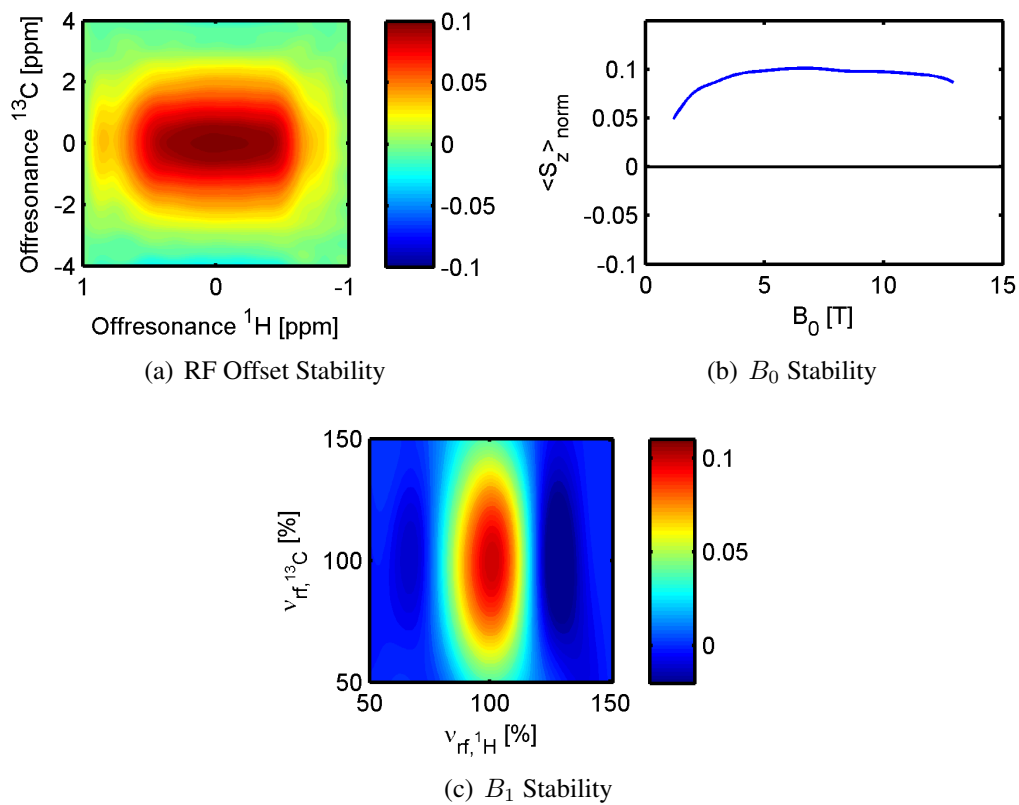


Figure 3.25: RF offset stabilization for the the OC pulse sequence with 6 pulses and $\lambda = 10^{-6}$.

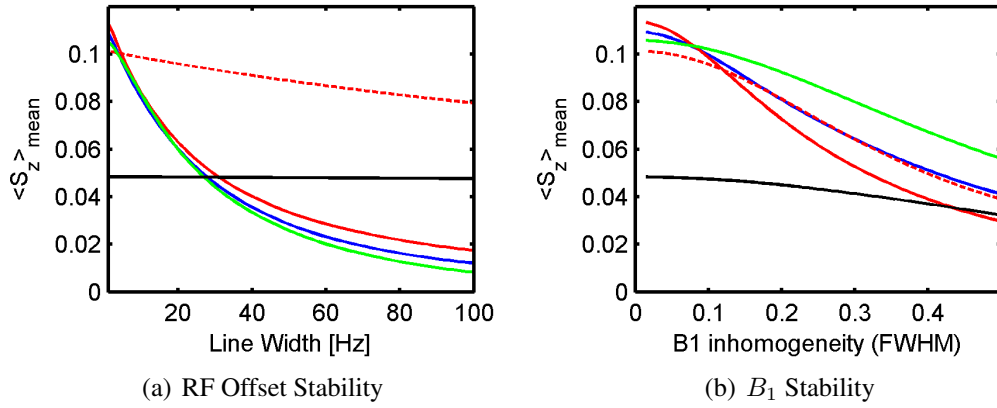


Figure 3.26: RF offset and B_1 inhomogeneity stability of the OC sequence using 6 pulses. Color depict for the λ values (blue: 10^{-7} , red: 10^{-6} , green: 10^{-5}), the dashed curve shows the results for the RF offset stabilized OC sequence. The black curve shows the stabilities of the PH-INEPT+ sequence.

calculated by summing over the weighted transfer efficiencies for different RF offset:

$$\langle S_z \rangle_{\text{mean}} = \sum_{\Delta\nu(^1\text{H}), \Delta\nu(^{13}\text{C})} w(\Delta\nu(^1\text{H}), \Delta\nu(^{13}\text{C})) \langle S_z \rangle_{\Delta\nu(^1\text{H}), \Delta\nu(^{13}\text{C})}, \quad (3.23)$$

whereas for the weighting function $w(\Delta\nu(^1\text{H}), \Delta\nu(^{13}\text{C}))$ the product of two Lorentzian functions was used. Since the line width depends mainly on the magnetic field inhomogeneity, the same line width (in ppm) was used for the two channels. The same calculations were performed for the B_1 inhomogeneity, but using the product of two Gaussian functions. For simplicity, the same relative B_1 width was used for the proton and the carbon-13 channel.

The stabilization optimizations clearly improve the RF offset stability as shown in figure 3.26a. The transfer efficiency of the onresonance optimized pulses decays faster with line width and does not show an improvement compared to the PH-INEPT+ sequence over a line width of approximately 30 Hz. The offset optimized pulse still shows a transfer efficiency of 80% of the maximum for a line width of 100 Hz. It should be noted that the benefit of the offset optimized pulse is even higher if, additionally, a deficient frequency adjustment is taken into account. The B_1 stability was not strongly influenced by the offset stabilization (Fig. 3.26b). The reduction of the transfer efficiency due to B_1 inhomogeneity is more remarkable for the optimized pulses than for the PH-INEPT+ sequence.

3.4 Discussion

3.4.1 Hollow-Fiber Membrane Modules

The hollow-fiber membrane modules are well-suited for pulse sequence optimizations. They were used in this thesis for the optimization of the sequence timing of the PH-INEPT+ sequence. One of the main advantages is the continuous generation of hyperpolarization under controllable conditions, like for instance, a dedicated magnetic field. The acquired data can robustly be corrected e. g. for the amount of hyperpolarization by taking reference measurements during the acquisition cycle. Therefore, a high agreement between the spin dynamics simulations and the measurements could be obtained.

However, the hollow-fiber membrane modules are limited in their lifetime. In measurements (not shown in this thesis) it was observed that the precursor molecule is hydrogenated by old membrane modules even in the absence of the catalyst. This is possibly caused by an accumulation of Rhodium on the fibers' surfaces, which leads to a heterogeneous catalysis. The heterogeneous catalysis is very inefficient in the simultaneous transfer of the two parahydrogen spins. Therefore, the amount of hyperpolarization is strongly reduced due to the competing effect of this unwanted reaction with the normal hydrogenation with the dissolved catalyst. The hollow-fiber membrane modules might be recyclable, e. g. by oxidative cleaning in a hydrochloric acid bath. The recyclability of the hollow-fiber membrane modules is not a restriction for *in vivo* applications since they would be used as disposable product for this purpose.

3.4.2 Hyperpolarized ^{13}C Spin State

Hyperpolarized ^{13}C signal was observed at 1.5 T without using a polarization transfer sequence. This effect was described before by Eisenschmid et al. [1989]. They observed an ^{31}P enhancement in the complex $\text{IrBr}(\text{CO})(\text{dppb})$ after hydrogenation with pH_2 . The physical process might be based on the nuclear Overhauser effect [Morris and Freeman, 1979, Solomon, 1955], which is explained in the following for a three spin system consisting of the two pH_2 protons and one ^{13}C spin. After the hydrogenation with pH_2 only the spin states $|\alpha\beta, \alpha\rangle$, $|\alpha\beta, \beta\rangle$, $|\beta\alpha, \alpha\rangle$ and $|\beta\alpha, \beta\rangle$ are populated (neglecting the Zeeman population). The double-quantum transition probability caused by the dipole-dipole coupling is strongly distance dependent ($\propto r^{-6}$). For example, in the $^{13}\text{C}_1$ -HEP molecule the protons in the methyl group have a distinct shorter distance to the ^{13}C than the protons in the methylene group. Therefore, the probability of the double-quantum transitions $|\alpha\beta, \alpha\rangle \rightarrow |\beta\beta, \beta\rangle$ and $|\beta\alpha, \beta\rangle \rightarrow |\alpha\alpha, \alpha\rangle$ is higher than for the transitions $|\alpha\beta, \beta\rangle \rightarrow |\alpha\alpha, \alpha\rangle$ and $|\beta\alpha, \alpha\rangle \rightarrow |\beta\beta, \beta\rangle$ (or vice versa). This causes a population difference of the spin states $|\alpha\beta, \alpha\rangle$ and $|\alpha\beta, \beta\rangle$ as well as $|\beta\alpha, \beta\rangle$ and $|\beta\alpha, \alpha\rangle$ which

leads to a signal enhancement in the ^{13}C spectra.

Since this effect is based on a relaxation process, it increases with the duration of the reaction and the subsequent delay until the acquisition is started. On the other hand, the signal enhancement by the polarization transfer sequence increases if these durations are shortened. We found that the NOE hyperpolarized ^{13}C spin state exceeded the signal enhancement of the polarization transfer by a factor of 1.5. However, it is supposed that the signal enhancement generated by the polarization transfer clearly exceeds the NOE signal enhancement by optimizing the reaction process and shortening the delay prior to the acquisition. Further discussions about these optimizations can be found below.

Future studies should proof the assumed origin of the observed ^{13}C signal enhancement. These studies have to be performed in a NMR spectrometer to achieve spectra of higher quality in comparison to the clinical system.

3.4.3 Polarization Transfer Sequence

Sequential Transmission

The principle of shifting RF pulses in a $^1\text{H}/^{13}\text{C}$ polarization transfer sequence has been proposed previously for thermal polarization [Watanabe et al., 1998, Klomp et al., 2008a,b]. They showed that the performance of the sequential versions practically equals the original sequences. In contrast to the sequence used in this study, they applied adiabatic pulses [Ugurbil et al., 1988] on the heteronucleus frequency. These pulses yield a higher B_1 field stability. However, the implementation of these pulses is more complicated and the stability requires pulse durations longer than 4 ms to fulfill the adiabatic condition. The improvement of the sequential PH-INEPT+ sequence by the use of adiabatic pulses should be addressed in a future study.

Signal Enhancement

The signal enhancement in the ^{13}C spectra after the polarization transfer of the PHIP spin state was estimated to be around 120 in this study. The signal enhancement is influenced by:

- Amount of parahydrogen
- Hydrogenation of the precursor molecule
- Elapsed time between the reaction and the polarization transfer
- Polarization transfer sequence

In this study, we used 93% enriched parahydrogen provided by a commercial Bruker BPHG90 Parahydrogen Generator operating at 37 K. Higher enrichment of parahydrogen

only moderately increase the maximal possible hyperpolarization (e. g. a factor of 1.1 by increasing the enrichment from 93% to 99%).

The sample used for the estimation of the signal enhancement was pressurized with $p\text{H}_2$ and shaken 25 times until the precursor HEA was completely hydrogenated to HEP. Using the ^1H reference, it was estimated that the amount of reaction per shake is less than 6.5%. In comparison, Hövener et al. [2009] achieved a complete reaction by using a reaction chamber in which the catalyst-precursor mixture is sprayed into a parahydrogen atmosphere. Increasing the amount of hydrogenated molecules from 6.5% to 100% would improve the signal enhancement by a factor of 15.

After shaking the sample, it was positioned inside the NMR coil which took around 1 s. Then the ^1H reference was acquired and 2 s later the polarization transfer sequence was started. The loss caused by the excitation pulse of the reference measurement (FA: 3°) is negligible since it causes only a reduction of the initial spin state by a factor of $\cos^2(3^\circ) \approx 0.997$. However, the delay caused by the reference acquisition is non-negligible due to longitudinal relaxation. Roth [2009] measured T_1 relaxation times in HEP of 5.8 s of the methyl group protons and 5.0 s for the methylene group protons at 7 T. These are most likely even shorter at 1.5 T. The loss of the initial spin state due to relaxation during 3 s is therefore estimated to be more than 50%. It directly follows that a cancellation of these delays would improve the signal enhancement by at least a factor of two.

The loss of polarization during the sequence is complex to determine, especially under the used reaction conditions. The sequence timing was accurately optimized using spin dynamics simulations which were experimentally validated. The spin dynamics simulations have the advantage over other theoretical calculations that they also take other factors such as the duration of the pulses into account. Recently, Bär et al. [2012] published a systematic analysis of the three $^1\text{H}/^{13}\text{C}$ polarization transfer sequences available for the PHIP spin state - the two low field sequences (spin order transfer (SOT) sequence by Goldman and Johannesson [2005] and the sequence by Kadlecik et al. [2010]) and the high field sequence l-PH-INEPT+ by Haake et al. [1996]. They found that the l-PH-INEPT+ sequence is more robust towards B_1 field and J-coupling errors. As mentioned above, further B_1 field improvements might be achieved by using adiabatic pulses.

Taking into account the possible mentioned improvements, i. e. the higher amount of reaction (x15) and the shortened delays (x2), the signal enhancement could be improved to 3600. In comparison, Hövener et al. [2009] achieved a polarization of 0.18 using an external polarizer with reaction chamber and NMR unit. Due to the transportation time of 33 s, the polarization is reduced to 0.09 inside the NMR scanner. At 1.5 T, this corresponds to a signal enhancement of 70,000. This huge difference cannot be ascribed to imperfections of the polarization transfer sequence. Hövener et al. [2009] used $1\text{-}^{13}\text{C}$ 2,3,3- D_3 -HEP whereas in my study no deuteration was performed. Without deuteration of HEP, the ini-

tial density operator $I_{1z}I_{4z}$ is equally distributed over $I_{1z}I_{4z}$, $I_{2z}I_{4z}$, $I_{3z}I_{4z}$, $I_{1z}I_{5z}$, $I_{1z}I_{5z}$ and $I_{1z}I_{5z}$ since the protons in the methyl group and the protons in the methylene group are magnetically equivalent. Therefore, the maximum transfer expected in the natural HEP is only approximately $\frac{1}{6}$ of the deuterated HEP. Hence, a signal enhancement of 21600 is expected for deuterated HEP with the sequential PH-INEPT+ sequence used in this study. The remaining deviation to the results by Hövener et al. [2009] by a factor of 3 to 6 might be caused by suboptimal robustness of the sequence towards hardware imperfections which should be improved in a future study.

3.4.4 Optimal Control

Polarization transfer optimizations were performed based on the optimal control theory yielding a promising improvement of the high-field polarization transfer by a factor of two. The experimental feasibility of these optimized sequences in the NMR scanner still needs to be demonstrated. Though, in general, this was shown in many studies before. Moreover, OC sequences were recently used by Bretschneider et al. [2012] for the PHIP spin state for the first time. In their report, they converted the longitudinal two-spin order of the initial PHIP spin state to evenly distributed single spin polarization of three protons.

Eventually, additional stabilizations will be necessary for the OC sequence shown in this thesis. This might include an extended RF offset range and a stabilization towards B_1 field inhomogeneities. However, the possible number of supporting points needed for these stabilizations is so far limited by the strongly increasing computing time. This is complicated by the fact that the implementation of the OC theory in the simulation package SIMPSON [Tosner et al., 2009] so far only runs on a single core of the processor. A parallelization of the calculations of the single supporting points is in principle possible since these calculations are independent of each other. Therefore, the implementation of the OC theory in SIMPSON would hugely benefit from the implementation of parallel processing.

3.4.5 Imaging

The hyperpolarized ^{13}C spin state was used for magnetic resonance imaging by utilizing a fast spin echo train.

The echo time behavior of the sequence was analyzed both by spin dynamics simulations and experimentally and a good agreement between these methods was found. An inadequate TE selection leads to a non-negligible initial signal loss. A shorter TE allows for detection of more echoes due to the lower transverse relaxation. However, in particular for ^{13}C imaging the gradients are a limiting factor for the possible resolution since they need to have a four times higher gradient moment in comparison to ^1H . Longer TE times

allow for longer gradients and therefore for higher spatial resolutions. The initial signal loss, the relaxation driven signal decay in the echo train and the desired spatial resolution should be taken into account to find the optimal echo time for a certain experiment.

The transversal magnetization generated by the sequential PH-INEPT+ sequence was directly used in the imaging experiments. For *in vivo* applications, the magnetization can be stored in longitudinal magnetization by using an additional 90° pulse (seq 1-PH-INEPT+) or even in a long-lived spin state by using special pulse sequences (c.f. chapter 4). This allows for injection and distribution of the hyperpolarized molecule before acquisition. The subsequent image acquisition can then directly be performed with the RARE sequence starting with a 90° pulse. The analysis of the echo time dependence made in this study is directly applicable to this modification since the system after a $(90^\circ)_y$ pulse starts in the S_x spin density operator as was used in the simulations.

3.4.6 ^{13}C Labeling / Deuteration

In this study, hydroxyethyl propionate was used in natural ^{13}C abundance and without deuteration. An adequate signal to noise ratio was achieved resulting in a good imaging quality. Therefore, ^{13}C labeling was not required for the performed *in vitro* experiments.

For *in vivo* experiments, both ^{13}C labeling and deuteration should be performed because of the dilution of the hyperpolarized molecules in the organism. The ^{13}C labeling directly enhances the signal by a factor of approximately 100. The deuteration has two advantages. First, this increases the longitudinal relaxation time of the ^{13}C spin state. Second, as stated above it increases the possible polarization transfer from the PHIP hyperpolarized ^1H spin state. The methods used in this study for optimization of the polarization transfer sequence timing and the echo time of the imaging sequence are applicable also for a three spin system. The careful selection of the echo time for the imaging experiment is also expected for these spin systems.

Chapter 4

Long-Lived Nuclear Spin States

Contents

4.1	Theory / Previous Work	56
4.2	Singlet Triplet Conversion	59
4.2.1	Field Cycling	59
4.2.2	RF Pulse Sequences	62
4.3	Multiple Conversion Experiment	68
4.3.1	Continuous Wave	71
4.3.2	Chemical Shift Scaling Sequence	74
4.4	Imaging	76
4.5	Discussion	79
4.5.1	Reference Measurement	79
4.5.2	Multiple Conversion Experiment	80
4.5.3	Singlet State Lifetime	80
4.5.4	RF Pulse Sequences	81
4.5.5	Imaging	83
4.5.6	Chemical Limitations	84
4.5.7	Comparison to Other Studies	84

This part of the PhD thesis addresses the transfer of a long-lived singlet state to the NMR observable triplet state using the Cs-symmetric molecule dimethyl maleate. This transfer can be realized by transporting the sample to a magnetic field strength B_{res} of 0.1 T (see section 4.1). The aim of the present work is to realize this singlet triplet conversion on a clinical 1.5 T MRI system not only by using the field cycling to the resonance magnetic field but also inside the magnet by using RF pulse sequences (section 4.2). In section 4.3 these converting RF pulse sequences are also used to generate multiple singlet triplet

conversions. The signal behavior in the multiple conversion train is analyzed and used to determine the singlet state lifetime and the conversion fraction of the sequence. In section 4.4 the multiple conversions are utilized for NMR imaging by combining them with field gradients. The results of this chapter are finally discussed in section 4.5.

4.1 Theory / Previous Work

A drawback of hyperpolarization in solution NMR experiments is the limited lifetime of the nuclear spin order since it is usually relaxing to the thermal equilibrium with the T_1 relaxation time (order of seconds). One approach to increase the lifetime is to transfer the polarization to a slower relaxing heteronucleus, e.g. ^{13}C , which was analyzed in the previous chapter. Another approach is to store the hyperpolarization in a nuclear spin singlet state. The singlet state's lifetime exceeds T_1 which is why it is called "long-lived spin state".

In homonuclear two-spin-1/2 systems, the singlet spin state with total nuclear spin angular momentum $I = 0$, as e.g. assumed by the parahydrogen molecule, is the long-lived state:

$$|S_0\rangle = \frac{1}{\sqrt{2}}(|\alpha\beta\rangle - |\beta\alpha\rangle). \quad (4.1)$$

The relaxation driven conversion of the singlet state to the three triplet states, with total nuclear spin momentum $I = 1$:

$$|T_{+1}\rangle = |\alpha\alpha\rangle, \quad (4.2)$$

$$|T_0\rangle = \frac{1}{\sqrt{2}}(|\alpha\beta\rangle + |\beta\alpha\rangle), \quad (4.3)$$

$$|T_{-1}\rangle = |\beta\beta\rangle, \quad (4.4)$$

is slower than the relaxation driven interconversion of the three triplet states. This is due to the fact that the modulation of the homonuclear intramolecular dipole-dipole interaction by random molecular tumbling, which is often the strongest relaxation mechanism in the NMR of liquids, is symmetric with respect to the exchange of the two nuclei and can not induce singlet triplet transitions [Pileio and Levitt, 2009].

The use of the singlet-state for long-term storage of nuclear spin order has the following difficulties: The singlet spin state can not be measured directly because its total nuclear spin is zero. Since it is antisymmetric with respect to the nuclear spin exchange it is a silent state for NMR. Therefore, it gives rise to no direct macroscopic observables since these are inherently symmetric. In the homonuclear spin-1/2-spin system with two magnetically equivalent spins (A_2 spin system), e.g. the parahydrogen molecule, the singlet spin state is an eigenstate of the spin evolution NMR Hamiltonian and therefore it will not evolve into a measurable triplet state. This problem is addressed by symmetry-breaking, which is for

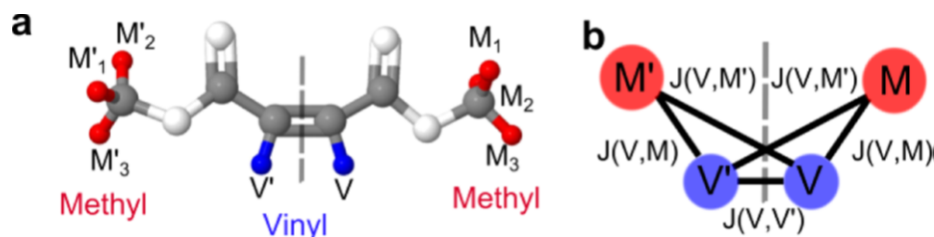


Figure 4.1: (a) Dimethyl maleate with labeled protons. (b) Sketch of the J-coupling network. Strong coupling $J_{V,V'} = 11.6$ Hz and remote coupling $J_{V,M}$ and $J_{V,M'}$ etc., are estimated to be lower than 1 Hz [Franzoni et al., 2012].

parahydrogen done by hydrogenating the two spins in a molecule where they have different chemical shifts. If the two spins have different chemical shifts (AX spin system), the singlet spin state is not an eigenstate of the spin Hamiltonian opening up for conversions from the singlet states to the measurable triplet states. However, this also reduces the lifetime of the singlet state, because due to the coherent conversion the singlet state relaxes with the fast triplet state relaxation time T_1 . To overcome this, the chemical shift difference needs to be suppressed until the measurement. This can be performed in two ways:

- moving to a sufficiently low external magnetic field
- applying a pulse sequence, which suppresses the chemical shift interaction in the sense of average Hamiltonian theory (AHT) [Haeberlen and Waugh, 1968].

The approach to reduce the chemical shift at low field to a negligible order has e.g. used by Carravetta et al. [2004], Carravetta and Levitt [2005], Canet et al. [2007]. Pulse sequences to minimize the evolution of the spin system due to chemical shift has been published among others by Carravetta and Levitt [2004] and Gopalakrishnan and Bodenhausen [2006].

Recently, it was shown that the singlet to triplet conversion can also be realized in a molecule where the PHIP protons have no chemical shift difference [Buljubasich et al., 2012, Franzoni et al., 2012]. This was shown for the Cs-symmetric molecule dimethyl maleate (DMM), which is obtained by hydrogenation of dimethyl acetylenedicarboxylate (DMAD). The molecule contains two methyl groups (M, M') and two vinyl protons (V, V') originating from the two parahydrogen protons (Fig. 4.1a). Since the three protons in each rotating methyl group are magnetically equivalent, the molecule can be simplified as two pairs of chemically equivalent spins 1/2 (Fig. 4.1b), which at high magnetic field represents an AA'XX' spin system. After the hydrogenation with pH₂ the vinyl protons are in the singlet state and therefore only the states $|S^{VV'}T_{+1}^{MM'}\rangle$, $|S^{VV'}T_0^{MM'}\rangle$, $|S^{VV'}T_{-1}^{MM'}\rangle$ and $|S^{VV'}S^{MM'}\rangle$ are populated, neglecting the Boltzmann contribution. The Hamiltonian's matrix expressed in the singlet-triplet basis shows potential nonzero off-diagonal terms connecting the singlet and triplet state of the vinyl protons:

$$\begin{aligned}
\langle T_{+1}^{VV'} S^{MM'} | \mathcal{H} | S^{VV'} T_{+1}^{MM'} \rangle &= \dots \\
\langle T_0^{VV'} S^{MM'} | \mathcal{H} | S^{VV'} T_0^{MM'} \rangle &= \dots \\
\langle T_{-1}^{VV'} S^{MM'} | \mathcal{H} | S^{VV'} T_{-1}^{MM'} \rangle &= \dots \\
-\langle T_{+1}^{VV'} T_{-1}^{MM'} | \mathcal{H} | S^{VV'} S^{MM'} \rangle &= \dots \\
\langle T_0^{VV'} T_0^{MM'} | \mathcal{H} | S^{VV'} S^{MM'} \rangle &= \dots \\
-\langle T_{-1}^{VV'} T_{+1}^{MM'} | \mathcal{H} | S^{VV'} S^{MM'} \rangle &= \pi(J_{V,M} - J_{V,M'})
\end{aligned} \tag{4.5}$$

This shows that the coherent singlet-triplet conversion in a Cs-symmetric molecule could be realized based on the symmetry break caused by the J-coupling network. If $J_{V,M} = J_{V,M'}$, the vinyl protons are magnetically equivalent and the initial state is an eigenstate of the Hamiltonian for every field strength. Therefore, $J_{V,M} \neq J_{V,M'}$ is a necessary condition. Investigating the magnetic field dependence of the energy level, Buljubasich et al. [2012] showed that under the condition $J_{V,M} \neq J_{V,M'}$ there are level anti-crossings among the energy levels of $| S^{VV'} T_{+1}^{MM'} \rangle$ and $| T_{+1}^{VV'} S^{MM'} \rangle$ at:

$$\Delta\nu_{V,M}^I = J_{V,V'} - J_{M,M'} \tag{4.6}$$

and of $| S^{VV'} S^{MM'} \rangle$ and $| T_{+1}^{VV'} T_{-1}^{MM'} \rangle$ at:

$$\Delta\nu_{V,M}^{II} = (J_{V,V'} + J_{M,M'}) - \frac{1}{2}(J_{V,M} + J_{V,M'}). \tag{4.7}$$

At this magnetic field strengths, the energy levels approach each other, but do not cross since they are coupled by the Hamiltonian. This yields a redistribution of the populations near the avoided crossing point. In the dimethyl maleate molecule, $J_{M,M'} \ll J_{V,V'}$ and therefore, $J_{M,M'}$ can be neglected in equation 4.6 and 4.7. Buljubasich et al. [2012] estimated $J_{V,M} \approx 0.75$ Hz and $J_{V,M'} \approx 0.25$ Hz because the couplings are long range. This yields $\Delta\nu_{V,M}^I \approx \Delta\nu_{V,M}^{II}$. The calculated resonance magnetic field strength for the singlet-triplet conversion in dimethyl maleate of $B_{\text{res}} = 0.1$ T was in perfect agreement with the experiments.

Franzoni et al. [2012] showed that in a magnetic field of 7 T, the singlet state of the vinyl protons in DMM has a life time $T_{\text{Singlet}} = 4$ min. They achieved this result by keeping the pH₂-hydrogenated DMM for a variable waiting time T_W at 7 T. Afterwards the sample was brought for a few seconds to 0.1 T to allow for singlet-triplet conversion and consecutively measured an FID at again 7 T. Repeating this transfer for several waiting times T_W yields an exponential decay of signal integral of the vinyl protons as a function of the waiting time T_W with the characteristic time T_{Singlet} .

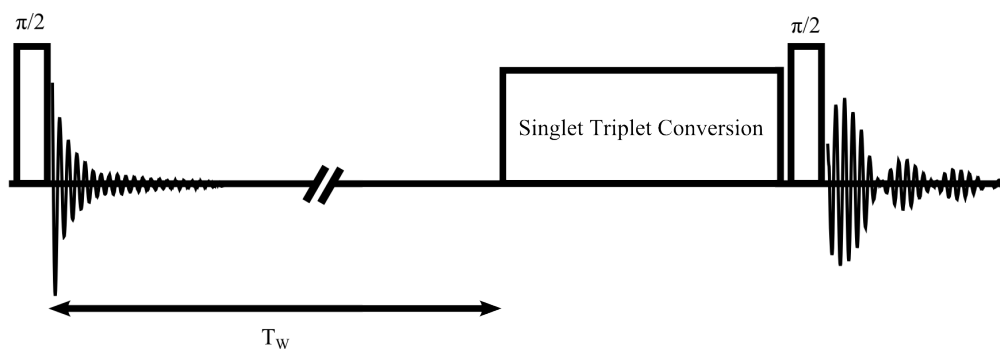


Figure 4.2: Measurement procedure. Directly after positioning the sample into the NMR coil a reference spectrum was measured. After a waiting time T_w the singlet triplet conversion was executed followed by an FID acquisition.

4.2 Singlet Triplet Conversion

The singlet triplet conversion was performed in a clinical 1.5 T NMR scanner, both by field cycling and RF pulse sequences. The samples used for the experiments consist of a mixture of 500 mg dimethyl acetylenedicarboxylate (99%, Sigma Aldrich) and 10 mg (0.23 mol%) of the hydrogenation catalyst [1,4-bis (diphenylphosphino) butane] (1,5-cyclo-octadiene) rhodium (I) tetrafluoroborate dissolved in 2.6 g of acetone- d_6 (99.9% D). They were prepared under Argon atmosphere and filled into 10 mm NMR pressure tubes sealed with a septum cap.

For both methods, the same procedure was used. At earth magnetic field the sample was heated up to 70 °C and pressurized with 4 bar of 93% enriched parahydrogen from an 1 L aluminum cylinder. Subsequently, the sample was rapidly transferred into the bore of the 1.5 T NMR scanner (Magnetom Sonata, Siemens), vigorously shaken for 5 s and positioned inside the NMR coil. An initial spectrum was acquired using a 90° excitation pulse. After a delay T_w , the singlet-triplet conversion was executed, either by the field cycling or by an RF pulse sequence, followed by another spectrum acquisition (Fig. 4.2).

4.2.1 Field Cycling

The accomplishment of the field cycling method to the resonance frequency at $B_{\text{res}} = 0.1$ T in a clinical 1.5 T NMR scanner has been performed mainly to proof the feasibility of the experiment in a clinical scanner with typical hardware imperfections like the reduced magnetic field shim. Furthermore, the determination of the singlet state lifetime T_{Singlet} at 1.5 T provides an estimation of the magnetic field dependency of the singlet state relaxation.

The position of the resonance magnetic field was determined with a gaussmeter on the center line of the patient table. The field cycling consists of a short transport time (< 1 s) of

the sample from the NMR coil to the resonance field position. The sample was positioned there for 5 s and subsequently fast repositioned in the NMR coil at 1.5 T. The measurement was performed for several waiting times T_W between 3 min and 20 min. One sample could be used for around 5 shakes until no more hyperpolarized signal is visible in the spectra.

In figure 4.3 the spectra for one experiment are shown using a waiting time of $T_W = 4$ min. In the reference spectrum (Fig. 4.3a) surprisingly a signal enhancement of the vinyl protons at around 6.5 ppm is visible. In contrast to the hyperpolarized signal after the singlet-triplet conversion this peak is in phase to the methyl group peak at around 4 ppm. This peak does not stem from the thermal equilibrium because after six shakes, the net conversion by the catalyst of dimethyl acetylenedicarboxylat to dimethyl maleate is so low, that even in the final thermal spectrum the vinyl group is not visible as can be seen in the thermal spectrum (Fig. 4.3c). The hyperpolarization directly after the shake is unexpected, since the shake and therefore the reaction is performed at 1.5 T being far away from the singlet-triplet resonance at 0.1 T. However, the NMR tubes are pressurized with parahydrogen at earth field. Therefore, it is assumed that the hyperpolarization stems from the small amount of hydrogenated molecules generated in the short duration between pressurizing and crossing of the resonance field. This conjecture is supported by the fact that the methyl group peak in the reference measurement is smaller in comparison to the thermal measurement, i.e. the hyperpolarization signal also have an antiphase contribution on the methyl group which is not big enough to flip the peak. Therefore, the vinyl and methyl peaks show the same characteristics in the reference measurements as in the spectra after the executed singlet triplet conversion, which yield to the assumption that they are based on the same physical effect.

The spectrum after the singlet triplet conversion is shown in figure 4.3b. The spectrum consists of the vinyl group and the methyl group peak being in anti-phasic position towards each other. Moreover, the hyperpolarized methyl peak shows also a 180° phase shift in comparison to the peak originating from the thermal polarization. This is consistent to the experiments and simulations performed at 7 T by Buljubasich et al. [2012].

The amount of hyperpolarized molecules depends on the amount of molecules being converted by the catalyst during the reaction period. This amount strongly varies between two shakes. This is the main reason for the dispersion observed in the data. Therefore, a normalization of the vinyl peak integral after the singlet-triplet conversion is necessary. Since the activity of the catalyst mainly influences the amount of hydrogenated molecules, it was assumed that vinyl peak in the reference spectrum is proportional to the amount of hydrogenated molecules in the reaction period. Therefore, it was used for the normalization. The decay of the normalized vinyl group integral with the waiting time T_W is shown in figure 4.4. The exponential fit of these data points yields a lifetime of the long-lived state of (4.0 ± 1.2) min at 1.5 T.

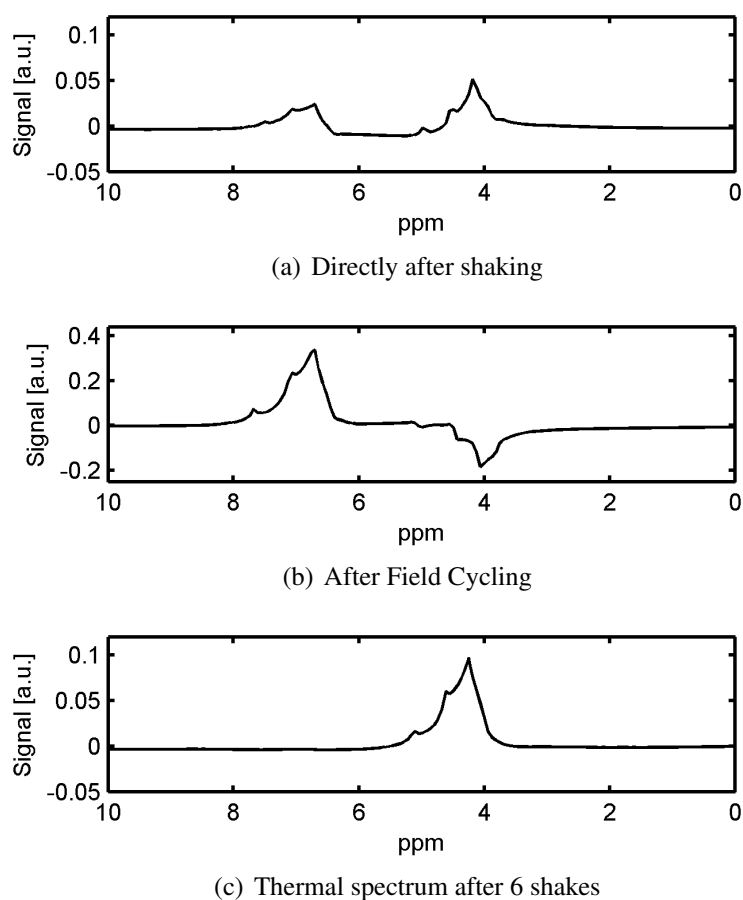


Figure 4.3: ^1H NMR spectra of (a) the reference measurement directly after shaking and (b) the measurement after the field cycling executed after a waiting time of $T_W = 4$ min. (c) Thermal spectrum after the sixth shake.

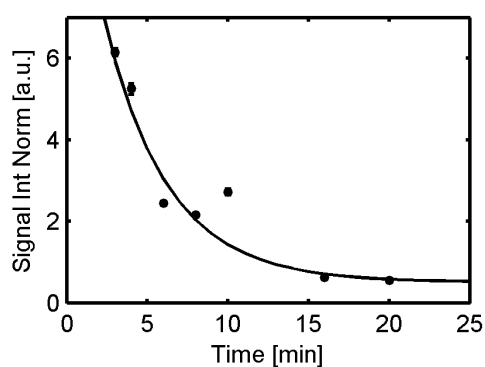


Figure 4.4: Decay of the long-lived state at 1.5 T. The integral over the vinyl group peak was normalized with the integral of the reference measurement. Exponential fit function with a characteristic time $T_{\text{Singlet}} = 4.0 \pm 1.2$ min.

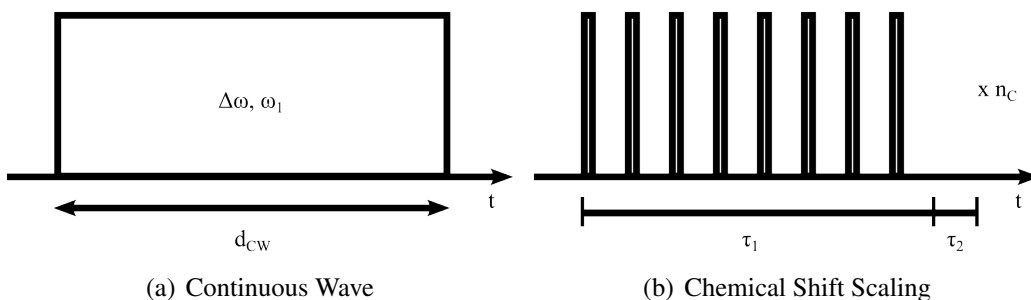


Figure 4.5: RF pulse sequences to execute the singlet triplet conversion inside the NMR scanner.

4.2.2 RF Pulse Sequences

Two known pulse sequences (Fig. 4.5) were adapted and optimized to allow the singlet triplet conversion inside the NMR magnetic field of 1.5 T:

- Continuous Wave - constant RF excitation with frequency ω_{RF} , RF strength ω_1 and duration d_{CW}
- Chemical Shift Scaling Sequence - a sequence consisting of π pulses and two characteristic durations to scale or even average out the chemical shift [Morris et al., 2003]

Continuous Wave

The application of an unmodulated RF field - for historical reasons called "continuous wave" - was used before to cancel out the chemical shift difference in nonequivalent and nearly-equivalent molecules to prevent the singlet state from mixing with the triplet state at high fields [Carravetta and Levitt, 2004, Sarkar et al., 2007, Pileio and Levitt, 2009] and therefore increase its lifetime. The idea behind the use of a continuous wave (CW) for the Cs-symmetric molecule dimethyl maleate is not to prevent but to allow for the singlet-triplet conversion by reducing the chemical shift difference of the vinyl and the methyl group to the same difference they have at the resonance field of 0.1 T.

The Hamiltonian of the unperturbed 4 spin system of the Cs-symmetrical molecule in the rotating frame is given by:

$$\mathcal{H} = \Omega_V(I_V^z + I_{V'}^z) + \Omega_M(I_M^z + I_{M'}^z) + J\text{-terms}, \quad (4.8)$$

in which $\Omega_K = \omega_K - \omega_{\text{ref}}$ ($K = V$ or M , V : Vinyl, M : Methyl) with ω_{ref} being the rotation frequency of the rotating frame. The J-coupling terms are invariant operators under the RF modulation and therefore will be excluded in the following calculations.

Using $I_{\mathbf{K}\mathbf{K}'}^j = I_{\mathbf{K}}^j + I_{\mathbf{K}'}^j$ ($\forall j \in \{x, y, z\}, \forall \mathbf{K} \in \{\mathbf{V}, \mathbf{M}\}$) and introducing $\Delta\omega = \frac{1}{2}(\Omega_{\mathbf{V}} + \Omega_{\mathbf{M}})$ and $\Delta\Omega = \frac{1}{2}(\Omega_{\mathbf{V}} - \Omega_{\mathbf{M}})$, the Hamiltonian can be rewritten as:

$$\mathcal{H} = \Delta\omega(I_{\mathbf{V}\mathbf{V}'}^z + I_{\mathbf{M}\mathbf{M}'}^z) + \Delta\Omega(I_{\mathbf{V}\mathbf{V}'}^z - I_{\mathbf{M}\mathbf{M}'}^z). \quad (4.9)$$

The singlet triplet conversion is caused by the antisymmetric term $\Delta\Omega(I_{\mathbf{V}\mathbf{V}'}^z - I_{\mathbf{M}\mathbf{M}'}^z)$, in which $\Delta\Omega$ is independent of the chosen ω_{ref} . Under the perturbation of the system by an RF pulse, the Hamiltonian takes the form:

$$\mathcal{H} = \omega_1(I_{\mathbf{V}}^x + I_{\mathbf{V}'}^x + I_{\mathbf{M}}^x + I_{\mathbf{M}'}^x) + \Omega_{\mathbf{V}}(I_{\mathbf{V}}^z + I_{\mathbf{V}'}^z) + \Omega_{\mathbf{M}}(I_{\mathbf{M}}^z + I_{\mathbf{M}'}^z), \quad (4.10)$$

in which ω_1 is the RF strength of the CW pulse and the reference frequency was set to the carrier RF frequency: $\omega_{\text{ref}} = \omega_{\text{RF}}$. The phase ϕ_{RF} of the pulse is set to zero, since it has no influence on the further considerations. This Hamiltonian can again be rewritten as:

$$\mathcal{H} = \omega_1(I_{\mathbf{V}\mathbf{V}'}^x + I_{\mathbf{M}\mathbf{M}'}^x) + \Delta\omega(I_{\mathbf{V}\mathbf{V}'}^z + I_{\mathbf{M}\mathbf{M}'}^z) + \Delta\Omega(I_{\mathbf{V}\mathbf{V}'}^z - I_{\mathbf{M}\mathbf{M}'}^z). \quad (4.11)$$

This system can be transformed into another rotating frame, rotating around the effective rotation axis, given by:

$$\vec{\omega}_{\text{eff}} = \omega_{\text{eff}}(\sin(\theta)\mathbf{e}_x + \cos(\theta)\mathbf{e}_z), \quad (4.12)$$

with $\omega_{\text{eff}} = \sqrt{\omega_1^2 + \Delta\omega^2}$ and $\tan(\theta) = \frac{\omega_1}{\Delta\omega}$, which yields:

$$\tilde{\mathcal{H}} = \omega_{\text{eff}}(I_{\mathbf{V}\mathbf{V}'}^z + I_{\mathbf{M}\mathbf{M}'}^z) + \cos(\theta)\Delta\Omega(I_{\mathbf{V}\mathbf{V}'}^z - I_{\mathbf{M}\mathbf{M}'}^z) - \sin(\theta)\Delta\Omega(I_{\mathbf{V}\mathbf{V}'}^x - I_{\mathbf{M}\mathbf{M}'}^x). \quad (4.13)$$

The third term on the right side of equation 4.13 has only nonsecular contributions and can therefore be neglected in the secular approximation. Comparing equations 4.9 and 4.13, one finds that the CW pulse yields the possibility to scale the antisymmetric term in the Hamiltonian. To achieve the singlet triplet conversion by the CW pulse, the following condition needs to be fulfilled:

$$\cos(\theta_{\text{res}})\Delta\Omega \Big|_{B_0} = \Delta\Omega \Big|_{B_{\text{res}}}, \quad (4.14)$$

where in our case the magnetic field $B_0 = 1.5$ T and the resonance field $B_{\text{res}} = 0.1$ T. It directly follows, that:

$$\theta_{\text{res}} = \arccos\left(\frac{B_{\text{res}}}{B_0}\right). \quad (4.15)$$

In practice, this condition can be fulfilled by choosing an appropriate relation of the RF pulse strength ω_1 and the RF offset $\Delta\omega$ from the center frequency between the methyl and

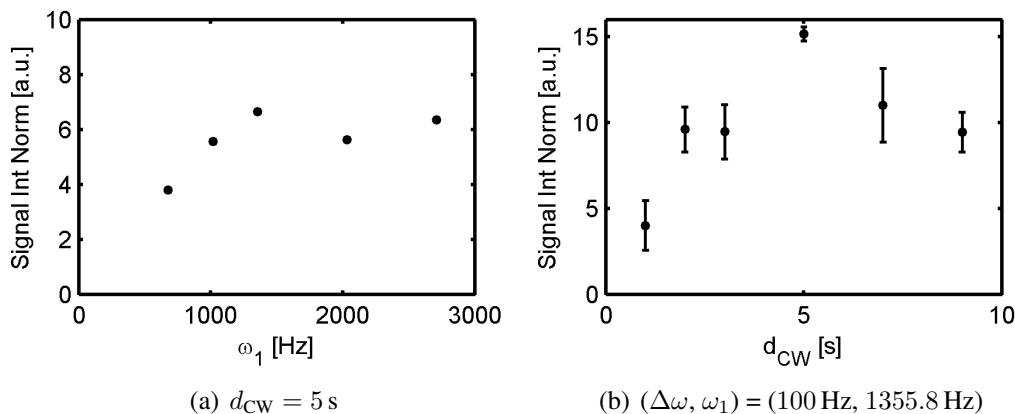


Figure 4.6: Normalized signal integral after a CW pulse depending on (a) the RF strength ω_1 and (b) the CW pulse duration d_{CW} . In (b) the mean and the standard deviation values of four measurements are shown.

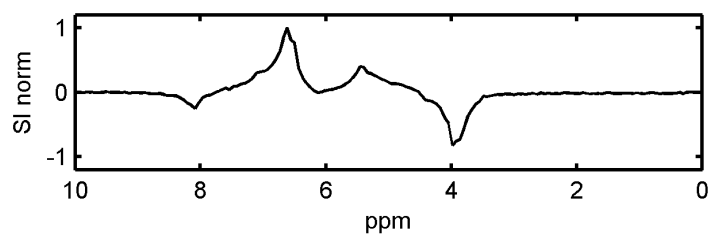
the vinyl group:

$$\omega_1 = \tan \left(\arccos \left(\frac{B_{res}}{B_0} \right) \right) \Delta\omega. \quad (4.16)$$

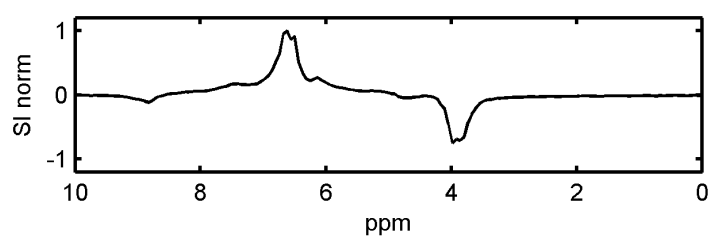
The sequence was tested for the following $(\Delta\omega, \omega_1)$ combinations using a CW pulse duration d_{CW} of 5 s: (50 Hz, 677.9 Hz), (75 Hz, 1016.9 Hz), (100 Hz, 1355.8 Hz), (150 Hz, 2033.7 Hz) and (200 Hz, 2711.6 Hz).

The spectra for the different $(\Delta\omega, \omega_1)$ combinations are shown in figure 4.7. Due to the varying amount of hyperpolarization, the spectra were normalized each with the maximum signal intensity. Therefore, they should be interpreted only qualitatively. For the lowest used combination strong distortions of the expected spectrum were found. These distortions are much smaller but also visible for the combination (75 Hz, 1016.9 Hz). In figure 4.6a the dependence of the vinyl group integral is shown. Each integral was normalized with the corresponding reference measurement. The signal integral increases fast until $\omega_1 = 1355.8$ Hz. For higher values it seems that a plateau is reached. Due to these results, the combination (100 Hz, 1355.8 Hz) was used for further investigations.

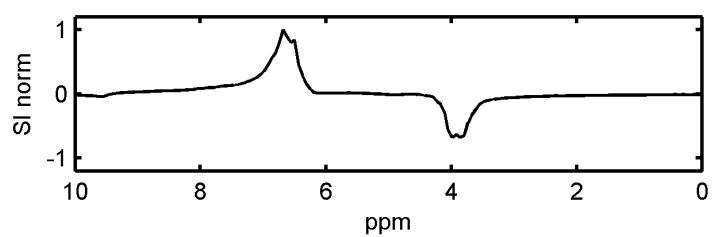
Using the combination (100 Hz, 1355.8 Hz) the signal was acquired for different CW pulse durations d_{CW} using 1 s, 2 s, 3 s, 5 s, 7 s and 9 s. The maximum signal was found for a duration of 5 s (cf. Fig. 4.6b). These measurements were repeated four times. Further analysis of the singlet triplet conversion using the CW pulse can be found in section 4.3 on page 68.



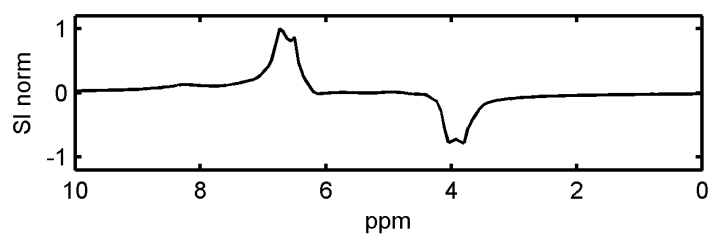
(a) (50 Hz, 677.9 Hz)



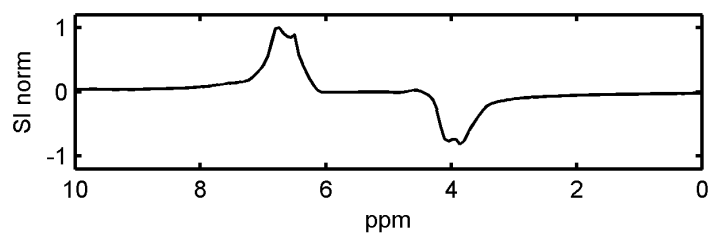
(b) (75 Hz, 1016.9 Hz)



(c) (100 Hz, 1355.8 Hz)



(d) (150 Hz, 2033.7 Hz)



(e) (200 Hz, 2711.6 Hz)

Figure 4.7: Spectra obtained after a 5 s CW pulse using different $(\Delta\omega, \omega_1)$ combinations. Spectra are normalized each with the maximum signal intensity.

Chemical Shift Scaling Sequence

The chemical shift scaling (CSS) sequence introduced by Morris et al. [2003] consists of a repetitive cycle of eight evenly distributed 180° pulses during the duration τ_1 and an additional delay τ_2 (cf. Fig. 4.5 on page 62). The phases of the pulses follow an XY-16 supercycle (x,y,x,y,y,x,y,x,-x,-y,-x,-y,-y,-x,-y,-x) [Gullion et al., 1990]. The sequence generates an effective Hamiltonian which scales the chemical shift by a factor:

$$\lambda = \frac{\tau_2}{\tau_1 + \tau_2}. \quad (4.17)$$

To allow for the singlet triplet conversion, the chemical shift difference among the vinyl and the methyl groups in the dimethyl maleate molecule needs to be scaled from the magnetic field B_0 of 1.5 T to the resonance field of 0.1 T. Four different (τ_1, τ_2) combinations were used fulfilling these condition: (7.52 ms, 0.6 ms), (10.08 ms, 0.8 ms), (12.56 ms, 1.0 ms) and (25.2 ms, 2.0 ms). The number of cycles was set to $n_C = 80$. For the combination (12.56 ms, 1.0 ms) additionally 20 and 160 cycles were tested. The RF strength ω_1 of the 180° pulses was set to 1.0 kHz resulting in a pulse duration of $500 \mu\text{s}$.

The spectra of the combination (12.56 ms, 1.0 ms) using different number of cycles are shown in figure 4.8. No major qualitative differences are visible between the spectra. However, the methyl group peak shows some disturbances which are less evident for $n_C = 80$ because the amplitude is bigger. They might be caused by overlaying thermal signal. The variation of the number of cycles show that the conversion clearly increases from 10 to 80 cycles (Fig. 4.9a). A further benefit by another increase of n_C was not observed. Even a small reduction of the signal was yielded by an increase of the cycles from 80 to 160. The (τ_1, τ_2) combinations (7.52 ms, 0.6 ms) and (10.08 ms, 0.8 ms) show much higher signal intensities than the two combinations with higher values (Fig. 4.9b). Further analysis of the singlet triplet conversion using the CSS pulse sequence can be found in the following section.

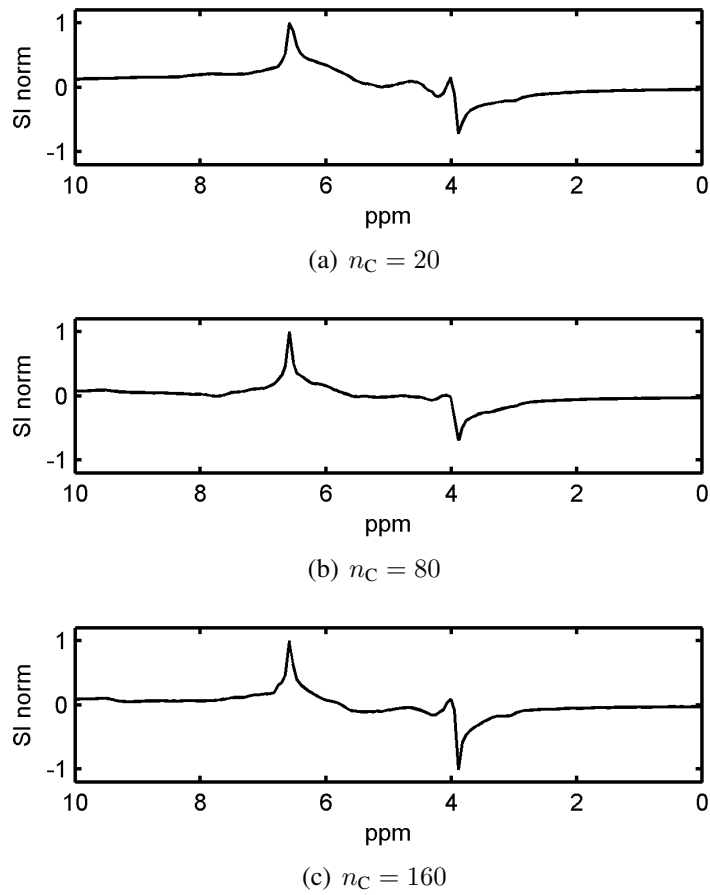


Figure 4.8: Spectra obtained after a CSS pulse sequence using the τ combination (12.56 ms, 1 ms). Spectra are normalized each with the maximum signal intensity.

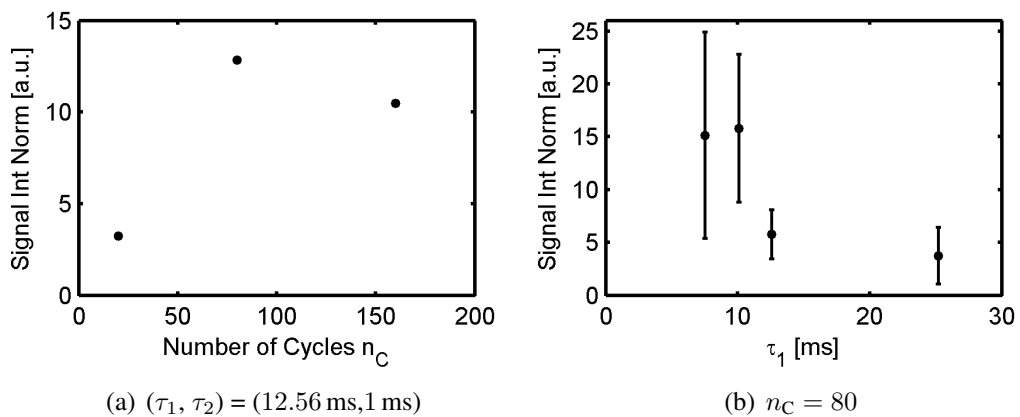


Figure 4.9: Normalized signal integral after a CSS pulse sequence depending on (a) the number of cycles n_C and (b) the (τ_1, τ_2) combination. In (b) the mean and the standard deviation values of four measurements are shown.

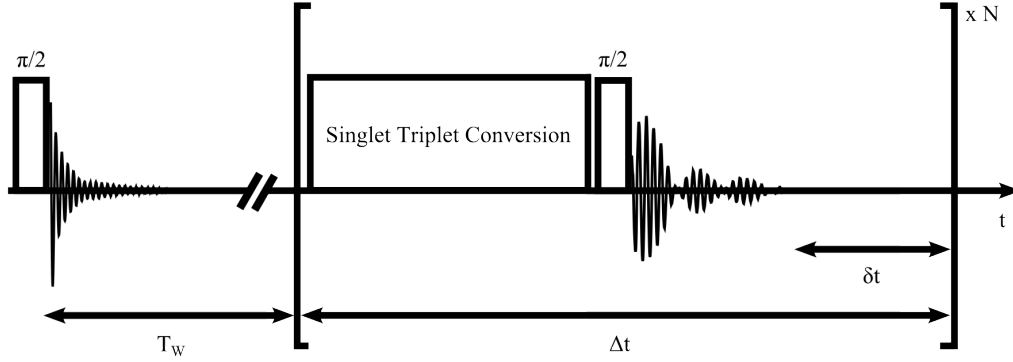


Figure 4.10: Multiple Conversion Experiment. After the waiting time T_w the singlet triplet conversion is repeated N times using a repetition time Δt .

4.3 Multiple Conversion Experiment

In the previous section, it was shown that the conversion of the singlet to the triplet state can be realized by an RF pulse sequence. The use of a pulse sequence in comparison to field cycling opens up for multiple conversions after one shake in a controlled and reproducible way (cf. Fig. 4.10). In the following, the signal-time behavior is analyzed, in the first instance neglecting the longitudinal relaxation of the triplet spin state. The signal after a delay T_w between the shake and the first conversion is given by:

$$S_0 \propto \xi A_{\text{Singlet}}(T_w) \quad (4.18)$$

with $A_{\text{Singlet}}(T_w)$ being the amount of the system in the singlet state after the waiting time T_w and ξ being the fraction of singlet state which is converted into the triplet state by the RF pulse sequence. If the conversion is repeated after Δt then the second signal is given by:

$$S_1 \propto \xi \left[(1 - \xi) A_{\text{Singlet}}(T_w) \right] \exp \left(- \frac{\Delta t}{T_{\text{Singlet}}} \right) \quad (4.19)$$

with the term in square brackets being the part of the system, which stays in the singlet state after the first conversion decaying exponentially with the lifetime of the singlet state T_{Singlet} . The second signal is therefore given by:

$$S_1 = S_0 (1 - \xi) \exp \left(- \frac{\Delta t}{T_{\text{Singlet}}} \right) \quad (4.20)$$

Repeating this iteratively, it can be shown that the signal after the $(n + 1)^{\text{th}}$ conversion is given by:

$$S_n = S_0 (1 - \xi)^n \exp \left(- n \frac{\Delta t}{T_{\text{Singlet}}} \right). \quad (4.21)$$

Using the exponential relation $a^x = \exp(x \ln(a))$ and normalizing with the first signal S_0 , equation 4.21 can be transformed to:

$$\frac{S_n}{S_0} = \exp(-D_C(\Delta t)n), \quad (4.22)$$

with the characteristic exponential decay of the multiple conversion experiment:

$$D_C(\Delta t) = \frac{1}{T_{\text{Singlet}}}\Delta t - \ln(1 - \xi), \quad (4.23)$$

being a linear function of the conversion repetition time Δt . The slope is determined by the singlet state lifetime T_{Singlet} and the intersection with the y axis by the conversion fraction ξ .

In practice, this means that the lifetime and the conversion fraction can be determined by repeating the multiple conversion experiment with different repetition times Δt . As an example, this is shown in figure 4.11 for a CW pulse with a duration of 5 s, an RF strength ω_1 of 1355.8 Hz and the associated offset $\Delta\omega$ of 100 Hz. The experiments were performed with a conversion repetition time Δt of 10.5 s, 15.5 s, 25.5 s, 35.5 s and 55.5 s using 20, 20, 15, 10 and 10 conversions, respectively. The exponential fits of the normalized signal integrals as well as the linear fit of the characteristic exponential decay values are shown in figure 4.11. With the linear fit parameters a lifetime T_{Singlet} of (3.9 ± 0.4) min and a conversion fraction ξ of 6.7% were calculated.

To be rigorous, the signal-time behavior should be analyzed taking into account the triplet spin state relaxation T_1 . The efficiency of the RF pulse sequence is limited by the triplet state relaxation time T_1 , which causes the converted singlet states to relax with the fast T_1 relaxation. This effect can be included in equation 4.18:

$$S_0^* \propto \rho\xi A_{\text{Singlet}}(T_W) \quad (4.24)$$

with $\rho(T_1, d_{\text{RF}})$ being a function of the relaxation time and the duration of the RF pulse sequence. In analogy to equation 4.19 the signal after the second conversion is then given by:

$$S_1^* \propto \rho\xi \left[(1 - \xi) A_{\text{Singlet}}(T_W) \right] \exp\left(-\frac{\Delta t}{T_{\text{Singlet}}}\right). \quad (4.25)$$

The signal is also reduced by the factor ρ , but the term in square brackets reflecting the part of the system in the singlet state is not effected by this loss. The normalized signal

$$\frac{S_n^*}{S_0^*} = (1 - \xi)^n \exp\left(-n\frac{\Delta t}{T_{\text{Singlet}}}\right) \quad (4.26)$$

is therefore not changed by the longitudinal relaxation T_1 and therefore also not the deter-

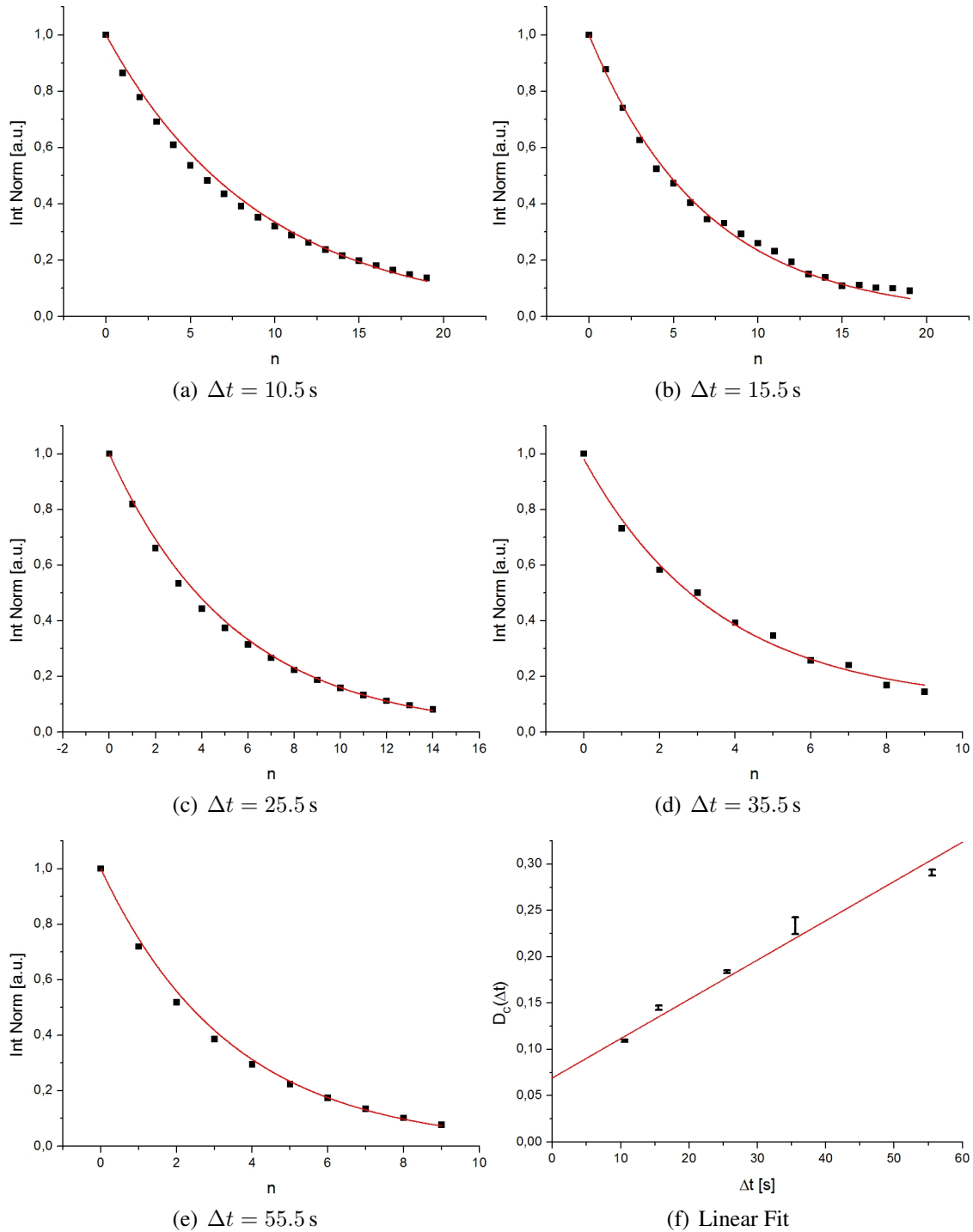


Figure 4.11: Exponential decay of the signal in a multiple conversion experiment for different repetition times. With the parameters of the linear fit of the characteristic exponential decay D_C shown in (f) a lifetime T_{Singlet} of 3.9 min and a conversion fraction ξ of 6.7% were calculated.

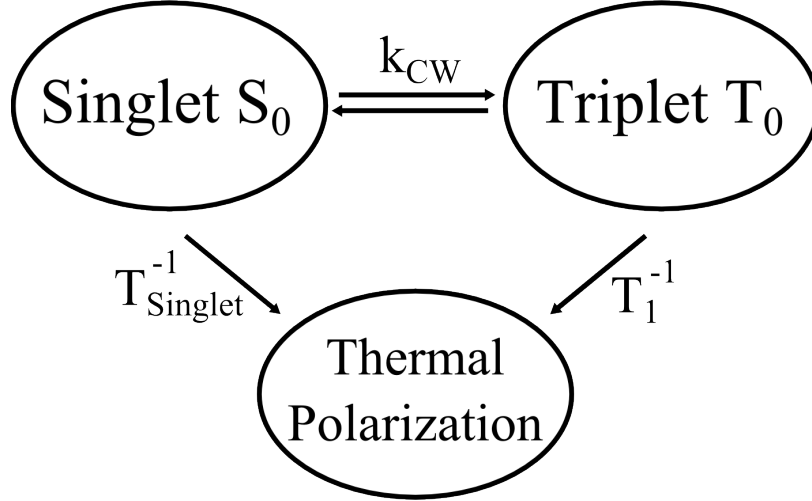


Figure 4.12: Model of the singlet triplet conversion. A constant conversion rate k_{CW} is assumed during the CW pulse. The triplet state T_0 relaxes with the longitudinal relaxation time T_1 to the thermal polarization. For the theoretical calculations the relaxation of the singlet state S_0 during the CW pulse was neglected.

mination of the singlet state lifetime and the conversion fraction. However, to maximize the signal after one conversion, it is necessary to maximize the product of ρ and ξ , which is in the following named the effective conversion fraction:

$$\xi_{\text{eff}} = \rho(T_1, d_{\text{RF}})\xi. \quad (4.27)$$

The multiple conversion experiment is used in the following to analyze the continuous wave and the chemical shift scaling sequence.

4.3.1 Continuous Wave

In a simplified classical model, the conversion of the singlet to the triplet state during a continuous wave pulse can be estimated by a constant conversion rate k_{CW} . The triplet state relaxes with T_1 to the thermal polarization whereas the singlet state relaxes with the singlet state lifetime T_{Singlet} . Since T_{Singlet} is much longer than the used pulse durations it should be neglected in the following. Furthermore, the thermal polarization is neglected. The model is schematically shown in figure 4.12. This yields the following differential equations to describe the amount of singlet state A_{Singlet} and the amount of triplet state A_{Triplet} :

$$\frac{dA_{\text{Singlet}}}{dt} = -k_{CW}(A_{\text{Singlet}} - A_{\text{Triplet}}), \quad (4.28)$$

$$\frac{dA_{\text{Triplet}}}{dt} = -k_{CW}(A_{\text{Triplet}} - A_{\text{Singlet}}) - \frac{1}{T_1}A_{\text{Triplet}}. \quad (4.29)$$

Equation 4.29 can be rearranged to solve for A_{Singlet} :

$$A_{\text{Singlet}} = \frac{1}{k_{\text{CW}}} \frac{dA_{\text{Triplet}}}{dt} + \left(1 + \frac{1}{k_{\text{CW}}T_1}\right) A_{\text{Triplet}}. \quad (4.30)$$

Insertion of equation 4.30 into equation 4.28 yields a decoupled differential equation of A_{Triplet} :

$$0 = \frac{d^2 A_{\text{Triplet}}}{dt^2} + \left(2k_{\text{CW}} + \frac{1}{T_1}\right) \frac{dA_{\text{Triplet}}}{dt} + \frac{k_{\text{CW}}}{T_1} A_{\text{Triplet}}. \quad (4.31)$$

The ansatz $A_{\text{Triplet}} = a_1 + a_2 \exp(-k_1 t) + a_3 \exp(-k_2 t)$ with the boundary conditions $A_{\text{Triplet}}(t = 0) = 0$ and $A_{\text{Triplet}}(t \rightarrow \infty) = 0$ yields:

$$A_{\text{Triplet}}(t) = \tilde{a} (\exp(-k_1 t) - \exp(-k_2 t)) \quad (4.32)$$

with the characteristic exponential decay rates being:

$$k_{1,2} = k_{\text{CW}} + \frac{1}{2T_1} \pm \sqrt{k_{\text{CW}}^2 + \left(\frac{1}{2T_1}\right)^2}. \quad (4.33)$$

Insertion of the solution of A_{Triplet} into equation 4.30 in combination with the boundary condition $A_{\text{Singlet}}(t = 0) = A_{\text{Singlet}}^0$, yields:

$$A_{\text{Singlet}}(t) = \frac{\tilde{a}}{k_{\text{CW}}} \left[\left(k_{\text{CW}} + \frac{1}{T_1} - k_1\right) \exp(-k_1 t) - \left(k_{\text{CW}} + \frac{1}{T_1} - k_2\right) \exp(-k_2 t) \right] \quad (4.34)$$

with

$$\tilde{a} = A_{\text{Singlet}}^0 \frac{k_{\text{CW}}}{k_2 - k_1}. \quad (4.35)$$

The conversion fraction ξ after a CW pulse with duration d_{CW} is given by:

$$\xi(d_{\text{CW}}) = \frac{A_{\text{Singlet}}^0 - A_{\text{Singlet}}(t = d_{\text{CW}})}{A_{\text{Singlet}}^0}. \quad (4.36)$$

In contrast, the effective conversion fraction ξ_{eff} is given by the relative amount of triplet state at time d_{CW} :

$$\xi_{\text{eff}}(d_{\text{CW}}) = \frac{A_{\text{Triplet}}(t = d_{\text{CW}})}{A_{\text{Singlet}}^0} \quad (4.37)$$

The effective conversion is proportional to the signal shown in figure 4.6 on page 64. At the maximum of the effective conversion fraction, being reached at $d_{\text{CW}}^{\text{opt}}$, the differential of ξ_{eff} must vanish:

$$\left. \frac{\partial \xi_{\text{eff}}}{\partial d_{\text{CW}}} \right|_{d_{\text{CW}}^{\text{opt}}} = 0. \quad (4.38)$$

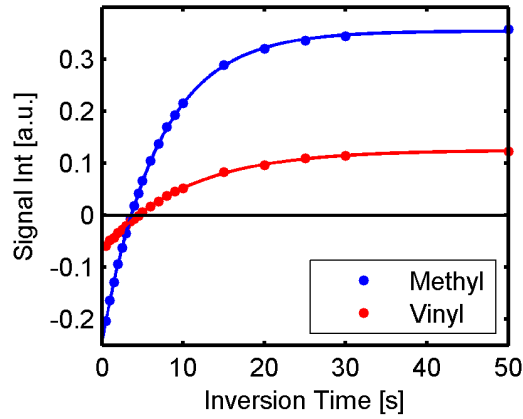


Figure 4.13: T_1 determination of dimethyl maleate using the inversion recovery sequence. The exponential fits yielded an T_1 relaxation time of (10.2 ± 0.2) s for the Vinyl protons and (6.86 ± 0.04) s for the Methyl groups at 1.5 T.

which yields:

$$d_{CW}^{opt} = \frac{\ln(k_2) - \ln(k_1)}{k_2 - k_1} \quad (4.39)$$

The calculation of the temporal evolution of the singlet and the triplet state during the CW pulse requires the knowledge of the triplet state relaxation time T_1 and the conversion rate k_{CW} . Whereas T_1 was determined using a well-known inversion recovery experiment (cf. Fig. 4.13), the conversion rate k_{CW} is given by the slope of the conversion fraction ξ at $d_{CW} = 0$:

$$\left. \frac{\partial \xi}{\partial d_{CW}} \right|_{d_{CW}=0} = k_{CW}. \quad (4.40)$$

The experimental analysis of this behavior was performed for the CW pulse with an RF strength ω_1 of 1355.8 Hz with the associated offset $\Delta\omega$ of 100 Hz. For this purpose, the multiple conversion experiment was executed for CW pulse durations d_{CW} of 1, 2, 3, 5 s, 7 and 9 s. The initial waiting time T_W was set to 3 min. The experiments were performed for delay times δt of 5, 10, 20, 30 and 50 s combined with 20, 20, 15, 10 and 10 repetitions, respectively.

In figure 4.14 on the following page the variation of the singlet state lifetime T_{Singlet} and the conversion fraction ξ depending on the CW pulse duration d_{CW} is shown. As expected, the determined value of the singlet state lifetime is independent of the CW duration. With the determined T_{Singlet} values a weighted average was calculated to be (3.8 ± 0.2) min. The conversion fraction increases with the CW duration d_{CW} . To determine the conversion rate k_{CW} , the initial slope was determined by fitting the ξ values at $d_{CW} = 2$ and 3 s with a line through origin. Due to the evidently larger error of the T_{Singlet} value at $d_{CW} = 1$ s, the ξ value at this position was not used for the k_{CW} determination. The initial slope yields a conversion rate $k_{CW} = 0.0173 \text{ s}^{-1}$.

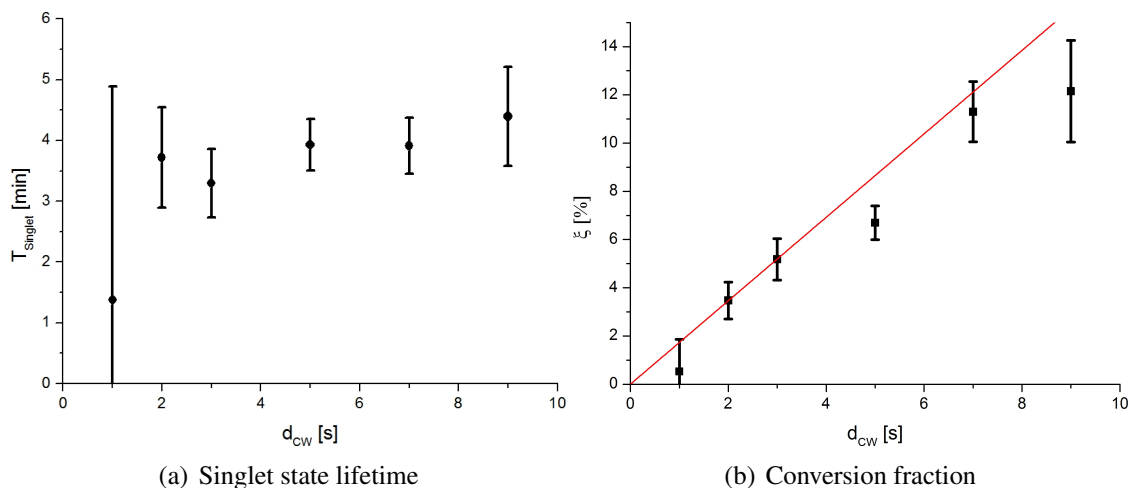


Figure 4.14: Dependency of (a) the singlet state lifetime T_{Singlet} and (b) the conversion fraction ξ on the duration of the continuous wave pulse d_{CW} . The red line in (b) shows the linear fit of the ξ values at 2 and 3 s with a line through origin to determine the initial slope of ξ which is equivalent to the conversion rate k_{CW} .

The theoretical predictions, as a function of d_{CW} , for the conversion fraction ξ (Eq. 4.36) and the effective conversion fraction ξ_{eff} (Eq. 4.37) are shown in figure 4.15 on the next page. The curves were calculated using $k_{\text{CW}} = 0.0173 \text{ s}^{-1}$ and $T_1 = 5, 10$ and 15 s . The T_1 relaxation time does not influence much the conversion fraction ξ . On the other hand, the effective conversion fraction ξ_{eff} is clearly dependent on T_1 , changing the optimal duration d_{CW} and the maximum possible effective conversion fraction. In figure 4.16 a comparison of the effective conversion predicted by the model and the experimental results shown in figure 4.6 on page 64 is shown. With the determined conversion rate of $k_{\text{CW}} = 0.0173 \text{ s}^{-1}$ and a manually adjusted T_1 of 1.4 s , the position of the maximum and the course of the theoretical curve are in good agreement with the experimental data. The experimental data was scaled by a factor of 0.2 which is justifiable since the normalized signal values (Fig. 4.6b) are proportional to the effective conversion fraction. With this parameters the maximum effective conversion fraction ξ_{eff} is reached for $d_{\text{CW}}^{\text{opt}} = 5.3 \text{ s}$. The conversion fraction ξ for this duration is 6.7% whereof following the theoretical model only 25% can be used for the acquisition.

4.3.2 Chemical Shift Scaling Sequence

The multiple conversion experiment was also performed using the CSS sequence. The following (τ_1, τ_2) combinations were used: (7.52 ms, 0.6 ms), (10.08 ms, 0.8 ms), (12.56 ms, 1.0 ms) and (25.2 ms, 2.0 ms). The number of cycles n_{C} was set to 80. The first conversion was delayed by an initial waiting time T_{W} of three minutes. As for the CW multiple conversion, the experiment were performed with delay times δt of 5, 10, 20, 30 and 50 s

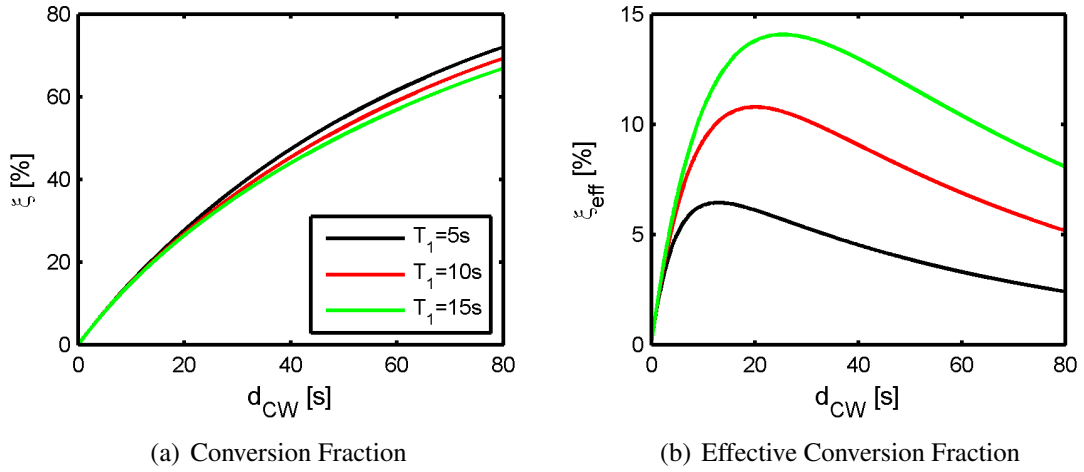


Figure 4.15: Conversion fraction ξ and the effective conversion fraction ξ_{eff} calculated with equations 4.36 and 4.37 using $k_{CW} = 0.0173 \text{ s}^{-1}$ and $T_1 = 5, 10$ and 15 s .

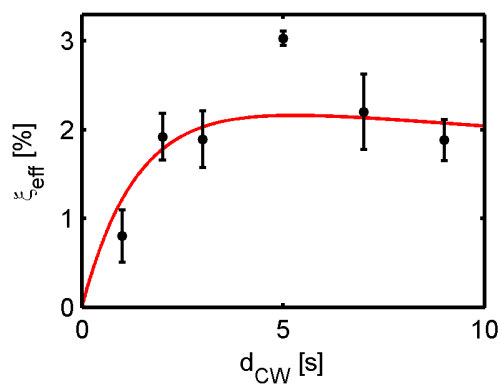


Figure 4.16: Comparison of model and experimental results. The effective conversion fraction curve was achieved using $k_{CW} = 0.0173 \text{ s}^{-1}$ and $T_1 = 1.4 \text{ s}$.

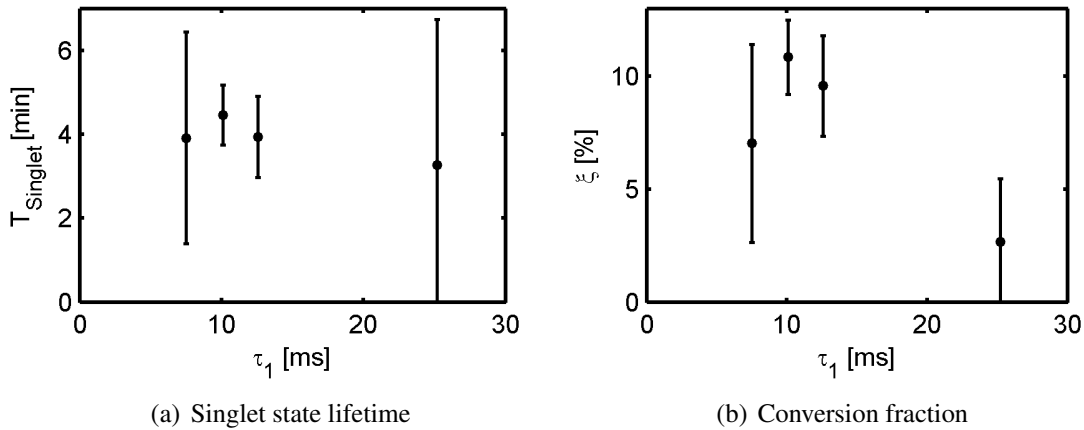


Figure 4.17: Dependency of (a) the singlet state lifetime T_{Singlet} and (b) the conversion fraction ξ on the τ combination.

combined with 20, 20, 15, 10 and 10 repetitions, respectively.

As expected, the lifetime of the singlet state does not depend on the used τ combination (cf. Fig. 4.17a). With the achieved values a weighted average was calculated: $T_{\text{Singlet}} = (4.2 \pm 0.6)\text{min}$, which is in good agreement with the value obtained by using the CW pulses ($(3.8 \pm 0.2)\text{min}$) and the field cycling. The conversion fraction ξ is maximal for the combination (10.08 ms, 0.8 ms) (actually, the first three combinations are not clearly distinguishable in the range of errors). However, for the combination (25.2 ms, 2.0 ms) the conversion fraction is four times lower in comparison to the maximum value. The explanation of the effect of the parameters n_C and (τ_1, τ_2) on the conversion fraction is addressed in the discussion in section 4.5.

4.4 Imaging

The aim of this section is to combine the singlet triplet conversion with magnetic resonance imaging. For this purpose, a gradient echo sequence was used combined with CSS multiple conversion sequence. Prior to every phase encoding step the singlet triplet conversion was executed by the CSS sequence (n_C : 80, τ_1 : 12.56 ms, τ_2 : 1 ms). A centric reordering scheme was used for the phase encoding. A 90° rectangular pulse was used for the excitation of the gradient echo sequence resulting in a projection image of the sample. A field of view (FOV) of 20x20 mm was sampled with 16x16 pixels. The repetition time of the sequence TR was set to 1.7 s. The sequence scheme is depicted in figure 4.18. After the first singlet triplet conversion an FID was acquired which was used as reference for determining the amount of generated singlet state by the hydrogenation.

As shown in the previous section, the amount of measurable magnetization after the

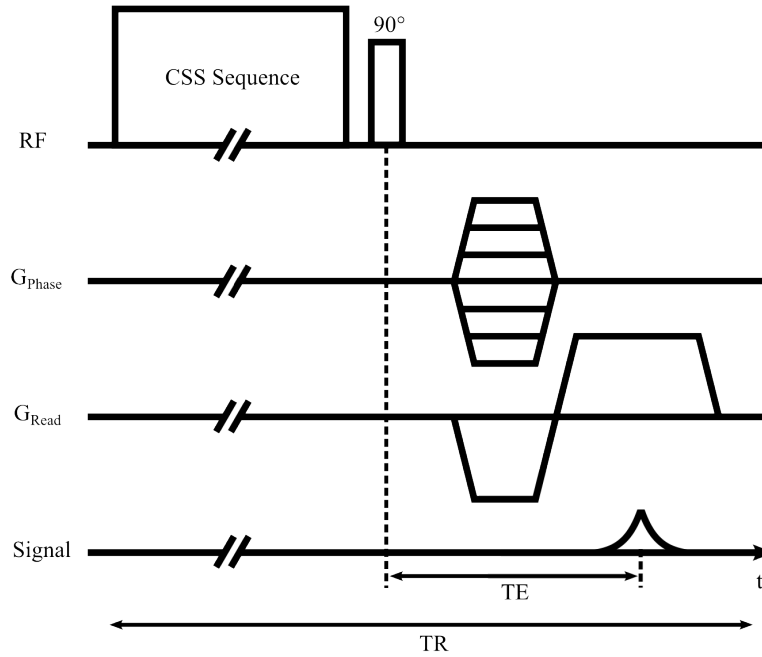


Figure 4.18: Imaging sequence scheme. Before every phase encoding step of the gradient echo sequence a singlet triplet conversion was performed by the CSS sequence. The duration of the CSS sequence (1 s) is illustrated considerably shortened. The used echo times TE are between 3 ms and 14 ms.

singlet triplet conversion decays exponentially with the multiple conversions. This yields an inhomogeneous weighting of the k-space resulting in a broadening of the image in phase direction. More precisely, an image I can be described mathematically as the folding of the object O with a kernel called point spread function PSF :

$$I = PSF * O. \quad (4.41)$$

The exponential decay of the magnetization yields a Lorentzian shape of the PSF in phase encoding direction. To avoid this broadening, a reference measurement was performed using a multiple conversion with the same CSS sequence parameters and the same repetition time TR. The data points were fitted with an exponential function, which was used to correct the k-space data of the imaging experiment (cf. Fig. 4.19).

Magnetic resonance imaging of a spin system with different chemical shifts and J-couplings requires an adequate choice of the echo time TE as shown by Dechent et al. [2012] for ^1H imaging of the PHIP hyperpolarized molecules hexene and hydroxyethyl propionate. For the gradient echo sequence, the echo time behavior is represented by temporal evolution of the absolute values in the FID. The sequence was tested for five different echo times: 3 ms, 5.5 ms, 8 ms, 11.5 ms and 14 ms. A factor 2 zero filling was used to improve the representation of the images yielding 32x32 pixels.

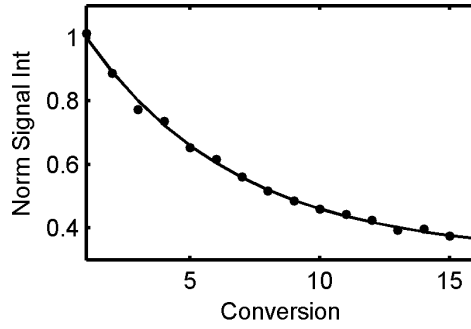


Figure 4.19: Reference measurement. Exponential decay of the signal using multiple singlet triplet conversions. The data was fitted with an exponential function.

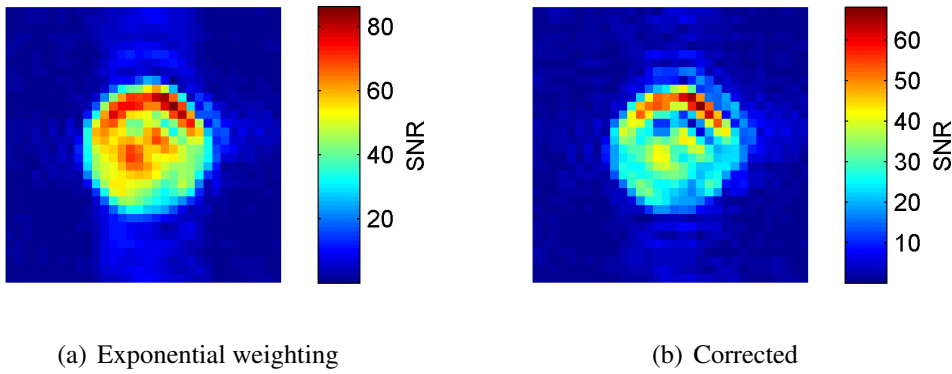


Figure 4.20: Comparison of the images (a) without and (b) with the correction of the exponential weighting of the k-space lines.

In figure 4.20 the image for TE=8 ms with and without the k-space line correction is shown. The artifacts in phase encoding direction outside the NMR tube are reduced. Inside the NMR tube strong inhomogeneities occur which are caused mainly by susceptibility artifacts. The correction of the exponential decay increases the contribution of the outer k-space lines yielding a higher resolution. This yields an visual increase of the inhomogeneities inside the NMR tube. Furthermore, the SNR (signal-to-noise ratio) is reduced in the corrected images since k-space lines with a lower SNR get a higher contribution. The corrected image shows an SNR up to 65. Notice that the proton image was acquired after a waiting time of 3 min inside the observation field

Due to the inhomogeneities, the signal intensity (SI) for a given echo time was not calculated by the mean signal inside the NMR tube. Instead, the mean of the pixels being higher than 80% of the maximum value in the image was taken. This value was corrected by the noise and normalized with the integral of the vinyl group in the reference measurement:

$$SI_{\max, \text{norm}} = \frac{SI_{>80\%} - SI_{\text{noise}}}{Int_{\text{ref}}}, \quad (4.42)$$

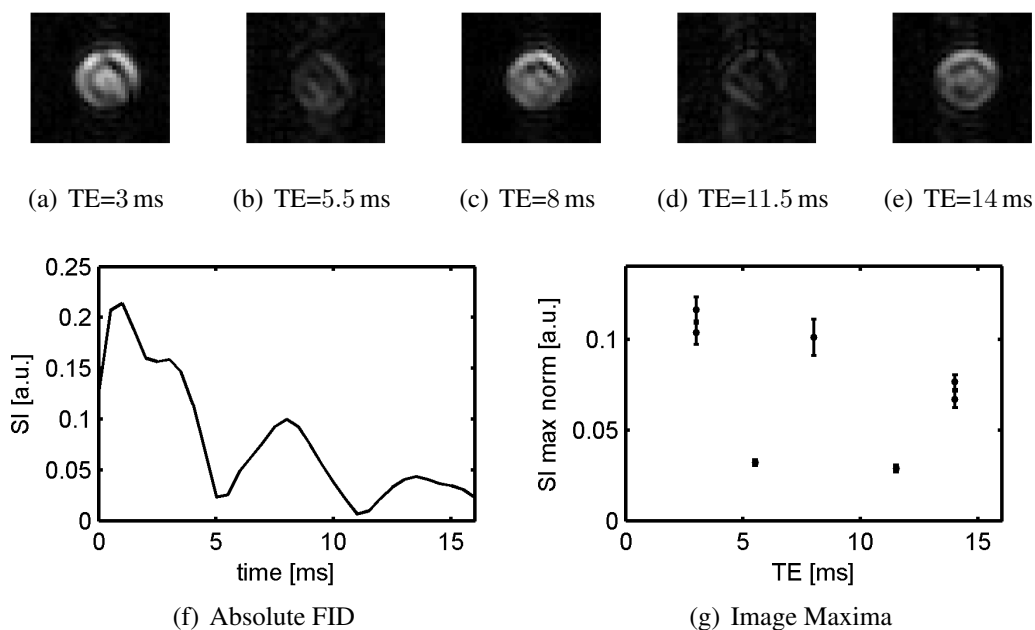


Figure 4.21: Signal's echo time dependence. On top, the images acquired with five different echo times are shown. Bottom, (f) FID's absolute values and (g) the maximal intensity of each image as a function of the echo time. The oscillation pattern is reproduced. The images for 3 ms and 14 ms were measured twice.

whereas the noise signal was calculated by the mean signal in a noise region.

Figure 4.21 shows the FID's absolute values of dimethyl maleate after the singlet triplet conversion together with the echo time dependence of $SI_{\max, \text{norm}}$. The oscillation of the signal intensity with the echo time is noticeable (Fig. 4.21g). Even though the signal at the maximum position decays slower than in the FID, the position of the echo times minima (5.5 ms and 11.5 ms) are in agreement.

4.5 Discussion

4.5.1 Reference Measurement

As mentioned in section 4.2, it is assumed that the signal contributions from hyperpolarized states in the reference measurement are caused by the small amount of hydrogenated molecules generated in the short duration between pressurizing and crossing of the resonance field. Following this assumption, the use of the reference measurement for normalization is justifiable since the activity of the catalyst mainly influences the amount of hydrogenated molecules, whereas it influences the reference and the main measurement similarly. However, other parameters like the transportation time from earth field to the position inside the magnetic bore, the duration of shaking and the shaking method could

differ among the two measurements introducing additional sources of error for this normalization method. Certainly, a more detailed analysis of this effect has to be addressed in future studies.

4.5.2 Multiple Conversion Experiment

The multiple conversion experiment yields a stable and accurate tool to measure the singlet state lifetime T_{Singlet} and the conversion fraction ξ achieved for the singlet triplet conversion. It overcomes the disadvantages of the signal normalization used for the single conversion since it can be normalized intrinsically with the signal after the first conversion.

The method is not limited but considerably simplified by the use of RF pulse sequences for the singlet triplet conversion. Realization of the multiple conversion experiment for the field cycling method requires additional hardware to achieve a precise timing of the experiment. This comprises e.g. an automatic controlled transport system being triggered by the NMR system.

So far the multiple conversion experiment yields only the conversion fraction ξ and not the effective conversion ξ_{eff} which describes the amount of magnetization being detectable. However, the method should be adaptable to measure ξ_{eff} . It is suggested that this can be realized by using the multiple conversion with alternating sets of RF pulse sequence parameters.

4.5.3 Singlet State Lifetime

The lifetime of the singlet state T_{Singlet} at 1.5 T was determined either by the field cycling method ((4.0 ± 1.2) min) or by the RF pulse sequences in combination with the multiple conversion experiment (CW: (3.8 ± 0.2) min; CSS: (4.2 ± 0.6) min). The values are in good agreement.

In general, the main singlet state relaxation mechanisms are the following [Pileio et al., 2012, Levitt, 2012]:

$$T_{\text{Singlet}}^{-1} = R^{\text{CSA}} + R^{\text{leak}} + R^{\text{DD}} + R^{\text{others}} \quad (4.43)$$

with R^{CSA} the rate caused by the motional modulation of the chemical shift anisotropy (CSA) tensor, R^{leak} the singlet-triplet leakage, R^{DD} the rate due to the dipole-dipole (DD) couplings and R^{others} including minor relaxation mechanism. The singlet-triplet leakage is caused by J-couplings to nuclei outside the pair and the small chemical shift difference $\Delta\nu$ which in the Cs-symmetric molecule is zero. The J-coupling contribution to R^{leak} in the dimethyl maleate molecule is relatively inefficient at 1.5 T since this is far away from the resonance field of 0.1 T. As mentioned in the theory of this chapter, the dipole-dipole relaxation is not caused by the intrapair DD coupling but by intramolecular out-of-pair DD

couplings¹ and intermolecular DD couplings. In contrast to the CSA relaxation rate, which is proportional to the square of the magnetic field B_0^2 , the DD rate is field-independent. One of the minor relaxation mechanisms for the liquid singlet state, summarized in R^{others} , is e.g. spin-rotation relaxation which is caused by the interaction of the nuclear spins with local magnetic fields.

Franzoni et al. [2012] determined the singlet state lifetime at 7 T to be (4.0 ± 0.4) min. In the order of errors this is not distinguishable from the lifetime at 1.5 T. Therefore, it is assumed that the dominant contribution to the singlet state relaxation of the vinyl protons in dimethyl maleate is not CSA and therefore given by the dipole-dipole couplings. The contribution of the intramolecular out-of-pair DD coupling and the intermolecular DD coupling to nuclei in the solvent should be investigated in a future study.

4.5.4 RF Pulse Sequences

Two RF pulse sequences were proved to accomplish the singlet triplet conversion inside the clinical MRI system. Both show a good feasibility to realize the singlet triplet conversion avoiding the movement of the sample.

Continuous Wave

The sequence, normally used for chemical shift cancellation or decoupling, was adapted to generate the singlet triplet transition. A theoretical model was developed to understand the characteristics of the singlet triplet conversion during the CW pulse (cf. Fig. 4.12 on page 71). The $(\Delta\omega, \omega_1)$ combination defines the conversion rate k_{CW} . The conversion fraction ξ increases with the duration d_{CW} of the CW pulse. However, due to the relaxation of the generated triplet state the effective conversion ξ_{eff} is maximized for a certain duration depending on the relaxation time T_1 and the conversion rate k_{CW} . For the used combination (100 Hz, 1355.8 Hz) a conversion rate k_{CW} of 0.0173 s^{-1} was found. The model and the measurements show a good agreement using a T_1 relaxation time of 1.4 s which is shorter than the longitudinal relaxation time determined using an inversion recovery experiment ($T_1 = 10.2 \text{ s}$). The reduction of the relaxation time is caused by the saturation effect of the continuous wave. A sufficiently long interval of RF irradiation equalizes the populations of the triplet states $|T_+\rangle$, $|T_0\rangle$ and $|T_-\rangle$ [Levitt, 2008], i.e. the CW pulse destroys the hyperpolarized triplet spin state. Therefore, the CW pulse generates hyperpolarized triplet spin state by enabling the singlet triplet transition but shortens its lifetime due to the saturation character. In a further study the dependency of the parameter k_{CW} on the RF field strength ω_1 should be analyzed.

¹Intramolecular out-of-pair DD couplings occur between one spin participating in the singlet state and another spin within the same molecule.

CSS Sequence

Again, as the mechanism behind the singlet triplet transition in the Cs-symmetrical molecule is understood, it was possible to establish the correct scaling parameters in order to implement the known CSS sequence for singlet triplet conversion.

Beside that, the properties of the CSS sequence are more complex to understand. The model used for the CW pulse is also applicable but the parameters of the CSS sequence ($n_C, (\tau_1, \tau_2)$) change both the sequence duration d_{CSS} as well as the conversion rate k_{CSS} .

The duration of the CSS sequence is given by:

$$d_{\text{CSS}} = n_C(\tau_1 + \tau_2), \quad (4.44)$$

which can be transformed using Eq. 4.17 to:

$$d_{\text{CSS}} = \frac{1}{1 - \lambda} n_C \tau_1 \quad (4.45)$$

Both parameters linearly increase the duration d_{CSS} . However, in contrast to the CW pulse the conversion fraction ξ does not monotonically increase with τ_1 (cf. Fig. 4.17b).

The CSS sequence works in a sense of an average Hamiltonian. In this theory the Hamiltonian operator during a period sequence is expanded as a 'desired' zero-order average Hamiltonian and terms of higher order [Ernst et al., 1990]. The contribution of the higher order terms depends on the repetition period (τ_C)ⁿ (in our case $\tau_C = \tau_1 + \tau_2$). Therefore, an increase of the τ_C durations increases the higher order contributions affecting the zero order approximation. This could explain the reduction of the conversion fraction ξ found for the highest τ combination (cf. Fig. 4.17b).

The RF strength ω_1 of the pulses should rather directly influence the conversion rate in the commonly used RF strength range. However it limits the minimal possible τ_1 duration. Furthermore, the relation of the pulse duration and the delay between the pulses might influence the contribution of higher order terms.

The number of cycles n_C also yield an imperfection of the effective Hamiltonian since the phase errors cumulatively increase with the number of used pulses.

Further analysis and measurements are necessary to achieve a more detailed understanding of the impacts on the singlet triplet conversion by the CSS sequence.

Comparison

The maximum normalized signal intensity is in the same range for the CW and the CSS sequence (cf. Fig 4.6b and 4.9b). However, the maximum was reached for the CSS sequence with a shorter sequence duration (CSS: 0.9 s; CW: 5 s). This on one side increases the ratio of the converted singlet state which can be used for acquisition since less triplet

state magnetization is lost due to longitudinal relaxation. On the other side it allows for shorter repetition times of the conversion. Moreover, it is assumed that the saturation effect of the CSS sequence is weaker in comparison to the CW pulse.

The main motivation of the implementation on a clinical MRI system is the future use of the method for *in vivo* applications. A critical value for *in vivo* applications is the energy of the RF pulses. The CW pulse with a duration d_{CW} of 5 s and a RF strength ω_1 of 1355.8 Hz has a RF energy of $9.2 \times 10^6 \text{ s}^{-1}$ (in units of \hbar). In comparison the energy of the CSS sequence using 80 cycles and an RF strength of 1000 Hz has an RF energy of $3.2 \times 10^5 \text{ s}^{-1}$ which is a factor of 30 less than the CW pulse.

For these reasons the CSS pulse is more advantageous than the CW pulse for *in vivo* applications. However, the use of a train of 180° pulses requires an adequate flip angle calibration. The inhomogeneity of the B_1 field reduces the efficiency of the sequence which is partially compensated by the high order phase cycling scheme. Adiabatic pulses being based on a simultaneous variation of both the RF strength and the phase show higher stability towards B_1 field inhomogeneity [Tannus and Garwood, 1997]. However, they are not suitable for the CSS sequence since they typically have durations longer than 4 ms. Therefore, the stability of the CSS sequence towards B_1 inhomogeneities in the range of *in vivo* application could be improved in future studies.

4.5.5 Imaging

The potential to combine the CSS sequence with imaging sequences has been shown. The CSS sequence was applied prior every phase encoding step of a gradient echo sequence. This strongly limits the amount of phase encoding steps due to the exponential decay of the signal with the number of applied conversions. It was shown that this exponential decay can be corrected. This correction reduces the width of the point spread function increasing the resolution in the image. On the contrary, the correction of the exponential decay reduces the signal to noise ratio in the images since k-space lines with lower SNR get a higher contribution. Moreover, the increase of the resolution makes the effect of susceptibility artifacts more evident, leading to a reduced image quality. Therefore, further investigations should be performed on the postprocessing of the data to find a compromise between PSF optimization and SNR.

Alternatively, one singlet triplet conversion can be combined with a single shot acquisition sequence like EPI (echo planar imaging) or RARE (rapid acquisition with relaxation enhancement). This enables image series within a range of minutes due to the long singlet state lifetime.

The limitation in the amount of phase encoding steps can be solved by combining the imaging method with parallel acquisition techniques.

Besides, the necessity of an adequate echo time selection was shown for dimethyl

maleate as previously shown by Dechent et al. [2012] for ^1H imaging of the PHIP hyperpolarized molecules 1-hexene and HEP.

4.5.6 Chemical Limitations

A main limitation in the use of the dimethyl maleate molecule as a long-lived nuclear spin state is the small amount of conversion achieved by the catalyst. After six shakes the vinyl peak in the thermal spectrum was still not visible (cf. Fig. 4.3). An improvement of the chemical reaction would directly improve the SNR found in the images.

Additionally, for *in vivo* applications the biocompatibility of the mixture needs to be guaranteed. Dimethyl maleate, acetone as well as the catalyst are toxic. Therefore, either biocompatible Cs-symmetric molecules need to be found or methods need to be developed guaranteeing the biocompatibility (e. g. encapsulation in a polymer shell).

4.5.7 Comparison to Other Studies

There are a lot of publications in the field of long-lived nuclear spin states. In the following, four state of the art publications are presented which are best suitable for comparison with the results of this PhD thesis.

Warren et al. [2009] reported first the use of a singlet spin state of a chemically equivalent ^{13}C spin pair. For this purpose, they used the DNP hyperpolarized spin state of the monohydrate of 2,3- ^{13}C -labeled diacetyl. By the combination of an RF pulse sequence perturbation and dehydration of the monohydrate in acetone they locked parts of the hyperpolarization in the long-lived singlet spin state of the Cs-symmetric molecule diacetyl. Rehydration caused by the injection of water makes it observable again. Therefore, the observation of the hyperpolarization with this method is mainly based on a chemical reaction.

Laustsen et al. [2012] showed the feasibility of the singlet triplet conversion by an RF pulse sequence in a nearly equivalent spin system performed on a small 4.7 T animal imaging system. They used the DNP hyperpolarized, double ^{13}C labeled and completely deuterated molecule cyclohexyl-isopropyl-1,2- $^{13}\text{C}_2$ -oxalate- d_{18} . To perform the conversion of the transversal magnetization to the singlet state, they used the M2S sequence by Pileio et al. [2010]. The sequence consists of a train of RF pulses at which the sequence timing is calculated with the chemical shift difference $\Delta\nu$ and the J-coupling of the two ^{13}C spins. The reconversion to the transversal magnetization is achieved by applying the mirror image of the M2S sequence (S2M). They measured a ^{13}C singlet state lifetime T_{Singlet} in the utilized molecule of 77 s ($T_1 = 54$ s). They achieved an efficiency of the M2S sequence of 50%.

Feng et al. [2012] adapted the M2S sequence to transfer population in chemically equivalent spin states. For this purpose, they used the Cs-symmetrical double ^{13}C labeled

molecule diethyl oxalate- $^{13}\text{C}_2$ on a small 7 T animal MRI scanner. Using a chemically equivalent spin state, the timing of the sequence is based on the J-coupling network in the molecule (in this case J_{CC} , J_{HH} , J_{CH} and J'_{CH}). They achieved a singlet state lifetime T_{Singlet} of 41 s ($T_1 = 22$ s). The efficiency of the M2S-S2M sequence was in this case 4.5%.

Pileio et al. [2012] analyzed the singlet state relaxation in double ^{13}C labeled nearly equivalent molecules. They measured the ^{13}C singlet state lifetime for two classes of molecules varying the substitutes of the molecules. They found singlet state lifetimes T_{Singlet} of up to 577 s at 9.4 T.

In this PhD thesis, the singlet triplet conversion is realized on a clinical 1.5 T system for the first time. Furthermore, in contrast to the most studies represented by the publications shown here, the hyperpolarized proton singlet spin state yielded via Parahydrogen Induced Polarization was used for the experiments.

The use of double labeled ^{13}C molecules is expensive. In addition, ^{13}C hardware is needed which is not available on every clinical MRI system (^{13}C NMR coil and a broadband amplifier). Beside, the same spatial resolution in a ^{13}C image requires a four times higher gradient strength. Most of the molecules used so far, have singlet state lifetimes in the order of 1 min which is four times less than the lifetime of the proton singlet state in dimethyl maleate. As mentioned before, Pileio et al. [2012] showed recently that there exist ^{13}C singlet spin states with lifetimes up to 10 min.

Conversion efficiencies of up to 10% were found for the CSS sequence. Laustsen et al. [2012] describes an efficiency of 50% for the M2S sequence whereas Feng et al. [2012] only reached around 5%. The reason for this difference can not be clearly found in the publications. Perhaps, it is based on the fact that Laustsen et al. [2012] used a phase cycling scheme. Another explanation might be that Laustsen et al. [2012] worked with nearly equivalent spins. For these spin systems the singlet triplet conversion (and vice versa) is easier to achieve because the singlet state is not an eigenstate (even though it is close). In this spin system they obtained 50% efficiency. On the other hand, the efficiency obtained in this PhD thesis as well as the one obtained by Feng et al. [2012] are both below 10%. However, the systems are in both cases chemically equivalent and therefore the singlet state is an eigenstate. This causes the transition to be more unlikely to occur. It is worth emphasizing that due to the same reason why the conversion is unlikely to happen between chemically equivalent spins, the storage of the singlet state is facilitated.

However, a comparison of the conversion efficiencies yielded in this work with the values found in the literature is limited since the method to achieve them differs. This is because the signal in the dimethyl maleate is only available after the conversion which requires the detection of the conversion efficiency using the multiple conversion experiment. Moreover, the experiments were performed on a clinical system with probably more pronounced hardware imperfections in comparison to a small animal scanner.

The main advantage of using PHIP hyperpolarized protons is based on the fact that the singlet nuclear spin state is directly generated by the hyperpolarization method [Münne-
mann and Spiess, 2011]. This avoids the loss of hyperpolarization caused by the initial
generation of the singlet state which is necessary when using DNP hyperpolarized spin
states. This fact provides a particular advantage for *in vivo* experiments since the hyperpo-
larized molecules can be injected directly after the reaction. Even though the efficiency of
one singlet triplet conversion of 10% is suboptimal, it was shown that the hyperpolarization
can almost completely be used by applying multiple conversions. Using a short repetition
time the loss caused by the singlet state relaxation is small.

Chapter 5

Conclusion and Outlook

In this thesis, two polarization transfer methods were improved to convert the two-spin order of the PHIP spin state for clinical MRI system applications.

Heteronuclear Polarization Transfer

First, the hyperpolarized ^1H spin state in hydroxyethyl propionate was transferred to ^{13}C using the PH-INEPT+ sequence. The sequence timing was optimized both by spin dynamics simulations and experimentally utilizing the continuous PHIP hyperpolarization achieved by hollow-fiber membrane modules. A sequential version of the sequence was developed allowing for the implementation on a clinical MRI system usually equipped with only a single RF transmission channel. The feasibility of performing the polarization transfer inside the clinical NMR scanner was shown. This might avoid the necessity of an additional NMR unit in future PHIP polarizers. A reaction chamber might be fixed first inside an adapted small animal double resonant $^1\text{H}/^{13}\text{C}$ NMR coil. This reaction chamber might be based either on the spray injection of the substrate into the parahydrogen atmosphere or alternatively on the use of hollow-fiber membrane modules. After the reaction, the hyperpolarized molecules would be injected into the animal having only a very short transportation time. This minimizes the loss due to relaxation during the transportation. After the distribution of the molecules inside the animal, the acquisition can be performed with the same NMR coil. The polarization transfer sequence in such a polarizer might be the sequential 1-PH-INEPT+ sequence or alternatively an optimized sequence via optimal control theory. In this work, simulations of such an optimal control sequence yield promising results with an improvement of the polarization transfer by a factor of two.

Long-Lived Nuclear Spin State

Second, the singlet triplet conversion was achieved for the long-lived singlet spin state of the Cs-symmetric molecule dimethyl maleate. The conversion was enabled by field cycling as well as by adapted RF pulse sequences. For this purpose, two sequences were analyzed

and implemented on a clinical MRI system. Using multiple singlet triplet conversions, a tool was developed to robustly determine both the lifetime of the singlet spin state and the conversion fraction achieved by the RF pulse sequence. The lifetime of dimethyl maleate was determined to be 4 min at 1.5 T. As mentioned, in the discussion further chemical improvements are necessary including the efficiency of the catalyst and the biocompatibility for *in vivo* applications. The long hyperpolarization lifetime in these molecules allows for long distribution durations. This enables to achieve a higher accumulation of these molecules in certain tissues or to penetrate metabolic processes. A higher contrast of healthy and pathologic tissue (e. g. cancer) might be achievable.

Both, the hyperpolarized ^{13}C spin state and the converted singlet state were utilized for MR imaging. The echo time dependency was analyzed for both combinations of spin system and imaging sequence. A careful choice of the echo time was shown for both molecules as a requirement to improve the results.

Comparison to DNP

As mentioned in the introduction, dynamic nuclear polarization (DNP) is an alternative method to achieve a hyperpolarized liquid for *in vivo* applications. In contrast to DNP, PHIP is more restricted in the molecules capable for the hyperpolarization method since it requires an unsaturated binding for the hydrogenation. This plays an important role for metabolic imaging at which the hyperpolarized molecule should be able to enter a metabolic process of interest. Several biomolecules are potential agents for the PHIP method: e. g. ^{13}C -succinate, ^{15}N -choline, ^{13}C -glucose, ^{13}C -glutamine and ^{13}C -glutamate [Hövenner, 2008]. Other interesting molecules for *in vivo* application are tetrafluoropropyl propionate (TFPP) for imaging of atherosclerotic plaques [Bhattacharya et al., 2011] or barbiturates for drug monitoring [Roth et al., 2008, 2010b].

Since PHIP is based on a chemical reaction, large amounts of hyperpolarized molecules can be produced within a short time. Solid state DNP reaches the same signal enhancement (10^5) as the PHIP method [Ardenkjaer-Larsen et al., 2003], but is limited in the amount of hyperpolarized molecules since it does not allow for a continuous generation of hyperpolarization. Additionally, it has high technical demands. Using liquid state DNP, continuous flow generation of hyperpolarized molecules is possible with DNP [Krummenacker et al., 2012]. However, the enhancement factor of this method is limited by the gyromagnetic ratio of the hyperpolarized nucleus and the electrons (e. g. $\gamma(e^-)/\gamma(^{13}\text{C}) \approx 2600$).

Even though there are less biocompatible molecules available for PHIP at present, the possibility to produce a high amount of strongly hyperpolarized molecules motivates the effort to continue pushing the method for *in vivo* applications. This work makes a contribution to this task by showing the feasibility of two spin order transfer on a clinical MRI system.

Chapter 6

Bibliography

- A. Abragam. *The principles of nuclear magnetism*. Clarendon Press, 1983.
- A. Abragam and M. Goldman. Principles of Dynamic Nuclear-Polarization. *Reports on Progress in Physics*, 41(3):395–467, 1978.
- S. Aime, R. Gobetto, F. Reineri, and D. Canet. Hyperpolarization transfer from parahydrogen to deuterium via carbon-13. *Journal of Chemical Physics*, 119(17):8890–8896, 2003.
- M. J. Albers, R. Bok, A. P. Chen, C. H. Cunningham, M. L. Zierhut, V. Y. Zhang, S. J. Kohler, J. Tropp, R. E. Hurd, Y. F. Yen, S. J. Nelson, D. B. Vigneron, and J. Kurhanewicz. Hyperpolarized C-13 Lactate, Pyruvate, and Alanine: Noninvasive Biomarkers for Prostate Cancer Detection and Grading. *Cancer Research*, 68(20):8607–8615, 2008.
- J. H. Ardenkjaer-Larsen, B. Fridlund, A. Gram, G. Hansson, L. Hansson, M. H. Lerche, R. Servin, M. Thaning, and K. Golman. Increase in signal-to-noise ratio of $> 10,000$ times in liquid-state NMR. *Proceedings of the National Academy of Sciences of the United States of America*, 100(18):10158–10163, 2003.
- M. Bak, J. T. Rasmussen, and N. C. Nielsen. SIMPSON: A general simulation program for solid-state NMR spectroscopy. *Journal of Magnetic Resonance*, 147(2):296–330, 2000.
- S. Bär, T. Lange, D. Leibfritz, J. Hennig, Dv Elverfeldt, and J. B. Hövener. On the spin order transfer from parahydrogen to another nucleus. *Journal of Magnetic Resonance*, 225:25–35, 2012.
- R. Bellman. *Introduction to the Mathematical Theory of Control Processes: Nonlinear processes*. Academic Press, 1971.
- M.A. Bernstein, K.F. King, and X.J. Zhou. *Handbook of MRI Pulse Sequences: A Guide for Scientists, Engineers, Radiologists, Technologists*. Academic Press, 2004.

- P. Bhattacharya, K. Harris, A. P. Lin, M. Mansson, V. A. Norton, W. H. Perman, D. P. Weitekamp, and B. D. Ross. Ultra-fast three dimensional imaging of hyperpolarized C-13 in vivo. *Magnetic Resonance Materials in Physics Biology and Medicine*, 18(5): 245–256, 2005.
- P. Bhattacharya, E. Y. Chekmenev, W. H. Perman, K. C. Harris, A. P. Lin, V. A. Norton, C. T. Tan, B. D. Ross, and D. P. Weitekamp. Towards hyperpolarized C-13-succinate imaging of brain cancer. *Journal of Magnetic Resonance*, 186(1):150–155, 2007.
- P. Bhattacharya, E. Y. Chekmenev, W. F. Reynolds, S. Wagner, N. Zacharias, H. R. Chan, R. Bunger, and B. D. Ross. Parahydrogen-induced polarization (PHIP) hyperpolarized MR receptor imaging in vivo: a pilot study of (13)C imaging of atheroma in mice. *Nmr in Biomedicine*, 24(8):1023–1028, 2011.
- C. R. Bowers and D. P. Weitekamp. Transformation of Symmetrization Order to Nuclear-Spin Magnetization by Chemical-Reaction and Nuclear-Magnetic-Resonance. *Physical Review Letters*, 57(21):2645–2648, 1986.
- C. R. Bowers and D. P. Weitekamp. Para-Hydrogen and Synthesis Allow Dramatically Enhanced Nuclear Alignment. *Journal of the American Chemical Society*, 109(18):5541–5542, 1987.
- C. Bretschneider, A. Karabanov, N. C. Nielsen, and W. Kockenberger. Conversion of parahydrogen induced longitudinal two-spin order to evenly distributed single spin polarisation by optimal control pulse sequences. *Journal of Chemical Physics*, 136(9), 2012.
- L. Buljubasich, M. B. Franzoni, H. W. Spiess, and K. Münnemann. Level anti-crossings in ParaHydrogen Induced Polarization experiments with Cs-symmetric molecules. *Journal of Magnetic Resonance*, 219:33–40, 2012.
- D. Canet, S. Bouguet-Bonnet, C. Aroulanda, and F. Reineri. About long-lived nuclear spin states involved in para-hydrogenated molecules. *Journal of the American Chemical Society*, 129(5):1445–9, 2007.
- M. Carravetta and M. H. Levitt. Long-lived nuclear spin states in high-field solution NMR. *Journal of the American Chemical Society*, 126(20):6228–9, 2004.
- M. Carravetta and M. H. Levitt. Theory of long-lived nuclear spin states in solution nuclear magnetic resonance. I. Singlet states in low magnetic field. *Journal of Chemical Physics*, 122(21), 2005.
- M. Carravetta, O. G. Johannessen, and M. H. Levitt. Beyond the T-1 limit: Singlet nuclear spin states in low magnetic fields. *Physical Review Letters*, 92(15), 2004.

- A. P. Chen, M. J. Albers, C. H. Cunningham, S. J. Kohler, Y. F. Yen, R. E. Hurd, J. Tropp, R. Bok, J. M. Pauly, S. J. Nelson, J. Kurhanewicz, and D. B. Vigneron. Hyperpolarized c -13 spectroscopic imaging of the TRAMP mouse at 3T - Initial experience. *Magnetic Resonance in Medicine*, 58(6):1099–1106, 2007.
- M. M. Darpolor, Y. F. Yen, M. S. Chua, L. Xing, R. H. Clarke-Katzenberg, W. F. Shi, D. Mayer, S. Josan, R. E. Hurd, A. Pfefferbaum, L. Senadheera, S. So, L. V. Hofmann, G. M. Glazer, and D. M. Spielman. In vivo MRSI of hyperpolarized [1-C-13]pyruvate metabolism in rat hepatocellular carcinoma. *Nmr in Biomedicine*, 24(5):506–513, 2011.
- S. E. Day, M. I. Kettunen, F. A. Gallagher, D. E. Hu, M. Lerche, J. Wolber, K. Golman, J. H. Ardenkjaer-Larsen, and K. M. Brindle. Detecting tumor response to treatment using hyperpolarized C-13 magnetic resonance imaging and spectroscopy (vol 13, pg 1382, 2007). *Nature Medicine*, 13(12):1521–1521, 2007.
- J. F. Dechent, L. Buljubasich, L. M. Schreiber, H. W. Spiess, and K. Münnemann. Proton magnetic resonance imaging with para-hydrogen induced polarization. *Physical Chemistry Chemical Physics*, 14(7):2346–52, 2012.
- T. C. Eisenschmid, R. U. Kirss, P. P. Deutsch, S. I. Hommeltoft, R. Eisenberg, J. Bargon, R. G. Lawler, and A. L. Balch. Para Hydrogen Induced Polarization in Hydrogenation Reactions. *Journal of the American Chemical Society*, 109(26):8089–8091, 1987.
- T. C. Eisenschmid, J. McDonald, R. Eisenberg, and R. G. Lawler. Inept in a Chemical Way - Polarization Transfer from Para-Hydrogen to P-31 by Oxidative Addition and Dipolar Relaxation. *Journal of the American Chemical Society*, 111(18):7267–7269, 1989.
- R.R. Ernst, G. Bodenhausen, and A. Wokaun. *Principles of Nuclear Magnetic Resonance in One and Two Dimensions*. Clarendon Press, 1990.
- Y. Feng, R. M. Davis, and S. W. Warren. Accessing long-lived nuclear singlet states between chemically equivalent spins without breaking symmetry. *Nature Physics*, 2012.
- M. B. Franzoni, L. Buljubasich, H. W. Spiess, and K. Münnemann. Long-lived (1)h singlet spin States originating from para-hydrogen in cs-symmetric molecules stored for minutes in high magnetic fields. *Journal of the American Chemical Society*, 134(25):10393–6, 2012.
- F. A. Gallagher, M. I. Kettunen, S. E. Day, D. E. Hu, J. H. Ardenkjaer-Larsen, R. in't Zandt, P. R. Jensen, M. Karlsson, K. Golman, M. H. Lerche, and K. M. Brindle. Magnetic resonance imaging of pH in vivo using hyperpolarized (13)C-labelled bicarbonate. *Nature*, 453(7197):940–U73, 2008.

- F. A. Gallagher, M. I. Kettunen, D. E. Hu, P. R. Jensen, R. in't Zandt, M. Karlsson, A. Gisselsson, S. K. Nelson, T. H. Witney, S. E. Bohndiek, G. Hansson, T. Peitersen, M. H. Lerche, and K. M. Brindle. Production of hyperpolarized [1,4-C-13(2)]malate from [1,4-C-13(2)]fumarate is a marker of cell necrosis and treatment response in tumors. *Proceedings of the National Academy of Sciences of the United States of America*, 106(47):19801–19806, 2009.
- W. Gerlach and O. Stern. Der experimentelle Nachweis der Richtungsquantelung im Magnetfeld. *Zeitschrift für Physik*, 9(1):349–352, 1922.
- M. Goldman and H. Johannesson. Conversion of a proton pair para order into C-13 polarization by rf irradiation, for use in MRI. *Comptes Rendus Physique*, 6(4-5):575–581, 2005.
- M. Goldman, H. Johannesson, O. Axelsson, and M. Karlsson. Hyperpolarization of C-13 through order transfer from parahydrogen: A new contrast agent for MFI. *Magnetic Resonance Imaging*, 23(2):153–157, 2005.
- K. Golman, O. Axelsson, H. Johannesson, S. Mansson, C. Olofsson, and J. S. Petersson. Parahydrogen-induced polarization in imaging: Subsecond C-13 angiography. *Magnetic Resonance in Medicine*, 46(1):1–5, 2001.
- K. Golman, J. H. Ardenkjaer-Larsen, J. Svensson, O. Axelsson, G. Hansson, L. Hansson, H. Johannesson, I. Leunbach, S. Mansson, J. S. Petersson, G. Pettersson, R. Servin, and L. G. Wistrand. C-13-angiography. *Academic Radiology*, 9:S507–S510, 2002.
- K. Golman, R. in't Zandt, M. Lerche, R. Pehrson, and J. H. Ardenkjaer-Larsen. Metabolic imaging by hyperpolarized C-13 magnetic resonance imaging for in vivo tumor diagnosis. *Cancer Research*, 66(22):10855–10860, 2006.
- K. Golman, J. S. Petersson, P. Magnusson, E. Johansson, P. Akeson, C. M. Chai, G. Hansson, and S. Mansson. Cardiac metabolism measured noninvasively by hyperpolarized C-13 MRI. *Magnetic Resonance in Medicine*, 59(5):1005–1013, 2008.
- K. Gopalakrishnan and G. Bodenhausen. Lifetimes of the singlet-states under coherent off-resonance irradiation in NMR spectroscopy. *Journal of Magnetic Resonance*, 182(2):254–9, 2006.
- T. Gullion, D. B. Baker, and M. S. Conradi. New, Compensated Carr-Purcell Sequences. *Journal of Magnetic Resonance*, 89(3):479–484, 1990.
- E.M. Haacke, R.W. Brown, M.R. Thompson, and R. Venkatesan. *Magnetic Resonance Imaging: Physical Principles and Sequence Design*. Wiley, 1999.

- M. Haake, J. Natterer, and J. Bargon. Efficient NMR pulse sequences to transfer the parahydrogen-induced polarization to hetero nuclei. *Journal of the American Chemical Society*, 118(36):8688–8691, 1996.
- U. Haeberlen and J. S. Waugh. Coherent Averaging Effects in Magnetic Resonance. *Physical Review*, 175(2):453–467, 1968.
- E. L. Hahn. Spin Echoes. *Physical Review*, 80(4):580–594, 1950.
- J. B. Hövener. ^{13}C spin hyperpolarization by PASADENA: Instrumentation, preparation of magnetic tracers, and NMR spectroscopy and imaging in vivo. PhD thesis, 2008.
- J. B. Hövener, E. Y. Chekmenev, K. C. Harris, W. H. Perman, L. W. Robertson, B. D. Ross, and P. Bhattacharya. PASADENA hyperpolarization of C-13 biomolecules: equipment design and installation. *Magnetic Resonance Materials in Physics Biology and Medicine*, 22(2):111–121, 2009.
- H. Johannesson, O. Axelsson, and M. Karlsson. Transfer of para-hydrogen spin order into polarization by diabatic field cycling. *Comptes Rendus Physique*, 5(3):315–324, 2004.
- E. Johansson, S. Mansson, R. Wirestam, J. Svesson, S. Petersson, K. Golman, and F. Stahlberg. Cerebral perfusion assessment by bolus tracking using hyperpolarized C-13. *Magnetic Resonance in Medicine*, 51(3):464–472, 2004a.
- E. Johansson, L. E. Olsson, S. Mansson, J. S. Petersson, K. Golman, F. Stahlberg, and R. Wirestam. Perfusion assessment with bolus differentiation: A technique applicable to hyperpolarized tracers. *Magnetic Resonance in Medicine*, 52(5):1043–1051, 2004b.
- S. Kadlecik, K. Emami, M. Ishii, and R. Rizi. Optimal transfer of spin-order between a singlet nuclear pair and a heteronucleus. *Journal of Magnetic Resonance*, 205(1):9–13, 2010.
- D. W. J. Klomp, A. P. M. Kentgens, and A. Heerschap. Polarization transfer for sensitivity-enhanced MRS using a single radio frequency transmit channel. *Nmr in Biomedicine*, 21(5):444–452, 2008a.
- D. W. J. Klomp, J. P. Wijnen, T. W. J. Scheenen, and A. Heerschap. Efficient (1)H to (31)P Polarization Transfer on a Clinical 3T MR System. *Magnetic Resonance in Medicine*, 60(6):1298–1305, 2008b.
- S. E. Korchak, K. L. Ivanov, A. V. Yurkovskaya, and H. M. Vieth. Para-hydrogen induced polarization in multi-spin systems studied at variable magnetic field. *Physical Chemistry Chemical Physics*, 11(47):11146–11156, 2009.

- J. G. Krumpal, V. P. Denysenkov, M. Terekhov, L. M. Schreiber, and T. F. Prisner. DNP in MRI: An in-bore approach at 1.5 T. *Journal of Magnetic Resonance*, 215:94–99, 2012.
- C. Laustsen, G. Pileio, M. C. Tayler, L. J. Brown, R. C. Brown, M. H. Levitt, and J. H. Ardenkjaer-Larsen. Hyperpolarized singlet NMR on a small animal imaging system. *Magnetic Resonance in Medicine*, 2012.
- P. C. Lauterbur. Image Formation by Induced Local Interactions - Examples Employing Nuclear Magnetic-Resonance. *Nature*, 242(5394):190–191, 1973.
- M. H. Levitt. *Spin dynamics : basics of nuclear magnetic resonance*. John Wiley & Sons, Chichester, England ; Hoboken, NJ, 2nd edition, 2008.
- M. H. Levitt. Singlet Nuclear Magnetic Resonance. *Annual Review of Physical Chemistry*, Vol 63, 63:89–105, 2012.
- Z.P. Liang, P.C. Lauterbur, IEEE Engineering in Medicine, and Biology Society. *Principles of magnetic resonance imaging: a signal processing perspective*. SPIE Optical Engineering Press, 2000.
- P. Mansfield. Proton Spin Imaging by Nuclear Magnetic-Resonance. *Contemporary Physics*, 17(6):553–576, 1976.
- P. Mansfield and P.G. Morris. *NMR imaging in biomedicine*. Academic Press, 1982.
- G. A. Morris and R. Freeman. Enhancement of Nuclear Magnetic-Resonance Signals by Polarization Transfer. *Journal of the American Chemical Society*, 101(3):760–762, 1979.
- G. A. Morris, N. P. Jerome, and L. Y. Lian. Real-time chemical-shift scaling in high-resolution NMR spectroscopy. *Angew Chem Int Ed Engl*, 42(7):823–5, 2003.
- K. Münnemann and H. W. Spiess. Nuclear Magnetic Resonance the Art of Signal Enhancement. *Nature Physics*, 7(7):522–523, 2011.
- J. Natterer and J. Bargon. Parahydrogen induced polarization. *Progress in Nuclear Magnetic Resonance Spectroscopy*, 31:293–315, 1997.
- I. Park, P. E. Larson, M. L. Zierhut, S. Hu, R. Bok, T. Ozawa, J. Kurhanewicz, D. B. Vigneron, S. R. Vandenberg, C. D. James, and S. J. Nelson. Hyperpolarized ¹³C magnetic resonance metabolic imaging: application to brain tumors. *Neuro Oncol*, 12(2):133–44, 2010.

- I. Park, L. E. Jalbert, M. Ito, T. Ozawa, C. D. James, J. J. Phillips, D. B. Vigneron, R. O. Pieper, S. M. Ronen, and S. J. Nelson. Hyperpolarized C-13 Magnetic Resonance Spectroscopic Imaging Provides an Early Biomarker of Mgmt Activity and Response to Temozolomide Treatment. *Neuro-Oncology*, 13:72–72, 2011.
- G. Pileio and M. H. Levitt. Theory of long-lived nuclear spin states in solution nuclear magnetic resonance. II. Singlet spin locking. *Journal of Chemical Physics*, 130(21), 2009.
- G. Pileio, M. Carravetta, and M. H. Levitt. Storage of nuclear magnetization as long-lived singlet order in low magnetic field. *Proceedings of the National Academy of Sciences of the United States of America*, 107(40):17135–17139, 2010.
- G. Pileio, J. T. Hill-Cousins, S. Mitchell, I. Kuprov, L. J. Brown, R. C. Brown, and M. H. Levitt. Long-lived nuclear singlet order in near-equivalent (¹³C) spin pairs. *Journal of the American Chemical Society*, 134(42):17494–7, 2012.
- L.S. Pontryagin. *The mathematical theory of optimal processes*. John Wiley, 1962.
- M. Roth. *Sensitivity enhancement in NMR by using Parahydrogen Induced Polarization*. PhD thesis, 2009.
- M. Roth, J. Bargon, H. W. Spiess, and A. Koch. Parahydrogen induced polarization of barbituric acid derivatives: H-1 hyperpolarization studies. *Magnetic Resonance in Chemistry*, 46(8):713–717, 2008.
- M. Roth, P. Kindervater, H. P. Raich, J. Bargon, H. W. Spiess, and K. Münnemann. Continuous (¹H and (¹³C) Signal Enhancement in NMR Spectroscopy and MRI Using Parahydrogen and Hollow-Fiber Membranes. *Angewandte Chemie-International Edition*, 49(45):8358–8362, 2010a.
- M. Roth, A. Koch, P. Kindervater, J. Bargon, H. W. Spiess, and K. Münnemann. C-13 hyperpolarization of a barbituric acid derivative via parahydrogen induced polarization. *Journal of Magnetic Resonance*, 204(1):50–55, 2010b.
- R. Sarkar, P. R. Vasos, and G. Bodenhausen. Singlet-state exchange NMR spectroscopy for the study of very slow dynamic processes. *Journal of the American Chemical Society*, 129(2):328–34, 2007.
- M. A. Schröder, L. E. Cochlin, L. C. Heather, K. Clarke, G. K. Radda, D. J. Tyler, and R. G. Shulman. In vivo assessment of pyruvate dehydrogenase flux in the heart using hyperpolarized carbon-13 magnetic resonance. *Proceedings of the National Academy of Sciences of the United States of America*, 105(33):12051–12056, 2008.

- I. Solomon. Relaxation Processes in a System of 2 Spins. *Physical Review*, 99(2):559–565, 1955.
- J. Svensson, S. Mansson, E. Johansson, J. S. Petersson, and L. E. Olsson. Hyperpolarized C-13 MR angiography using TrueFISP. *Magnetic Resonance in Medicine*, 50(2):256–262, 2003.
- A. Tannus and M. Garwood. Adiabatic pulses. *Nmr in Biomedicine*, 10(8):423–434, 1997.
- Z. Tosner, T. Vosegaard, C. Kehlet, N. Khaneja, S. J. Glaser, and N. C. Nielsen. Optimal control in NMR spectroscopy: Numerical implementation in SIMPSON. *Journal of Magnetic Resonance*, 197(2):120–134, 2009.
- K. Ugurbil, M. Garwood, and A. R. Rath. Optimization of Modulation Functions to Improve Insensitivity of Adiabatic Pulses to Variations in B1 Magnitude. *Journal of Magnetic Resonance*, 80(3):448–469, 1988.
- O. Warburg. Origin of Cancer Cells. *Science*, 123(3191):309–314, 1956.
- W. S. Warren, E. Jenista, R. T. Branca, and X. Chen. Increasing hyperpolarized spin lifetimes through true singlet eigenstates. *Science*, 323(5922):1711–4, 2009.
- H. Watanabe, Y. Ishihara, K. Okamoto, K. Oshio, T. Kanamatsu, and Y. Tsukada. In vivo 3D localized C-13 spectroscopy using modified INEPT and DEPT. *Journal of Magnetic Resonance*, 134(2):214–222, 1998.
- Y. F. Yen, K. Nagasawa, and T. Nakada. Promising Application of Dynamic Nuclear Polarization for in Vivo C-13 MR Imaging. *Magnetic Resonance in Medical Sciences*, 10(4):211–217, 2011.

Chapter 7

Appendix

7.1 Abbreviations

AHT	Average Hamiltonian Theory
ALTADENA	Adiabatic Longitudinal Transport After Dissociation Engenders Net Alignment
CSA	Chemical Shift Anisotropy
CSS	Chemical Shift Scaling
CW	Continuous Wave
DD	Dipole-Dipole
DMAD	Dimethyl Acetylenedicarboxylate
DMM	Dimethyl Maleate
DNP	Dynamic Nuclear Polarization
EPI	Echo Planar Imaging
FID	Free Induction Decay
FOV	Field of View
FWHM	Full Width at Half Maximum
GRE	Gradient Echo
HEA	Hydroxyethyl Acrylate
HEP	Hydroxyethyl Propionate

INEPT	Insensitive Nuclei Enhanced by Polarization Transfer
MRI	Magnetic Resonance Imaging
MRS	Magnetic Resonance Spectroscopy
NMR	Nuclear Magnetic Resonance
OC	Optimal Control
PASADENA	Parahydrogen And Synthesis Allow Dramatically Enhanced Nuclear Alignment
pH ₂	Parahydrogen
PHIP	Parahydrogen Induced Polarization
PSF	Point Spread Function
RARE	Rapid Acquisition with Refocused Echoes
RF	Radiofrequency
SABRE	Signal Amplification By Reversible Exchange
SAR	Specific Absorption Rate
SE	Spin Echo
SI	Signal Intensity
SNR	Signal-to-Noise Ratio
SOT	Spin Order Transfer
TE	Echo Time
TFPP	Tetrafluoropropyl Propionate
TR	Repetition Time

7.2 Chemical Composition of Samples

Table 7.1: HEP experiments using hollow-fiber membrane modules (see section 3.2.1)

Chemical	Amount	CAS Number
2-hydroxyethylacrylate	600 mg	818-61-1
Rh(nor)(ppbs)BF ₄	2.5 mg	see below
D ₂ O	2000 mg	7789-20-0

Table 7.2: HEP experiments using the shaking method on a clinical MRI system (see sections 3.2.2 and 3.2.3)

Chemical	Amount	CAS Number
2-hydroxyethylacrylate	500 mg	818-61-1
Rh(nor)(ppbs)BF ₄	10 mg	see below
D ₂ O	2600 mg	7789-20-0

Table 7.3: Singlet spin state experiments using the shaking method on a clinical MRI system (see chapter 4)

Chemical	Amount	CAS Number
dimethyl acetylenedicarboxylate	500 mg	762-42-5
Rh(COD)(dppb)BF ₄	10 mg	79255-71-3
Acetone-d ₆	2600 mg	666-52-4

The water-soluble catalyst Rh(nor)(ppbs)BF₄ used to hydrogenate HEA to HEP was synthesized as described by Hövener et al. [2009] and additionally freeze-dried and stored as a solid under argon atmosphere.

7.3 Product Operator Formalism

In the following a more detailed explanation is given for the product operator formalism used in this thesis.

An arbitrary state of a spin-1/2 particle can be expressed by a linear combination of the Zeeman eigenstates (Eq. 2.2 on page 5):

$$|\Psi\rangle = c_\alpha |\alpha\rangle + c_\beta |\beta\rangle, \quad (7.1)$$

with the normalization $|c_\alpha|^2 + |c_\beta|^2 = 1$. This object is an element of the Hilbert space. In the vector notation, this state is written as a two dimensional complex vector:

$$|\Psi\rangle = \begin{pmatrix} c_\alpha \\ c_\beta \end{pmatrix}. \quad (7.2)$$

The definition of the spin density operator of a spin-1/2 ensemble was shown in equation 2.3 on page 6. The spin density operator can be expressed in a matrix using an orthonormal base $\{|i\rangle, i = 1, 2\}$:

$$\rho_{ij} = \langle i | \rho | j \rangle \quad (7.3)$$

Most frequent it is shown in the basis of the Zeeman eigenstates $\{|i\rangle, i = \alpha, \beta\}$ which was shown in equation 2.4 on page 6. This density matrix can be achieved using the vector multiplication of the column and row vector given in equation 7.2:

$$|\Psi\rangle\langle\Psi| = \begin{pmatrix} c_\alpha \\ c_\beta \end{pmatrix} \begin{pmatrix} c_\alpha^* & c_\beta^* \end{pmatrix}. \quad (7.4)$$

The density operator is an object in the Liouville space and can be expressed as a linear combination of an orthonormal basis set of operators $\{B_s\}$ in the Liouville space. An often used basis operator set is the so called Cartesian basis which consists of the unity operator and the spin angular momentum operators $\{B_s^1\} = \{\frac{1}{2}\mathbb{1}, I_x, I_y, I_z\}$, in which the matrix representation of the three angular momentum operators in the Zeeman eigenbasis are

$$I_x = \frac{1}{2} \begin{pmatrix} 0 & 1 \\ 1 & 0 \end{pmatrix}, \quad I_y = \frac{1}{2i} \begin{pmatrix} 0 & 1 \\ -1 & 0 \end{pmatrix}, \quad I_z = \frac{1}{2} \begin{pmatrix} 1 & 0 \\ 0 & -1 \end{pmatrix}. \quad (7.5)$$

If an N-spin-1/2 system is regarded, the space needs to be expanded which is shown representatively for a two spin system in the following. An arbitrary state of the two spin-1/2 system can be expressed with the Zeeman eigenbasis:

$$|\Psi\rangle = c_{\alpha\alpha} |\alpha\alpha\rangle + c_{\alpha\beta} |\alpha\beta\rangle + c_{\beta\alpha} |\beta\alpha\rangle + c_{\beta\beta} |\beta\beta\rangle, \quad (7.6)$$

which in the vector notation can be written as:

$$|\Psi\rangle = \begin{pmatrix} c_{\alpha\alpha} \\ c_{\alpha\beta} \\ c_{\beta\alpha} \\ c_{\beta\beta} \end{pmatrix}. \quad (7.7)$$

The matrix representation of the density operator of the two spin-1/2 ensemble can be calculated again by the vector multiplication like in equation 7.4. A basis set of operators $\{B_s\}$ for Liouville space of the N-spin-1/2 system can be defined by the products of the Cartesian basis operators:

$$B_s^N = 2^{(q-1)} \prod_{k=1}^N (B_s^1)_k, \quad (7.8)$$

where k is the index of the nucleus and q is the number of operators in the product which are not the unity operator. For the two-spin-1/2 system, the 16 product operators are

$$\begin{aligned} q = 0 & \quad \frac{1}{2}\mathbb{1}, \\ q = 1 & \quad I_{1x}, I_{1y}, I_{1z}, I_{2x}, I_{2y}, I_{2z}, \\ q = 2 & \quad 2I_{1x}I_{2x}, 2I_{1x}I_{2y}, 2I_{1x}I_{2z}, \\ & \quad 2I_{1y}I_{2x}, 2I_{1y}I_{2y}, 2I_{1y}I_{2z}, \\ & \quad 2I_{1z}I_{2x}, 2I_{1z}I_{2y}, 2I_{1z}I_{2z}, \end{aligned} \quad (7.9)$$

The matrix representation of these operators in the Zeeman eigenbasis can be achieved by calculating the direct product of the matrices of the individual operators, e. g.

$$\begin{aligned} I_{1x} &= 2I_x \otimes \frac{1}{2}\mathbb{1} = \frac{1}{2} \begin{pmatrix} 0 & 1 \\ 1 & 0 \end{pmatrix} \otimes \begin{pmatrix} 1 & 0 \\ 0 & 1 \end{pmatrix} \\ &= \frac{1}{2} \begin{pmatrix} 0 \begin{pmatrix} 1 & 0 \\ 0 & 1 \end{pmatrix} & 1 \begin{pmatrix} 1 & 0 \\ 0 & 1 \end{pmatrix} \\ 1 \begin{pmatrix} 1 & 0 \\ 0 & 1 \end{pmatrix} & 0 \begin{pmatrix} 1 & 0 \\ 0 & 1 \end{pmatrix} \end{pmatrix} \\ &= \frac{1}{2} \begin{pmatrix} 0 & 0 & 1 & 0 \\ 0 & 0 & 0 & 1 \\ 1 & 0 & 0 & 0 \\ 0 & 1 & 0 & 0 \end{pmatrix} \end{aligned} \quad (7.10)$$

$$\begin{aligned}
2I_{1z} \otimes I_{2z} &= 2 \frac{1}{2} \begin{pmatrix} 1 & 0 \\ 0 & -1 \end{pmatrix} \otimes \frac{1}{2} \begin{pmatrix} 1 & 0 \\ 0 & -1 \end{pmatrix} \\
&= \frac{1}{2} \begin{pmatrix} 1 \begin{pmatrix} 1 & 0 \\ 0 & -1 \end{pmatrix} & 0 \begin{pmatrix} 1 & 0 \\ 0 & -1 \end{pmatrix} \\ 0 \begin{pmatrix} 1 & 0 \\ 0 & -1 \end{pmatrix} & -1 \begin{pmatrix} 1 & 0 \\ 0 & -1 \end{pmatrix} \end{pmatrix} \\
&= \frac{1}{2} \begin{pmatrix} 1 & 0 & 0 & 0 \\ 0 & -1 & 0 & 0 \\ 0 & 0 & -1 & 0 \\ 0 & 0 & 0 & 1 \end{pmatrix}
\end{aligned} \tag{7.11}$$

7.4 Optimal Control Input File

The source file included contains the definitions necessary to perform the matrix multiplications used for the normalization of the results to the detection operator

```
source DG_mmatrix.tcl
```

Defining of the spin system including the chemical shift values and the J-coupling network:

```
spinsys {
  channels 1H 13C
  nuclei 1H 1H 1H 1H 1H 13C
  # 1H resonance between Ha/b/c and He/d
  shift 1 -0.6635p 0 0 0 0 0
  shift 2 -0.6635p 0 0 0 0 0
  shift 3 -0.6635p 0 0 0 0 0
  shift 4 0.6635p 0 0 0 0 0
  shift 5 0.6635p 0 0 0 0 0
  # 13C onresonant
  shift 6 0p 0 0 0 0 0
  # J-coupling network
  jcoupling 1 2 0 0 0 0 0 0
  jcoupling 1 3 0 0 0 0 0 0
  jcoupling 1 4 7.6 0 0 0 0 0
  jcoupling 1 5 7.6 0 0 0 0 0
  jcoupling 1 6 128.4 0 0 0 0 0
  jcoupling 2 3 0 0 0 0 0 0
  jcoupling 2 4 7.6 0 0 0 0 0
  jcoupling 2 5 7.6 0 0 0 0 0
  jcoupling 2 6 128.4 0 0 0 0 0
  jcoupling 3 4 7.6 0 0 0 0 0
  jcoupling 3 5 7.6 0 0 0 0 0
  jcoupling 3 6 128.4 0 0 0 0 0
  jcoupling 4 5 0 0 0 0 0 0
  jcoupling 4 6 4.65 0 0 0 0 0
  jcoupling 5 6 4.65 0 0 0 0 0
}
```

Setting some parameters:

```
par {
  # spectrometer settings
  proton_frequency 300e6
  sw 10000
  # set up liquid state
  spin_rate 0
  crystal_file alpha0beta0
  gamma_angles 1
  start_operator I1z*I4z
```

```

detect_operator I6z
variable sampling_dur 10
# Lamba is the weighting factor of the RF energy
variable lam 1.0e-6
# Duration to change RF channel
variable swdur 100
# Number of pulses
variable no_pulses 6
variable no_pulses_sim 3
# Just limit number of iterations in oc_optimize
oc_max_iter 20
# This MUST be used when working with optimal control!!!
conjugate_fid false
}

```

The following procedure generates a list of numbers equally distributed over a given range:

```

proc get_lims {SWH cp} {
  if { $cp <= 1 } {
    set Res 0
  } else {
    set step [expr double($SWH)/($cp-1)]
    set Res {}
    for {set i 0} {$i < $cp} {incr i} {
      set shft [expr double($SWH)/2.0-$i*$step]
      lappend Res $shft
    }
  }
  return $Res
}

```

Procedure to normalize the results with the norm of the target density operator:

```

proc norm {} {
  global par
  set detect [matrix get detect]
  # set par(scoring) 1
  set par(scoring) \
  [mtrace [mmult [mconjugate [mtranspose $detect]] $detect]]
}

```

Calculation of the total cost at which the contribution of every supporting point in the RF offset range has to be calculated:

```

proc target_function {} {
  global par rfsh1H_1 rfsh1H_2 rfsh1H_3 rfsh1H_4 \
  rfsh13C_1 rfsh13C_2 rfsh13C_3 rfsh13C_4 lims1H lims13C lifr1H
  set par(np) 1
  set eff 0.0
  foreach shft1H $lims1H {

```

```

    set shft1H_1 [expr -0.6635+$shft1H]
    set shft1H_2 [expr 0.6635+$shft1H]
    set f [fsimpson [list [list shift_1_iso $shft1H_1\p] \
    [list shift_2_iso $shft1H_1\p] \
    [list shift_3_iso $shft1H_1\p] \
    [list shift_4_iso $shft1H_2\p] \
    [list shift_5_iso $shft1H_2\p] \
    [list shift_6_iso 0\p] ] ]
    set dum [findx $f 1 -re]
    set eff [expr $eff+$dum]
    funload $f
}
set en1 [shape_energy $rfsh1H_1 $par(pulse_dur)]
set en2 [shape_energy $rfsh1H_2 $par(pulse_dur)]
set en3 [shape_energy $rfsh1H_3 $par(pulse_dur)]
set Res [expr $eff-$par(lamscal)*($en1 + $en2 + $en3)]
set Res_norm [expr $Res/$par(scalding)]
return [format "%.20f" $Res_norm]
}

```

Definition of the pulse sequence consisting of three OC pulses on the 1H channel and three OC pulses on the ^{13}C channel:

```

proc pulseq {} {
    global par rfsh1H_1 rfsh1H_2 rfsh1H_3 \
    rfsh13C_1 rfsh13C_2 rfsh13C_3
    reset
    pulse_shaped $par(pulse_dur) $rfsh1H_1 nothing
    delay $par(swdur)
    pulse_shaped $par(pulse_dur) nothing $rfsh13C_1
    delay $par(swdur)
    pulse_shaped $par(pulse_dur) $rfsh1H_2 nothing
    delay $par(swdur)
    pulse_shaped $par(pulse_dur) nothing $rfsh13C_2
    delay $par(swdur)
    pulse_shaped $par(pulse_dur) $rfsh1H_3 nothing
    delay $par(swdur)
    pulse_shaped $par(pulse_dur) nothing $rfsh13C_3
    if {$par(check)==0} {
        oc_acq_hermit
    } else {
        acq
    }
}
}

```

Calculation of gradients for the iterative optimization process:

```

proc gradient {} {
    global par rfsh1H_1 rfsh1H_2 rfsh1H_3 \

```

```

rfsh13C_1 rfsh13C_2 rfsh13C_3 lims1H lims13C lifr1H
set par(np) [expr $par(no_pulses_sim)*$par(NOC)]
# create empty fid for accumulating gradients
set f [fcreate -np $par(np) -sw $par(sw) ]
foreach shft1H $lims1H {
    set shft1H_1 [expr -0.6635+$shft1H]
    set shft1H_2 [expr 0.6635+$shft1H]
    set g [fsimpson [list [list shift_1_iso $shft1H_1\p] \
    [list shift_2_iso $shft1H_1\p] \
    [list shift_3_iso $shft1H_1\p] \
    [list shift_4_iso $shft1H_2\p] \
    [list shift_5_iso $shft1H_2\p] \
    [list shift_6_iso 0\p]] ]
    oc_grad_add_energy_penalty $g $rfsh1H_1 -$par(lam) \
    $rfsh1H_2 -$par(lam)    $rfsh1H_3 -$par(lam)
    fadd $f $g
    funload $g
}
return $f
}

```

Main procedure of the input file, which calculates the supporting points, starts the optimizations and saves the results:

```

proc main {} {
    global par rfsh1H_1 rfsh1H_2 rfsh1H_3 \
    rfsh13C_1 rfsh13C_2 rfsh13C_3 lims1H lims13C lifr1H
    set dir "$par(name)"
    file mkdir $dir
    # Parameter output file
    set outfile "$par(name)_parameters.dat"
    set fp [open $outfile w]
    puts $fp "\# IterationCycle Lambda Dur PW Real_Norm \
    En_1H_1 En_1H_2 En_1H_3 En_13C_1 En_13C_2 En_13C_3 \
    Res_Norm Scaling"
    set par(filename1H_1) "Pulse_1H_1.dat"
    set par(filename1H_2) "Pulse_1H_2.dat"
    set par(filename1H_3) "Pulse_1H_3.dat"
    set par(filename13C_1) "Pulse_13C_1.dat"
    set par(filename13C_2) "Pulse_13C_2.dat"
    set par(filename13C_3) "Pulse_13C_3.dat"
    # Calculate scaling
    set par(pulse_sequence) "norm"
    set f [fsimpson]
    set par(scaling) [lindex $par(scaling) 0]
    # Reset to pulseq
    set par(pulse_sequence) "pulseq"
}

```

```

# Duration of total pulse sequence and single pulses
set par(duration) 30500
set par(sampling_dur) 10
set par(pulse_dur) \
    [expr ($par(duration)-($par(no_pulses)-1)*\
    $par(swdur))/ $par(no_pulses)]
# Number of sample points per pulse
set par(NOC) [expr $par(pulse_dur)/ $par(sampling_dur)]
# Supporting points in Offset Range
set par(supp01H) 17
set lims1H [get_lims 1 $par(supp01H)]
set par(lamscal) [expr $par(lam)*$par(supp01H)]
# Number of Iteration per Cycles
set par(NoIterCycles) 50

# Run optimization cycles. After every cycle the pulses are saved
for {set par(i) 1} {$par(i) <= $par(NoIterCycles)} {incr par(i)} {
    set par(check) 0
    # Load 1H pulses of last cycle and 13C pulses
    set rfsh1H_1 [load_shape \
    "$dir/CP_17_Cycle_[expr $par(i)-1]_-$par(filename1H_1)"]
    set rfsh1H_2 [load_shape \
    "$dir/CP_17_Cycle_[expr $par(i)-1]_-$par(filename1H_2)"]
    set rfsh1H_3 [load_shape \
    "$dir/CP_17_Cycle_[expr $par(i)-1]_-$par(filename1H_3)"]
    set rfsh13C_1 [load_shape \
    "$dir/CP_17_Cycle_0_-$par(filename13C_1)"]
    set rfsh13C_2 [load_shape \
    "$dir/CP_17_Cycle_0_-$par(filename13C_2)"]
    set rfsh13C_3 [load_shape \
    "$dir/CP_17_Cycle_0_-$par(filename13C_3)"]
    set tfopt [oc_optimize $rfsh1H_1 -min 0 -max 3600 \
    $rfsh1H_2 -min 0 -max 3600 \
    $rfsh1H_3 -min 0 -max 3600]
    # Save pulses
    save_shape $rfsh1H_1 \
    "$dir/CP_17_Cycle_-$par(i)_-$par(filename1H_1)"
    save_shape $rfsh1H_2 \
    "$dir/CP_17_Cycle_-$par(i)_-$par(filename1H_2)"
    save_shape $rfsh1H_3 \
    "$dir/CP_17_Cycle_-$par(i)_-$par(filename1H_3)"
    # final checking of sequence
    set par(check) 1
    set f [fsimpson]
    set re_norm [expr [findex $f 1 -re]/ $par(scaling)]
    set en1 [shape_energy $rfsh1H_1 $par(pulse_dur)]

```

```

set en2 [shape_energy $rfsh1H_2 $par(pulse_dur)]
set en3 [shape_energy $rfsh1H_3 $par(pulse_dur)]
set en4 [shape_energy $rfsh13C_1 $par(pulse_dur)]
set en5 [shape_energy $rfsh13C_2 $par(pulse_dur)]
set en6 [shape_energy $rfsh13C_3 $par(pulse_dur)]
set Res_norm [expr $re_norm - $par(lam)*($en1 + $en2 + \
    $en3 + $en4 + $en5 + $en6)/$par(scaling)]
puts $fp "$par(i) $par(lam) $par(duration) \
    $par(sampling_dur) $re_norm $en1 $en2 $en3 $en4 \
    $en5 $en6 $Res_norm $par(scaling)"
    free_all_shapes
flush $fp
}
close $fp
}

```

7.5 Acknowledgments

An dieser Stelle möchte ich mich bei allen herzlich bedanken, die zum Gelingen dieser Arbeit beigetragen haben!

7.6 Declaration

I hereby declare that I wrote the dissertation submitted without any unauthorized external assistance and used only sources acknowledged in the work. All textual passages with are appropriated verbatim or paraphrased from published and unpublished texts as well as all information obtained from oral sourced are duly indicated and listed in accordance with bibliographical rules. In carrying out this research, I complied with the rules of standard scientific practice as formulated in the statutes of Johannes Gutenberg-University Mainz to insure standard scientific practice.

Mainz, Germany

Dirk Markus Graafen

7.7 Curriculum Vitae

Personal Data

Dirk Graafen

*31.03.1982 in Mainz, Germany

Married, two children

Studies

Medicine

08/2008 First Episode of the Medical Exam (Grade: 2.0)

Since 10/2005 Study of Medicine at the Johannes Gutenberg-University in Mainz

Physics

10/2008 to 02/2013 PhD candidate at the Section of Medical Physics of the
Medical Center of the Johannes Gutenberg-University Mainz

Since 01/2008 Diploma in Physics (Grade: "sehr gut")

01/2007 to 01/2008 Diploma thesis at the Section of Medical Physics of the
Medical Center of the Johannes Gutenberg-University in Mainz

10/2002 to 01/2008 Study of Physics at the Johannes Gutenberg-University in Mainz

Education

09/1992 to 06/2001 Secondary School: Graf-Stauffenberg-Schule in Flörsheim
Qualification: Abitur (Grade:1.0)

Publications

D. Graafen, K. Münnemann, S. Weber, K.-F. Kreitner, L. M. Schreiber. Quantitative contrast-enhanced myocardial perfusion magnetic resonance imaging: Simulation of bolus dispersion in constricted vessels. *Medical Physics*, 36(7):3099-3106, 2009.

D. Graafen, J. Hamer, S. Weber, L. M. Schreiber. Quantitative myocardial perfusion magnetic resonance imaging: The impact of pulsatile flow on contrast agent bolus dispersion. *Physics in Medicine and Biology*, 56/16(:5167-5185, 2011.

R. Schmidt, D. Graafen, S. Weber, L. M. Schreiber. Computational fluid dynamics simulations of contrast agent bolus dispersion in a coronary bifurcation: Impact on MRI-based quantification of myocardial perfusion. *Computational an Mathematical Methods in Medicine*, 2013. accepted